NBS-GCR-87-532

Thermophoretic Sampling and Soot Aerosol Dynamics of an Ethene Diffusion Flames

Constantine M. Megaridis

December 1987

Sponsored by
U.S. DEPARTMENT OF COMMERCE
National Bureau of Standards
Center for Fire Research
Gaithersburg, MD 20899

NBS-GCR-87-532

THERMOPHORETIC SAMPLING AND SOOT AEROSOL DYNAMICS OF AN ETHENE DIFFUSION FLAMES

Constantine M. Megaridis

Brown University
Providence, RI

December 1987

Sponsored by
U.S. DEPARTMENT OF COMMERCE
National Bureau of Standards
Center for Fire Research
Gaithersburg, MD 20899

Thermophoretic Sampling and Soot Aerosol Dynamics of an Ethene Diffusion Flame

by

Constantine M. Megaridis

B. S. Mechanical Engineering,

National Technical University of Athens, Greece

June, 1982

M. S. Applied Mathematics,

Brown University, Providence, RI

May, 1986

Thesis

Submitted in partial fulfillment of the requirements for the

Degree of Doctor of Philosophy in the

Division of Engineering at Brown University

May, 1987

Acknowledgment

I would like to express my gratitude to my research advisor Professor Richard A. Dobbins for his guidance and supervision during the course of my work. The instructions of M. Sosnowski in the first steps of the operation of the electron microscope are acknowledged with deep appreciation. R. Follansbee made major contributions to the design of the probe control system and was responsible for its construction. Prof. H. Kolsky generously provided high-speed photographic equipment and guidance in its use. Prof. J. Gurland provided the data acquisition system and familiarized me with its operation. Special thanks are due to Ms. Jacque Groves who typed the bulk of the dissertation. The invaluable moral support of my parents throughout my graduate studies is gratefully appreciated. At last, but not least, I would like to thank all my colleagues and friends who kept me motivated throughout my studies at Brown. This research was sponsored by the Center for Fire Research of the National Bureau of Standards under Grants NB83-NADA4025 and 60NANB6D0643.

TABLE OF CONTENTS

CHAPTER 1. INTRODUCTION 1

1.1 Thesis objective 4

CHAPTER 2. SOOT FORMATION IN A LAMINAR AXISYMMETRIC ETHENE/AIR DIFFUSION FLAME. PREVIOUS STUDIES. 7

2.1 The ethene laminar diffusion flame. Optical studies 8

CHAPTER 3. EXPERIMENTAL 18

3.1 Thermophoretic probes 18

3.2 Boundary layer studies of the flow field around the probe. 23

3.3 Thermophoretic studies on soot particle transport 27

3.4 Probe control system and burner 29

3.5 Experimental results and discussion 33

3.6 A hypothetical description of the physical aspects of soot formation and transport in the laminar axisymmetric ethene diffusion flame. 55

CHAPTER 4. THEORETICAL 61

4.1 A bimodal integral solution of the aerosol dynamic equation. 61

4.1.1 Description of the model 62

4.1.2 Surface growth term 77

4.1.3 Transition from the bimodal to the monomodal integral solution. 87

4.2 A monomodal integral solution of the aerosol dynamic equation 96

4.3 Other models for simulating aerosol dynamics 102

TABLE OF CONTENTS (Continued)

4.4 Comparisons of the models 109

4.5 Bimodal solution predictions for the soot aerosol in the coannular ethene/air diffusion flame 115

CHAPTER 5. CONCLUSIONS AND RECOMMENDATIONS. 128

APPENDIX A. Numerical evaluation of the collision integrals 132

REFERENCES 138

FIGURES 151

LIST OF TABLES

Table 2.1 Experimental light scattering ratio measurements.

Table 2.2 Experimental light scattering coefficient and depolarization ratio measurements.

Table 3.1 Selected data for the ethene diffusion flame.

Table 3.2 Radial dependence of soot morphological data for the ethene diffusion flame.

Table 4.1 Nomenclature used in bimodal solution.

Table 4.2 Nomenclature used in monomodal solution.

Table 4.3 Nomenclature used in MAEROS solution.

Table 4.4 Residence time data for particles ultimately transported on the annular region.

Table 4.5 Selected optical data for particles in the annular region of the ethene diffusion flame.

Table A.1 Comparison of collision integrals with interpolation formulae.

LIST OF FIGURES

Figure 2.1 Typical structure of a nonsmoking coannular laminar diffusion flame.

Figure 2.2 (a) Soot volume fraction, (b) particle diameter, and (c) number concentration as a function of z and r for the ethene diffusion flame. Reproduced from ref. 85.

Figure 2.3 Velocity profiles in the ethene diffusion flame; (a) axial velocity component, (b) radial velocity component. Reproduced from ref. 86.

Figure 2.4 Temperature profiles in the ethene diffusion flame at various axial locations z (uncorrected thermocouple measurements). Reproduced from ref. 82.

Figure 2.5 Flame front structure of a coannular laminar diffusion flame. The coordinate system is also displayed.

Figure 2.6 (A) Particle paths, and (B) residense times, calculated from the velocity measurements for the ethene diffusion flame. Reproduced from refs. 86 and 81 respectively.

Figure 2.7 (a) Soot volume fraction, (b) particle diameter, and (c) number concentration along the line exhibiting the maximum volume fraction value. Only the curves labeled 3.85 cc/s are related to the ethene diffusion flame under investigation. Reproduced from ref. 86.

Figure 3.1 Sketch of thermophoretic probe devices; (a) circular grid, (b) bulk specimen carrier, (c)-(f) modified probes.

Figure 3.2 Sketch of thermophoretic probe sampling of a coannular diffusion flame. The flame coordinate system and the radial position r_c of maximum soot volume fraction are also shown.

Figure 3.3 (A) Numerically calculated temperature contours, and (B) velocity contours of the flow field around the probe. The thermal boundary layer δ_t, and the trajectory of a soot particle ultimately captured halfway along the probe are also shown. (C) Schematic of a particle P traversing the distance between two neighboring isotherms.

Figure 3.4 Schematic diagram of the probe control system and related equipment.

Figure 3.5 Typical oscilloscope record of the probe trajectory. Transit time $\tau_t \approx 16$ ms, exposure (residence) time $\tau_e \approx 36$ ms.

Figure 3.6 Cross sectional drawing of the coannular burner.

Figure 3.7 TEM micrograph of soot particles deposited on a carbon substrate supported by a copper grid positioned at z=30 mm. The grid bar is shown as the dark boundary. Grid exposure time $\tau_e \approx 30$ ms.

Figure 3.8 TEM micrographs of soot particles collected from the annular region of the ethene diffusion flame at various heights z, using carbon coated grids. For all cases $\tau_e \approx 30$ ms except (A) where $\tau_e \approx 120$ ms. (A) z=10 mm, (B) z=20 mm, (C) z=30 mm, (D) z=40 mm, (E) z=50 mm, (F) z=80 mm.

Figure 3.9 Mechanisms of soot particle growth.

Figure 3.10 TEM micrographs of soot particles collected from the annular region of the ethene diffusion flame at a height z=20 mm, using carbon coated grids. (A) τ_e=30 ms, (B) τ_e=50 ms, (C) τ_e=70 ms, (D) τ_e=90 ms.

Figure 3.11 High magnification TEM micrographs of the particles described in Figure 3.10.

Figure 3.12 TEM micrographs of soot particles collected from the methane coannular diffusion flame using the type II probe. (A) z=25 mm, r=4.03 mm=r_c, τ_e=64 ms, (B) z=25 mm, r=4.77 mm>r_c, τ_e=64 ms, (C) z=15 mm, r=4.43 mm=r_c, τ_e=72 ms, (D) z=15 mm, r=5.44 mm>r_c, τ_e=72 ms.

Figure 3.13 Primary particle size as function of height, near r=r_c, for the ethene diffusion flame. Each size measurement is an average over about 100 primary particles.

Figure 3.14 TEM micrographs of soot particles collected on a type I probe from an axial location z=30 mm of the ethene diffusion flame, and at three different radial positions (A) r=1.28 mm, (B) r=2.54 mm$\sim$$r_c$, (C) r=2.89 mm. Probe exposure time τ_e=36 ms.

Figure 3.15 TEM micrographs of soot particles collected on a type III probe positioned at z=10 mm in the ethene diffusion flame.Probe exposure time τ_e=48 ms. (A) r=1.54 mm, (B) r=3.96 mm$\sim$$r_c$,(C) r=4.59 mm.

Figure 3.16 TEM micrographs of soot particles collected from the fuel side of $r_c(r<r_c)$, at z=30 mm of the ethene diffusion flame. Type IV probe exposure time τ_e=30 ms. (A) r=0.64 mm, (B) r=1.30 mm.

Figure 3.17 TEM micrographs of soot particles collected from the outside region of $r_c(r>r_c)$, at z=30 mm of the ethene diffusion flame. Type IV probe exposure time τ_e=36 ms. (A) r=2.59 mm$\sim r_c$, (B) r=3.13 mm, (C) r=3.35 mm.

Figure 3.18 TEM micrographs of soot particles collected on a type IV probe positioned at z=15 mm in the ethene diffusion flame. Probe exposure time τ_e=36 ms. (A) r=0.64 mm, (B) r=2.60 mm, (C) r=3.44 mm.

Figure 3.19 TEM micrographs of soot particles collected on a type I probe, positioned at z=15 mm in the ethene diffusion flame. Probe exposure time τ_e=36 ms. (A) r=3.05 mm$\sim r_c$, (B) r=3.73 mm, (C) r=3.05 mm$\sim r_c$, (D) digitized picture of the particles shown in C.

Figure 3.20 Comparison of the actual with the equivalent log-normal distributions at the two radial positions analyzed at z=15 mm. (A) r=3.05 mm, (B) r=3.73 mm.

Figure 3.21 Comparison of the distributions obtained from the numerical experiment described in the text. (A) 90 randomly distributed diameters, (B) 500 randomly distributed diameters.

Figure 3.22 Structure of the lower and intermediate regions of the coannular ethene diffusion flame. Particle paths (trajectories) and the loci of T_{max} and ϕ_{max} are also shown. N,ϕ and T profiles corresponding to a height z=10 mm are displayed. Information obtained from refs. 85 and 86.

Figure 4.1 Schematic of a bimodal PVDF. The various processes involved in the formulation of the bimodal integral solution are shown.

Figure 4.2 (A) Gaussian source pulse used in the example of free molecular coagulation discussed in the text. (B) Particle volume fraction versus time for the same example.

Figure 4.3 (A) Number concentration, and (B) second moment time variation obtained by the three methods examined, for the case of free molecular coagulation with a Gaussian source term.

Figure 4.4 Comparison of f_N profiles obtained by the three methods, for the case of free molecular coagulation with a Gaussian source term.

Figure 4.5 Mass concentration histograms obtained by the MAEROS solution for the case of free molecular coagulation with a Gaussian source term. (A) t=0.02 sec, (B) t=0.04 sec, (C) t=0.16 sec.

Figure 4.6 Particle volume distribution obtained by the two integral solutions, at an instant where the source term achieves a maximum (t_m=0.03 sec). The geometric mean volume of the source particles is also shown.

Figure 4.7 Time evolution of the PVPF of the growth mode for the case of free molecular coagulation with a Gaussian source term.

Figure 4.8 (A) Number concentration, and (B) particle volume fraction time variation of the two modes, as calculated by the bimodal integral solution for the case of free molecular coagulation with a Gaussian source term.

Figure 4.9 Time variation of the geometric standard deviation of the growth mode for the case of free molecular coagulation with a Gaussian source term. The asymptotic value corresponding to the self-preserving form is also shown.

Figure 4.10 Particle volume fraction profile used by the bimodal solution to duplicate the optically determined values. These values correspond to particles transported on the annular region and were determined using Mie scattering theory.

Figure 4.11 (A) Particle diameter and (B) number concentration versus residence time, as calculated by the bimodal solution in the numerical simulation of the soot aerosol. The values determined by the optical and thermophoretic techniques are also shown.

Figure 4.12 (A) Time variation of f_N and (B) Gaussian source pulse used in the numerical simulation of the soot aerosol.

Figure 4.13 Time variation of volumetric Rayleigh scattering cross section Q_{vv} as calculated by the bimodal solution in the numerical simulation of the soot aerosol.

Figure 4.14 Time variation of (A) soot surface area and (B) specific growth rate used in the numerical simulation of the soot aerosol.

Figure 4.15 Time variation of (A) particle number concentration, and (B) particle diameter with and without the surface growth reaction term.

Abstract

A detailed investigation of the sooting structure of an overventilated laminar axisymmetric ethene/air diffusion flame under atmospheric pressure is presented. A thermophoretic sampling technique using a variety of probes is employed to obtain data on the morphological character of soot particles collected from various locations of the flame. The morphological features of the particles examined by Transmission Electron Microscopy provide not only qualitative information on particle agglomeration, surface growth, and oxidation but also quantitative data on primary particle size as a function of flame coordinates. An increasing primary particle size with height above the burner mouth proved the dominance of surface growth reactions on the morphology of particles transported in the lower and intermediate portions of the flame. The surface growth reaction rate throughout these regions was calculated from a series of observations without any assumption on the form of the particle size distribution. The primary particle size was found to decrease as the particles move to the upper regions of the flame probably because of oxidation. A theoretical model examining the aerosol dynamics when particle formation, coagulation, and surface growth are present is also discussed. The model uses a time varying bimodal representation of the aerosol size distribution function with a prescribed logarithmic-normal form. The model can be used to study the physical/chemical processes acting upon the particulate phase in various aerosol systems in which particle generation mechanisms are present. The thermophoretic method, combined with existing data obtained by others through laser-light scattering and extinction measurements on the same flame, is used to describe the physical aspects of soot formation and transport. The combined observations of the two methods led to the conclusion that the soot particles are formed locally low in the flame in regions of high temperature near the reaction zone. The two experimental methods together with the theoretical model form a powerful unit used to gain a better understanding of the soot formation processes related to a diffusion flame environment.

CHAPTER 1

INTRODUCTION

Soot emission from various combustion appliances is a phenomenon observed very frequently. The light of a candle flame has its origin to the presence of incandescent soot particles. The efficiency of an internal combustion engine, particularly of a diesel motor, depends on the suppression of the soot formation processes. It is therefore desirable to control the soot formation mechanisms in order to avoid poor combustion and a loss of efficiency in practical combustion systems. However the presence of soot is desirable in some technical processes for a more efficient heat transfer, since the ability of the soot particles to radiate promotes the heat transport. In these systems subsequent oxidation of the particles is necessary in order to avoid pollution. The production of carbon black from the pyrolysis of hydrocarbons is another process where a maximum yield of soot is desirable.

The above discussion explains the intense research activity related to the soot formation processes during the last twenty years, mainly focused on the study of laboratory scale systems. These studies produce valuable information on the soot formation mechanisms in simple combustion systems and can be used to study the more complicated phenomena related to large scale fires.

The conditions under which soot is formed vary, and depend on numerous factors. Generally the generation of soot in combustion systems occurs in a temperature range between 1500 and 2500 K. The conversion of carbon available in the fuel consumed to soot, varies for different systems. For a laminar axisymmetric ethene/air diffusion flame under

atmospheric pressure the conversion[86] is 10-15%. However at elevated pressures the soot yield can be appreciably higher (~50% for the laminar diffusion flames studied by Flower and Bowman[26,27]). The soot particles look black and consist mainly of carbon and up to 10% per mole hydrogen. Newly formed particles in flames have a larger hydrogen content and display a considerably higher reactivity when compared to the old particles[45]. The macroscopic density of old soot has been found[19,64,67] to be in the interval 1.8 - 2 gr/cm^3. The density of incipient soot may be substantially lower because of the high hydrogen content.

The soot particles inside a combustion environment form an aerosol which can be characterized by the following quantities: the volume concentration of the particulate phase ϕ, called particle volume fraction (cm^3/cm^3), the particle number concentration N (cm^{-3}), and the particle size D (nm). Various studies concentrate on the determination of those parameters which uniquely define the dispersed phase.

In the various combustion systems the time available for the development of the soot formation processes is of the order of a few milliseconds. During this period a certain sequence of events takes place in a specific order. The first stage, called particle inception or particle formation, incorporates the generation of soot "nuclei" from the fuel molecules via oxidation and pyrolysis products (molecules, radicals, ions). Chemical kinetically controlled reactions initially create the precursor species needed to form the first soot particles, called incipient particles. Various theories about the nature of the soot precursors in flames have been developed so far. The most likely precursors are considered to be the unsaturated hydrocarbons,

like acetylene and its higher analogs ($C_{2n}H_2$), as well as polycyclic aromatic hydrocarbons. Other theories suggest that flame generated ions or radicals are also major species involved in the soot formation processes. The precursor species are then combined through a mechanism that is not well understood to form the incipient soot particles. These particles are small[45] (1~3 nm), and are created in large numbers thus forming the soot aerosol hosted by the combustion gases. Even though the first soot particles are created locally in high number concentrations they are associated with a very low soot loading because of their small size.

The second stage involves the growth of the existing particles (increasing D) through two different mechanisms. Particle coagulation (when particles collide and coalesce) which is representative of the early stage of soot formation, or particle agglomeration (when chain-like particles are formed) representative of the stages thereafter. Both coagulation and agglomeration result in a decrease of the number concentration N while the volume fraction ϕ remains constant. The other mechanism, called surface growth, involves the gas phase mass deposition on the surface of the existing particles through heterogeneous reactions. Surface growth results in an increase of ϕ while N remains unchanged. The mechanisms of growth are mainly responsible for the bulk of soot generated during combustion. Agglomeration and surface growth may coexist and their relative contribution to the formation of the macroscopic fluffy soot flocs visible in the atmosphere varies accordingly to the conditions present in the combustion environment.

The stages of soot formation and growth finally terminate when the oxidation mechanisms dominate. The third stage thus involves the burning of

the particles in the presence of oxidizing species to form gaseous products such as CO, CO_2 etc. The intensity of the oxidative attack determines the eventual emission of soot particles from the combustion device. This emission highly depends on the temperature[34] and velocity fields inside the system as well as the presence of additives[45,55] which can alter its behavior drastically. Most soot studies so far have concentrated on simple combustion systems and in particular laboratory scale flames. In the premixed flames both fuel and oxidant are mixed prior to the combustion process. Diffusion flames are those in which the mixing of fuel and oxidant occurs in the combustion region through molecular or turbulent diffusion processes. The premixed flames have been thoroughly[3,4,6,7,38-43,47,48,76,98] investigated, and the soot formation and depletion mechanisms are better understood at this instant. The mechanisms of soot formation and growth may be quite different from system to system, and most of the details of these mechanisms are still not well established. This is clearly demonstrated by a series of recent review articles[10,45,53,55,82,96] summarizing the results of numerous studies on soot formation. The intense interest of the scientific community for a better understanding of the soot formation processes is illustrated by the long list of 388 references in one[45] of the above mentioned reviews.

1.1 Thesis objective

The first attempts to understand the structure of diffusion flames were made by Burke and Schumann[9] who developed a theory to predict the ideal flame front, based on a model of equal interdiffusion of both fuel and oxidizer. Their simple theory predicted the heights of a variety of axisymmetric flames very successfully, using the appropriate values of

diffusion coefficients. However the visible flame height is not always the same, depending on the overall production of soot as well as its depletion by oxidation. Most experimental work since then has concentrated on the investigation of soot formation, growth and depletion mechanisms in both premixed and diffusion flames. Although numerous studies have been completed so far, many details related to soot production and oxidation in flames are not yet well established.

The present study attempts a detailed investigation of the sooting structure of an overventilated laminar axisymmetric ethene/air diffusion flame under atmospheric pressure conditions. A wealth of existing data provides us with valuable information on the temperature and velocity fields of an identical flame[85] analyzed at the Centers of Fire Research and Chemical Engineering of the National Bureau of Standards (NBS). A series of optical tests[82-86] performed there, produced information on the structure of the soot field throughout the coannular ethene diffusion flame. However these tests proved inadequate to provide information on the size distribution of the soot particles, and to assess the relative contributions of various mechanisms (particle inception, agglomeration, surface growth, oxidation) affecting the soot particle morphology.

A thermophoretic sampling technique presented in this work provides data on the morphological character of soot particles corresponding to various locations of the flame. Additional information on the contribution of surface growth is also obtained through the analysis of soot samples collected thermophoretically from the flame environment. A theoretical model of soot aerosol dynamics is also developed and used to interpret the experimental data.

The two experimental methods together with the theoretical model form a powerful unit, used to gain a better understanding of the soot formation processes related to a diffusion flame environment.

The current work begins with a general discussion on soot particle diagnostic methods and a brief review of the data obtained at NBS through the laser light scattering and extinction measurements. A series of boundary layer studies on soot particle transport related to the thermophoretic method is presented in the next section, followed by a detailed description of the experimental apparatus. The experimental results are then presented with an extensive evaluation of the data and a critical discussion. The theoretical model is developed in the following section and is subsequently used to evaluate the data obtained experimentally. The last section presents the conclusions of the study and recommendations for future work. The treatise is concluded with the appendices and other related material.

CHAPTER 2

SOOT FORMATION IN A LAMINAR AXISYMMETRIC ETHENE/AIR DIFFUSION FLAME. PREVIOUS STUDIES

The interest in the formation, evolution and partial or complete oxidation of soot in flames resulted in the development of a wide variety of sampling methods. The two most widely used are the "in situ" methods examining the particles in location, and the direct sampling methods which remove the particles from their environment. The scattering of a light beam has been used initially to analyze the soot field in a flame environment[54,71]. The more accurate laser light scattering and transmission tests were subsequently employed[5,14-17,44,49,51,52] for an "in situ" analysis of the soot field in flames. These methods have considerable appeal because they are nonintrusive and allow observation of the soot field without intervening in the chemical and physical processes which are present. However a weak point of these methods is their inability to distinguish between single and agglomerated particles that cause the scattering of the light. Direct sampling of the particles, an intrusive technique, has appeared in several forms so far but it has received more limited attention because of questions related to the validity of the morphological observations. Some of the direct sampling methods are based on the fact that soot deposition rates on cold targets immersed in flames are dominated by particle thermophoresis, i.e. particle drift down the temperature gradient. According to this principle, soot particles have often been collected on cold surfaces[49,74,76,80,88,95] for subsequent analysis by electron microscopy. Another method consists of using a sampling orifice[12,71,78] to collect the particles from the interior of the flame and subsequently analyze them through electron microscopy techniques. This method however involves a few steps

which aim at the separation of the sampled particles from the combustion gases withdrawn from the flame. These steps may affect the particle morphology thus causing a degree of uncertainty of the results obtained using this method. The molecular beam-sampling method has also been used extensively[3,48,98], but its use is limited only to the investigation of low pressure flat flames. None of the above sampling methods has clearly an edge over the others. A possible combination of these techniques has a greater potential to produce more information related to the soot formation processes in a flame environment.

2.1 The ethene laminar diffusion flame. Optical studies

The combustion system studied in the current work is a coannular laminar ethene/air diffusion flame under atmospheric pressure conditions. The burner consists of two concentric brass tubes of 11.1 mm and 101.6 mm i.d. The fuel flows through the inner tube while the ventilating air flow passes through the annulus between the two tubes. A detailed description of the burner is given in Section 3.4.

The flow rates adopted throughout this work for the ethene and the air are 3.85 and 713.3 cm^3/s respectively. These flow rates result in a laminar flame of definite shape and height (88 mm) shown in Figure 2.1. It is clear that the flame has an axisymmetric structure characterized by a cylindrical coordinate system (r,z). The lowest part of the flame is surrounded by a blue zone which extends up to a height of 3-5 mm. The rest of the flame appears as an envelope characterized by the familiar soot luminosity and a strong absorptivity. The luminous flame envelope closes at

the top which is a general characteristic of flames that release no soot to the environment (non smoking flames).

The structure of the soot field of the coannular ethene diffusion flame has been previously investigated using laser light-scattering and extinction measurements[83-86]. The apparatus used is described in ref. 86. A 4W argon ion laser operating at the 514.5 nm laser line was used as the light source for the scattering and extinction measurements. The laser was operated at the 488.0 nm line for the fluorescence experiments. The beam diameter was approximately 0.2 mm with a radial control of 0.127 mm. In all the experiments the incident beam was vertically polarized. We should mention at these point that the optical measurements were performed using a metal chimney instead of a plastic one that was used throughout our experiments. This change though is estimated to have only a slight effect on the structure of the flame, mainly because of the distance of the chimney walls from the flame (~8 burner radii).

For particles in the Rayleigh regime ($D<\lambda/10$; D particle diameter, λ wavelength of incident beam), the value of the volumetric scattering cross section for incident and scattered rays polarized in the vertical plane is given by

$$Q_{vv} = \frac{F(\tilde{m})}{4} \left[\frac{\pi}{\lambda}\right]^4 N \int_0^\infty P(D)\, D^6\, dD \qquad (2.1)$$

where

$$F(\tilde{m}) = \left| \frac{\tilde{m}^2 - 1}{\tilde{m}^2 + 2} \right|^2 ,$$

and P(D) is the particle size probability function $\left[\int_0^\infty P(D)\, dD = 1\right]$, $\tilde{m}$ the complex refractive index of the particulate material and N the total number of particles per unit volume. The product P(D) dD expresses the fraction of all particles contained in the interval D to D+dD. The extinction coefficient in the Rayleigh limit is given by

$$K_{ext} = \frac{\pi^2}{\lambda} E(\tilde{m})\ N \int_0^\infty P(D)\ D^3\ dD \tag{2.2}$$

where

$$E(\tilde{m}) = -\mathrm{Im}\left[\frac{\tilde{m}^2 - 1}{\tilde{m}^2 + 2}\right]$$

A parameter thoroughly used in the optical method, called generalized mean diameter or moment ratio, is defined by

$$D_{pq}^{\ p-q} = \frac{\int_0^\infty P(D) D^p\, dD}{\int_0^\infty P(D) D^q\, dD} \tag{2.3}$$

The particle volume fraction ϕ, defined as the volume concentration of the particulate material inside the host gas, is related to K_{ext} through

$$\phi = \frac{\lambda\ K_{ext}}{6\pi\ E(\tilde{m})} \tag{2.4}$$

From Eqs. (2.1) and (2.2) using the definition of Eq. (2.3) we obtain

$$D_{63} = \lambda \left[\frac{4}{\pi^2} \frac{E(\tilde{m})}{F(\tilde{m})} \frac{Q_{vv}}{K_{ext}} \right]^{1/3} \tag{2.5}$$

If

$$f_N = \left[\frac{D_{63}}{D_{30}} \right]^3 \tag{2.6}$$

and since $$\phi = \frac{\pi}{6} N D_{30}^{\ 3}$$

we obtain the following expression for the number concentration

$$N = \frac{6\phi}{\pi D_{63}^{\ 3}} f_N \tag{2.7}$$

All three Eqs. (2.4), (2.5) and (2.7) are valid independently of the form of P(D), provided that the particles belong to the Rayleigh regime. An assumption for the value of $\tilde{m}$ is required in order to calculate ϕ and D_{63} from Eqs. (2.4) and (2.5) respectively. An additional assumption is required for the value of f_N, in order to obtain the values of N from Eq. (2.7). The assumed value of f_N is directly related to the form of the distribution as we can see from Eqs. (2.3) and (2.6). The optical measurements discussed here used a value of $\tilde{m} = 1.57 - 0.56i$. A different value of $\tilde{m}$ would affect the values of N by a significant factor, while the values of ϕ and D_{63} would be

less influenced[84,85]. The value of f_N was taken to be equal to 2.0 corresponding to the self-preserving distribution function[37], which is the asymptotic form of the particle distribution function for an aerosol undergoing free molecular coagulation by Brownian motion in the absence of particle formation or surface growth.

Soot volume fraction, particle size and number concentration measurements for the ethene flame are shown in Figure 2.2 for two heights (z=15 and 50 mm). Only the labeled profiles are of interest for our work, since the rest correspond to other flames studied by Santoro et al[85]. The soot volume fraction at each height achieves a maximum value at a radial location r_c defining the annular region. This maximum value steadily increases up to a height of 40 mm, reaches a maximum between z=40 mm and z=50 mm and then decreases probably through oxidation. The central region of the flame (r=0) is first observed to contain particles at an axial location which is significantly higher than that observed for the annular region. The regions of maximum ϕ coincide with the regions of large particle size and almost a constant N higher up in the flame. However in the lower part of the flame the maxima of ϕ and D_{63} coincide with the occurrence of a minimum of N. A tentative explanation for this seemingly paradoxical behaviour is given in the last chapter of the current work.

A shown by Fig. 2.2b the particles start at a lower size down low in the flame and grow as they move upwards. The two main mechanisms of growth (agglomeration and surface growth) account for the steady increase of the particle size. The increase of ϕ with height may be due to particle

inception or surface growth mechanisms. The optical tests do not provide information about neither the existence nor the relative contribution of these processes to the soot loading. The region of smaller particles and large number concentration moves closer to the center line with increasing height. The particles grow during this stage and their number concentration decreases probably through agglomeration. Particle oxidation processes finally cause the cessation of the growth mechanisms as the particles move toward the upper portions of the flame. As we see the particle sizes in the intermediate and higher portions of the flame grow larger than 100 nm. This implies that the particles do not belong to the Rayleigh regime thus indicating that the profiles there are not as reliable. However low in the flame the particle sizes are clearly in the Rayleigh limit. A test of the applicability of Rayleigh theory is performed by measuring R_{ij}, defined as the ratio of the scattering coefficients for two different angles θ_i and θ_j, i.e.

$$R_{ij} = \frac{Q_{vv}(\theta_i)}{Q_{vv}(\theta_j)}$$

When $D/\lambda \leq 10$ it should be $R_{ij} \approx 1$. A series of values of R_{ij} for three different scattering angles ($\theta_1=45^\circ$, $\theta_2=90^\circ$ and $\theta_3=135^\circ$) at the position of maximum volume fraction is given in the following table reproduced from ref. 84.

TABLE 2.1

Experimental Light Scattering Ratio Measurements[a]

Height z (mm)	7	10	30	50
R_{12}	1.06	1.1	2.2	2.3
R_{13}	1.28	1.4	4.0	4.2

[a] From ref. 84

It is clear that low in the flame $R_{ij} \approx 1$, while higher up $R_{ij} > 1$ thus invalidating the adoption of Rayleigh theory.

The depolarization ratio ρ_v is defined as the ratio of the energy flux scattered in the horizontal plane (Q_{hv}) to that in the vertical plane (Q_{vv}) when the incident light is vertically polarized. The depolarization ratio is zero if the scatterers do not exhibit any material and/or geometrical anisotropy. From the optical measurements we can construct the following table

TABLE 2.2

Experimental Light Scattering Coefficient and Depolarization Ratio Measurements

	z = 30 mm		
	Q_{hv}	Q_{vv}	ρ_v
$r>r_c$	2×10^{-5}	3×10^{-3}	0.0067
$r=r_c$	3×10^{-4}	1.5×10^{-2}	0.020
$r<r_c$	3×10^{-5}	1.8×10^{-3}	0.017

As we see, at a height z=30 mm there is a drastic decrease of ρ_v from r_c to $r>r_c$ (factor of 3). The value of ρ_v at $r<r_c$ is comparable to that corresponding to the annular region. This behaviour of ρ_v is discussed in Section 3.6.

The optical method also provided data on the fluoresence cross section Q_F at a wavelength of 514.5 nm, using a laser line at 488.0 nm as the excitation source. The fluorescence profiles were found to be broader than

the Q_{vv} profiles, extending closer to the center line. The maximum number concentration in the central core coincides with the maximum fluorescence level. It was also found that low in the flame (z<5mm) the Q_{hv} signal was due almost entirely to fluorescence. The fluorescence signal shifts towards the center line with increasing height until the entire central part of the flame exhibits fluorescence. A very similar fluorescence has been observed in premixed flames of various fuels[43] as well as in other diffusion flames[69], and has been attributed to various polycyclic aromatic hydrocarbons[13,75]. However the existence of other fluorescing molecules (polyenes and polyynes according to Smyth et al.[90]) which seem to be unconnected with the soot formation processes can not be excluded.

A study of the velocity and temperature fields of the ethene flame was performed by Santoro et al[86]. The axial (v_z) and radial (v_r) components of velocity are shown in Figure 2.3. For heights below z=20 mm both v_r and v_z exhibit a maximum in the annular region of the flame. The strong entrainment of air inside the flame at these heights is indicated by the substantial radial velocity component. Mitchell et al.[72] reported similar behavior in the lower portions of the axisymmetric laminar methane diffusion flame they studied. A strong acceleration of the flow along the z-axis is apparent throughout the flame showing the strong effect of buoyancy forces.

Temperature profiles were obtained using fine wire thermocouples. The uncorrected temperatures are shown in Figure 2.4 for various heights. An estimate of the radiation corrections for the thermocouple measurements in a methane diffusion flame is given in ref. 90. This correction is of the order of 5% and is not expected[8] to be very different for the ethylene flame studied.

Comparing the profiles of ϕ and T we see that the temperature maxima correspond to radial positions larger than r_c. The radial distance between the positions of ϕ_{max} and T_{max} varies from 1 to 2 mm.

According to Mitchell et al.[72] the luminous flame surface shown in Figure 2.5 marks the fuel rich side of the reaction zone, which is defined as the zone corresponding to the maximum temperature. This reaction zone has a blue hue the intensity of which decreases with increasing height above the burner mouth (not visible above z=5 mm). The fuel lean side of the reaction zone is dominated by the burnout of CO and represents a surface through which oxygen diffuses to the fuel rich side. The minimum concentrations of oxygen and the fuel exist on the reaction zone (T_{max}), where the products of the combustion exhibit their maximum concentrations.

Santoro et al.[86] used the particle velocity measurements to determine particle paths (trajectories) inside the flame. The particle trajectories are influenced by thermophoresis because of the presence of high temperature gradients inside the flame (as high as 400 K/mm). These gradients give rise to thermophoretic velocities up to 4 cm/sec which tend to transport the particles into the interior of the flame. However when compared to the convective velocities, the thermophoretic velocities are much lower in magnitude higher in the flame and are more important at lower axial locations. The particle paths calculated for the ethene flame are shown in Figure 2.6A. Using the calculated path lines and the velocity field measurements, Santoro[81] related each position in the flame to a residence time. The exit plane of the fuel nozzle was used as the initial particle location.

The residence time is plotted in Figure 2.6B as a function of the two coordinates used (z,r). This figure was used to transform spatial dependence of various variables such as ϕ, D_{63} and N, to residence time dependence. Figure 2.7 shows soot volume fraction, particle size D_{63} and particle number concentration N, corresponding to the region of maximum ϕ as functions of the residence time. Only the curves labeled 3.85 cc/s are the ones related to our current work. These profiles were calculated by Santoro using Mie scattering analysis for a self-preserving distribution of polydisperse spheres[20], which is less limited compared to Rayleigh theory but involves more computational difficulties. It is apparent from Figure 2.7b that the particles grow traversing through the low and intermediate regions of the flame. At the same time the number concentration decreases through agglomeration, up to the point where oxidation mechanisms take over. From then on, ϕ and D_{63} decrease, while N is observed to decrease as the particles move into the oxidation zone. This behavior of the number concentration is different from what Kent and Wagner[52] found for a laminar ethylene diffusion flame based on a Wolfhard-Parker burner. They concluded that the number density at the region of maximum ϕ remains invariant with height.

The information provided by the optical data is used in the third chapter of the current work in combination with the results obtained by our thermophoretic method, in order to examine the aerosol dynamics of the soot aerosol in the laminar axisymmetric ethene diffusion flame under investigation.

CHAPTER 3

EXPERIMENTAL

A novel experimental apparatus was designed to probe an axisymmetric laminar ethene-air diffusion flame at atmospheric pressure. The same flame was extensively studied by optical methods[83,84,86] and a wealth of data was produced as a result of these studies. The thermophoretic method presented here complements the optical method providing useful information on the morphology of the soot particles throughout the flame. The combination of the two methods can contribute to a qualitative understanding of the complicated phenomena associated with the soot formation processes. In the first part of this chapter the theoretical background is given for a thorough understanding of the thermophoretic mechanism that drives the soot particles to the sampling surface. In the latter part the apparatus used is described and the experimental procedure of the sampling method is presented in detail.

3.1 Thermophoretic probes

Small particles inside a nonisothermal environment are driven from the high to the low temperature regions. This phenomenon of particle transport down the temperature gradient was given the name thermophoresis, which literally means being carried by heat. Many particle sampling methods are based on the thermophoretic mechanism. More recently the role of thermophoretic deposition[24,35,79] has provided a quantitative understanding of the drift of particles across the boundary layer to a surface that is at a lower temperature than the surrounding gases. This principle has been used extensively[49,74,76,80,88,95] to collect soot particles from a flame environment on cold surfaces for subsequent analysis by electron microscopy.

The thermophoretic deposition is driven by the presence of a temperature gradient in the vicinity of a cold wall inside the flow field of a particle-laden gas. This gradient is readily established by introducing briefly into the hot flame gases a probe surface which is initially at room temperature. The probe exposure time τ_e should be long enough to capture a significant sample but short enough to present a cold surface to the flame-born particles. This cold surface serves a second important role which is that it freezes heterogeneous reactions of the particles that are already captured. This chemical freezing action inhibits changes in the soot morphology after the particles have impacted upon the cold surface.

The sampling surfaces employed in this work are the two devices that are used to hold specimens in electron microscopy as well as modified versions of these materials. These devices are the widely used circular perforated grid of 3.05 mm diameter and the bulk specimen carrier, a thin strip of metal with dimensions 11.0x3.5x0.1 mm, used to examine bulk specimens through scanning electron microscopy (SEM). The more familiar porous grid, Figure 3.1a, is advantageous for transmission electron microscopy (TEM) work, especially when it supports a 200 Å thick film of elemental carbon or silicon monoxide (SiO). These films are deposited on the grids by low pressure evaporative deposition and are commercially available in a wide variety of dimensions of the supporting grid. The carbon films are extremely stable under the electron beam, possess a fine background structure giving high-resolution capabilities, and have a composition closely related to that of the soot particles. Carbon films however are readily oxidized in the flame environment and therefore can be exposed only for very short time intervals. Films of SiO

are generally more durable but tend to produce a lower background contrast. Two different kinds of grids, supplied by Ernest F. Fullam Inc., Latham NY, were used in the tests. These were the 200-mesh copper grids, made up of 40 μm bars forming 85 μm square holes and the 400-mesh copper grids made up of 33 μm bars forming 30 μm square holes.

The image quality produced by photographing soot particles captured on carbon substrates is very high and good particle statistics are potentially obtainable from the electron micrographs. A disadvantage of the porous grid is its inability to afford good spatial correspondence between the flame position examined and the electron micrograph coordinates. Nevertheless position correspondence to about 1.0 mm between flame and micrograph coordinates is achievable with this device.

The bulk specimen carrier shown in Figure 3.1b, is a thin strip of metal which can be used to provide better position correspondence by aligning its edge with the flame axis as illustrated in Figure 3.2. This figure shows a schematic diagram of the probe inserted into the diffusion flame, and the burner based coordinate system applicable for our experiments. The bulk specimen carrier is commercially available by Philips Electronic Instruments Inc. (part no. PW6156/00). The material of the carrier is an alloy of copper, nickel and zinc. The original carrier was used initially to sample the particles from the interior of the flame. However the smooth surface of the probe was oxidized during the exposure to the hostile flame environment thus limiting the capabilities of the SEM observations. In order to provide a chemically inert surface to capture the particles, the carrier was coated with a gold layer of

nominal thickness of 200 Å. The distance from the end of the carrier when placed in the microscope provides a reference to link the flame radial position and the micrograph coordinates to within about 0.2 mm. Magnifications up to 50,000 with adequate resolution are obtainable in the SEM mode. A disadvantage of the use of the bulk specimen carrier is that it allows only SEM observations which provide poor image quality (low contrast) of the low-density soot particles and does not yield quantitative information on the particle morphology.

Modifications of these probes have been made in order to combine the unique advantages that each affords. The first modification consists of replacing a sector of the specimen carrier with a 200-mesh nickel screen (type I probe in Figure 3.1c). The grid material is coated with a carbon film by evaporative deposition after being bonded to the modified carrier using epoxy cement. This probe offers good position correspondence between flame and micrograph coordinates as well as the high image quality afforded by TEM. The relatively large screen surface makes this probe fragile and more difficult to fabricate and coat uniformly. For this reason the carbon layer was supported by a thin formvar (polyvinylformal) film of 200 Å nominal thickness. The formvar films have a tendency to shrink slightly when first irradiated but when stabilized with an ultrathin carbon coating, are more resilient than carbon alone and very stable under the electron beam. When it is imperative that only pure carbon is present in the substrate material, the formvar can be removed by immersion in chloroform. The carbon films on the type I probes were manufactured by Ted Pella Inc., Tustin CA, and the formvar film was not removed since the probes had to sustain high acceleration forces during the sampling procedure. Comparisons of particles

collected on these probes and on pure carbon coated grids showed no influence of the formvar film on soot morphology.

A second modification consists of a carrier through which a slot has been milled (type II probe in Figure 3.1d). Conventional coated grids are bonded to the carrier with epoxy cement to provide a durable and more easily constructed probe. This probe has a larger thermal inertia than the type I probe, is inexpensively fabricated from the commercially available carbon-coated circular grids and the bulk specimen carrier, and is highly durable.

A third modification of the carrier is shown in Figure 3.1e (type III probe). A strip of the original carrier was removed along the probe thus providing a sharp edge as a stagnation flow collector. This probe affords high spatial positioning but gives information only on the primary particle size. The state of agglomeration is not revealed by the edge probe because of the high rate of deposition at a stagnation point.

A combination of the previous probes is shown in Figure 3.1f (type IV probe). A carbon coated grid was bonded to the carrier at a certain distance from the tip of the probe. This probe combines two different sampling surfaces that collect particles corresponding to a certain axial location (z) above the mouth of the burner.

The modified versions of the specimen carrier could not be accommodated by the appropriate specimen holder used to perform SEM observations on the original probe. In order to use TEM to examine the

modified probes some simple alterations of the holder were made. The soot samples collected on the probes have been examined on a Philips 420 Scanning Transmission electron microscope operating in either the SEM or the TEM mode. This instrument provides magnifications as high as 820,000 and possesses a point-to-point resolving power approaching 0.3 nm in the TEM mode. This capability is adequate to resolve the soot particles except in the very lowest portion of the flame where the smallest discernible size is determined by the instrument resolving power. Soot particles of 1-2 nm would be discernible, but smaller particles could be indistinguishable from the grainy background structure of the carbon substrate.

3.2 Boundary layer studies of the flow field around the probe

A numerical investigation of the flow field around the probe was performed using a computer program called FLUENT, developed by Creare Inc., Hanover NH, solving the Navier-Stokes equations without any approximations. The problem considered is the two dimensional steady flow around a flat plate of finite dimensions, maintained at a constant temperature different than that of the surrounding fluid. This is a first approximation to the actual 3-D unsteady flow problem around the specimen carrier inserted into the flame. The thermodynamic properties of the combustion gases were approximated by those of nitrogen which was considered an ideal gas. The heat capacity dependence on temperature was expressed as a polynomial function of T. Data were obtained from the JANAF tables[50], while viscosity and thermal conductivity data were taken from Svehla[91]. The free stream gas velocity and temperature were U=0.7 m/s and T_∞=1700 K respectively (characteristic[86] of the flame environment at an axial location z=10 mm) while

the probe temperature was taken T_w=380 K from probe temperature measurements at the same z. At this location we calculated a Reynolds number $Re_L \approx 9$ based on the streamwise dimension of the plate probe, i.e. L=3.5 mm. The numerical solution allows the full thermal boundary layer to be calculated. Figures 3.3A and 3.3B show the temperature and velocity contours around the probe. We define the thermal boundary layer by the isotherm T_{bl} such that T_{bl}/T_∞=0.9. It is clear from Figure 3.3A that the thermal boundary layer thickness δ_t, at the low Reynolds numbers characteristic of the problem, is rather larger than expected (typical value δ_t~2.3 mm halfway along the probe, i.e. x= L/2). The calculation of δ_t permits the particle trajectories to be calculated as well. The trajectory shown in Figure 3.3 is that corresponding to a particle ultimately captured at x=L/2.

A time scale of importance, the quench time τ_q, is the time required for a soot particle to traverse from the hot flame gases to the cold probe surface through the thermal boundary layer. Figure 3.3C shows a typical particle P traversing the distance between two neighboring isotherms T_n and T_{n+1}. The thermophoretic velocity V_t is perpendicular to the fluid velocity $U_{n,n+1}$ giving a total velocity vector $\overline{V}$ toward the probe surface. The time required for the particle to move from P to P' is given by

$$\Delta t_{n,n+1} = \frac{(PM)}{U_{n,n+1}} \tag{3.1}$$

where (PM) is the distance traversed by the particle along the x-direction during the motion from P to P'.

The thermophoretic velocity driving the particles of all sizes is given by

$$V_t = -K\nu \frac{\nabla T}{T} \tag{3.2}$$

where ν is the kinematic viscosity of the gas mixture, and T is the local temperature. The thermophoretic velocity coefficient K depends on the Knudsen number, defined by

$$Kn = \frac{\lambda}{R} \tag{3.3}$$

where λ is the mean free path of the gas and R is the radius of a particle. According to Talbot et al.[92], the values of K are 0.30, 0.51, 0.54 and 0.55 for Knudsen numbers of 0.1, 1.0, 10. and 100. respectively. Thus for particles in the free molecular regime ($Kn \gg 1$) $K = 0.55$. For particles in the transition regime ($Kn \approx 1$) the value of K is comparable to that of particles in the free molecular regime. A typical value of λ for the ethylene flame studied is within the range of 400 nm to 600 nm. From our previous studies[21,22] the largest soot aggregates were found to be as long as 300 nm. These particles belong to the transition regime but according to the above results, have almost the same thermophoretic velocity with the smaller particles which belong to the free molecular regime. This guarantees the absence of preferential deposition of particles of different sizes since they undergo similar theromophoretic transport inside the flame environment.

The temperature gradient in Eq. (3.2) can be approximated by

$$\nu \frac{\nabla T}{T} \approx \nu_a \frac{T_{n+1} - T_n}{(PN)\ T_a}$$

where (PN) is the distance between the isotherms T_n and T_{n+1} along the y-direction, $T_a=(T_n+T_{n+1})/2$, and ν_a is the kinematic viscosity of the gas mixture at T_a. Equation (3.1) was used to calculate the values of $\Delta t_{n,n+1}$ after graphical evaluation of (PM) from the contours in Figures 3.3A and 3.3B. The quench time is then given by

$$\tau_q = \sum_n \Delta t_{n,n+1} \tag{3.4}$$

Using the values corresponding to the characteristics of the soot field at z=10 mm we estimate from Eq. (3.4) τ_q to be approximately 10ms. The total distance along the x-direction, traversed by a typical particle collected at x=L/2 at the same height during the penetration through the thermal boundary layer, was estimated to be $\delta z \approx 2.3$ mm. This means that the particle ultimately captured at z=10 mm entered the thermal boundary layer caused by the plate probe at a height of z=7.7 mm. Thus the quenching effect of the probe, being felt by particles entering the thermal boudary layer, occurs at a relatively large distance (δz) upstream the flow field of the combustion gases low in the flame. However higher in the flame the thermal boundary layer is expected to be considerably thinner because of the higher velocities. A lower value of δ_t would increase the thermophoretic velocities which means that δz should be significantly reduced. For the type I and IV probes the value of δz for particles captured at a particular axial location is expected to be very low because of the small values of δ_t around the grid material. For the stagnation point probe (type III) δz is expected to be minimal throughout the flame.

Another time scale of importance is the disturbance time τ_d, which is defined as the time required for the flow field around the probe after its

insertion to achieve velocity values equal to 90% of the values corresponding to steady flow conditions. Under the assumption of instantaneous insertion of the probe inside the flame environment we calculated $\tau_d \approx 3.5$ ms, corresponding to conditions characteristic of the annular region at a height z=10 mm. The actual sampling times employed throughout the current work were longer than 30 ms. This suggests that the effect of the transient disturbance introduced by the motion of the probe to the flow field around it should by very low.

3.3 Thermophoretic studies on soot particle transport

The theoretical description of the thermophoretic transport of particles is provided by the analysis of the particle drift across a thermal boundary layer formed over a solid surface in a particle-laden, hot gas stream[24]. Assuming spherical particles of uniform diameter D_p in the free molecular regime, this analysis provides the particle flux to the cold wall as

$$J_w = \frac{6K\nu_e f_{v,e}}{\pi D_p^3} \left[\frac{T_w}{T_g}\right]^{\kappa} \frac{1}{T_g} \frac{dT}{dy}\bigg|_w \qquad (3.5)$$

where J_w is the particle number flux, K is the thermophoretic velocity coefficient, ν_e is the kinematic viscosity of the host gas mixture at the outer edge of the gas thermal boundary layer, $f_{v,e}$ is the particle volume fraction at the outer edge of the gas thermal boundary layer, D_p is the particle diameter, T_w, T_g are the wall and carrier gas temperatures, κ is the exponent appearing in the dependence of gas mixture thermal conductivity on temperature ($\kappa \approx 0.84$), and $(dT/dy)|_w$ is the temperature gradient in the

cross stream direction at the wall. We approximate

$$\left.\frac{dT}{dy}\right|_w \simeq \frac{T_g - T_w}{\delta_t}$$

where δ_t is the thermal boundary layer thickness. Then

$$J_w = \frac{6K\nu_e f_{v,e}}{\pi D_p^3 \delta_t}\left[\frac{T_w}{T_g}\right]^K \left[1 - \frac{T_w}{T_g}\right] \tag{3.6}$$

We can then estimate the required exposure time τ_e, here defined as the time required for a 10% surface coverage of the bulk specimen carrier by soot particles, to be given by

$$\tau_e = \frac{0.4}{\pi J_w D_p^2} \tag{3.7}$$

Using in Eqs (3.6) and (3.7) values corresponding to the characteristics of the soot field at z=10 mm, i.e., $K \simeq 0.55$ for free molecular flow[35,92], ν_e=2.81 cm^2/s corresponding to air at T_g, $f_{v,e}=1.8\times10^{-6}$ cm^3/cm^3 and T_g=1700 K from ref. 86, T_w=380 K from probe temperature measurements, D_p=13nm from ref. 22 and δ_t=0.23 cm from the previous chapter, we estimate τ_e to be of the order of 32 ms. In practice exposure times of that order or slightly longer are employed. It should be mentioned that Eq. (3.6) is based on the assumption that the aggregated particles are small compared with the mean free path of the gas molecules. This condition is fulfilled in most regions low in the flame.

3.4 Probe control system and burner

The probe control system and the related equipment is shown in Figure 3.4. The precise spatial positioning of the probe within the flame is achieved by mounting the mechanical components on a rigid aluminum table. The burner (a) with the chimney (b) and the flow restrictor (c) are securely held by a post (d) with a vertical screw drive mechanism. The vertical adjustment of the probe with respect to the burner mouth is measured by a cathetometer, and changes in the height above the burner are measured by means of a dial indicator (e). The vertical position control of the thermophoretic probe is about 0.1 mm.

The ideal probe control system would instantaneously insert the thermophoretic probe into the flame for a well defined, controllable time interval without causing any disturbance to the motion of the flame gases. The actual probe control system has been designed and calibrated to move the probe with the maximum speed to a precisely defined position in the flame. The mechanical actuator for this system is a double-acting pneumatic cylinder (g) of 14-mm diameter and 25-mm stroke that is driven by an air pressure of 4.5 atm through a pneumatic directional control valve (h). A translation potentiometer (j) supplied by SERVONIC, Costa Mesa CA, is mounted on the piston shaft and provides a precise record of the probe trajectory on the screen of a storage oscilloscope (k). The potentiometer is connected in series with a D.C. power supply (1.5V) and the oscilloscope. The motion of the shaft during the sampling procedure causes a variation of the resistance of the potentiometer, thus changing the voltage signal forwarded to the oscilloscope. The linear character of the circuit allows an excellent correspondence between

the position of the piston shaft and the time variation of the recorded oscilloscope signal. The reproducibility of the probe trajectory with a specified setting of the valve-timing circuit (i) proved to be very good. With this configuration we have been able to achieve transit times τ_t for the entry of the probe into the flame equal to 12 ms. The exposure time of the probe to the flame environment is controllable and can be reduced to as short as 30 ms. The entire probe trajectory is recorded by the linear transducer during each test. Figure 3.5 shows the probe trajectory and documents the brevity of the transit time as well as the precise spatial definition of the residence time.

The burner is identical in design with that used previously[85,86] for the extensive laser scattering and transmission measurements on the ethene coannular diffusion flame. A cross sectional drawing of the burner is shown in Figure 3.6. The burner brass tube (a) has a 11.1 mm i.d. and is surrounded by the outer brass tube (b) of 101.6 mm i.d. An evenly-spaced, 14-mesh ceramic honeycomb (c) fills the annular space. The fuel tube extends 4 mm above the top of the burner. An airflow through the ceramic provides the coannular air stream which overventilates the diffusion flame. A mixing chamber (d) in the middle of the burner is filled with 3-mm glass beads (e), to eliminate nonuniformities in the air flow field. Just below the glass bead chamber there is a preliminary air chamber (f), supplying the air uniformly toward the upper parts of the burner arrangement. The two chambers are separated by the distributor plate (g) which is a blockage plate with the purpose to begin the process of achieving a uniform air flow. The beads are prevented from penetrating through the holes of the distributor plate to the preliminary air chamber using a fine screen (h). The burner is shielded from laboratory air currents with a 420-mm long plastic transparent chimney (i) supporting a flow

restrictor plate (j) in order to reduce any air recirculation in the system. The flow restrictor consisted of a 143-mm diameter porcelain plate with a 23-mm diameter center hole and concentric rings of 5-mm diameter holes. The chimney could slide along the outside of the burner so only one hole provided access to all the axial locations of the diffusion flame.

CP-grade ethylene (99.5% pure) and compressed dry air (maximum moisture 3 ppm) were directed to the burner system. Both gases were supplied by LINDE specialty gases. Throughout the tests reported herein, the volume flow rates of ethene and air duplicated the values used at NBS namely 3.85 cm^3/s and 713 cm^3/s respectively. These flow rates were measured with rotameters, which were calibrated for each fuel using a soap bubble technique. Using these flow rates upon ignition, a flame of definite shape and height (88 mm) resulted[85]. This flame displays the bright yellow incandescence characteristic of soot but releases no soot to the surroundings.

A series of high-speed cine photographic studies were conducted to determine the influence of the probe motion on the flame. These tests showed that the probe enters the flame very smoothly but a flow induced by the probe support rod distorts the flame severely after the probe motion has ceased. This unsteadiness of the flame position destroys the position correspondence between flame and micrograph which has been a goal of our effort. To prevent the bending of the flame we have added a flow deflector plate, shown schematically in Figure 3.2, through which the probe enters the flame. The deflector plate remains stationary in space thus deflecting any air current induced by the motion of the probe support. Cine photography of the

probe equipped with the flow deflector shows the flame to be perfectly steady throughout the time period during which the probe is in motion. The flow deflector plate is always positioned parallel to the luminous envelope of the flame in order to minimize interference with the combustion processes. The distance of the plate from the luminous flame envelope is 4-5 mm which proved to cause no disturbance to the appearance of the flame. Macroscopically the insertion of the probe during the sampling procedure, was accompanied by the appearance of a thin long dark streak down stream the flow of the combustion gases. This streak appears as a discontinuity of the luminous zone of the flame, which starts from the position of the probe and continues to the tip of the flame. This phenomenon is probably a result of the quenching effect of the cold probe to the flame reactions. However the consistency of the results shows that the effect of this disturbance is not felt upstream by the soot particles ultimately captured on the probe.

The maximum temperature of the carrier probe during the sampling has been measured by means of temperature-indicating liquids supplied by OMEGA Engineering Inc., Stamford CT. At z=10 mm above the burner mouth, where gas temperature has reached a local maximum[86] as high as 2000 K, the carrier probe reaches a temperature of 385±10 K when the residence time is 65 ms. In an equal time period the grid material would assume a higher temperature since its thermal inertia is substantially lower. These tests also showed that the probe is subject to significant radiant heating prior to insertion into the flame unless a protective flow of cold air in the probe support annulus is sustained during this period. This cooling air flow is turned off about 1 sec before the extension of the probe. The high speed photographic studies proved this time to be adequately long for the flame to

recover from its influence. The transient burner mouth temperature was also measured immediately after ignition in order to determine the warm-up time of the system. A J-type thermocouple was used with a 1-mm diameter bead which was adjusted on the outer surface of the fuel tube 1 mm below the burner lip. The readings were recorded every one minute after ignition (t=0) until steady state. This procedure showed that the system reaches a steady state after 6 min. The transient temperature of the surface of the flow deflector plate was also recorded when the deflector was positioned in place at an axial location z=20 mm above the burner mouth. These measurements verified the previous warm-up time of 6 min which was adopted throughout our studies.

3.5 Experimental results and discussion

The thermophoretic sampling technique described previously in detail, was used to study the morphology of soot aggregates collected from the coannular ethene diffusion flame. These aggregates consist of individual particles, called primary particles, of approximately spherical shape and rather uniform size. Our observations of the diffusion flame generated soot are consistent with the long established fact of the uniformity of the primary particle size per aggregate in the carbon black industry. According to a series of studies[18,62,66] the distribution of the primary particles sizes is generally much narrower within a single aggregate than in the sample as a whole. The term aggregate is used from now on to depict a discrete, rigid entity composed of extensively coalesced primary particles fused together. The aggregates are highly rigid and stable under the high-energy electron beam (accelerating voltage of 80 KV) during the EM observations.

There is a difficulty in sampling the soot aerosol in the fuel-rich region of the flame. This region is surrounded by an annulus (~2mm thick) of high soot volume fraction[85] that peaks at $r=r_c$ (annular region). The value of r_c decreases with increasing height, as shown in Figure 3.2. The probe surface sampling the regions corresponding to $r<r_c$ can be contaminated by particles from the region of high soot volume fraction during insertion. This suggests that observations of the morphology of particles collected at $r<r_c$ must be very carefully examined for the presence of soot originating from the annular region. The soot material samples from $r \geqslant r_c$ are free of such contamination.

A vertical survey of primary particle size has been performed using various probes positioned inside the flame for exposure time τ_e varying from 30 to 120 ms. The longer probe exposure times were used at low regions of the flame, since the soot volume fraction there is considerably lower than that higher in the flame. However these long exposure times (~100 ms) were associated with partial oxidation of the carbon substrate. The micrographs examined were taken from the undamaged regions of the film. Analyzing the soot samples collected this way, we were able to verify the thermophoretic effect on particle deposition inside a flame environment. This effect is clearly shown in Figure 3.7, depicting soot aggregates collected on a carbon-coated grid from a height of z=30 mm. It is obvious from Figure 3.7 that the particle concentration is higher in the vicinity of the grid bar which is playing the role of the cold target attracting the particles.

A series of TEM micrographs reproduced in Figure 3.8 shows typical particles which are present near $r=r_c$ for the indicated values of height z. It

must be pointed out here that particle deposition occurs on both sides of the film. However, as Figure 3.8 shows, the low coverage of the film surface by soot aggregates, as well as the narrow depth of field at these microscopic scales, would clearly discern the majority of the particles deposited on opposite sides of the substrate. Based on an examination of these and similar micrographs we come to the following conclusions. Large aggregates dominate the particle morphology at the annular region of the flame at all heights. These aggregates consist of primary particles of rather uniform size at low and intermediate heights. The primary particle size strongly increases as the particles move toward higher regions of the flame (Figure 3.8A-D). These observations clearly indicate the dominant effect of surface growth on soot morphology at low and intermediate heights of the flame. The initial effects of soot particles oxidation are apparent from a height of z=40 mm (Figure 3.8 E) and above. Large aggregates of considerably smaller but uniform primary particle size are apparent. As the particles move toward the highest regions of the flame, these large clusters dominate showing a smaller primary particle size and a higher degree of agglomeration (Figure 3.8F). This dramatic decrease of the primary particle size with increasing height above the burner shows the effect of the oxidative mechanisms on the particles as they move toward the tip of flame.

A detailed examination of the micrographs of Figure 3.8 provides some information on the contributions of agglomeration and surface growth on the soot growth mechanisms in our diffusion flame system. Low in the flame (z<10 mm) there exist intense particle inception and intense agglomeration. This causes a rapid broadening of the size distribution and a reduction of the number concentration of aggregates immediately after the cessation of the

particle inception pulse. At intermediate heights of the flame the number concentration has decreased through agglomeration (Figure 3.9A), and surface growth (Figure 3.9B) becomes the dominant phenomenon. Heterogeneous reactions result in material deposition on the exposed surfaces of the primary particles that make up the aggregates, thus retaining their nearly spherical form while growing (Figure 3.9C). The uniformity of the primary particle size is thus maintained, since all the particles forming an aggregate are exposed to an environment that is locally uniform within the scale of the size of the aggregate. This growth mechanism is compatible with the series of micrographs of Figure 3.8 and it also agrees with Tesner's observations on thermal decomposition of hydrocarbons on carbon black aggregates[93].

The above observations were repeated with identical results, by performing the same measurements with the use of SiO-coated grids. There was no obvious dependence of primary particle size on the substrate material. Measurements were also performed with various exposure times (30-90 ms) of the carbon coated grids within the flame at a specified height of z=20 mm. The grids were inserted vertically inside the flame in order to minimize the distrubance introduced by the probe to the flow field of the combustion gases. Figures 3.10 and 3.11 show soot particles collected from the annular region of the diffusion flame at z=20 mm using various exposure times of the grids. No change of either the primary particle size or the degree of agglomeration with time is apparent. Some signs of oxidation of the carbon substrate are apparent in Figure 3.10C and D as well as in Figure 3.11C and D. The oxidation is probably associated with the long exposure times (70 and 90 ms) which result in the appearance of nonuniformities on the substrate background. No signs of oxidation are observed for shorter probe exposure times (τ_e=30 and

50 ms). The above observations lead to the conclusion that changes of the primary particle size or the degree of agglomeration do not take place on the probe, provided that the probe surface coverage by the particles is of small order, 10% or less. When the coverage is higher no positive conclusion about the degree of agglomeration can be drawn since some of the aggregates may overlap.

Further support for the conclusion of no agglomeration on the probe is provided by sampling a methane diffusion flame where soot concentrations are dramatically lower[86] (factor of 10-15 in soot volume fraction). The flame probed was based on the same coannular burner described previously in detail. A methane flow rate of 5.49 cm^3/sec was used while the ventilating coannular air flow rate was 784.5 cm^3/sec. These flow rates produce a flame of 55 mm height which displays the yellow incandescence characteristic of soot. Figure 3.12 shows the particle morphology as a function of the radial position r for the methane diffusion flame at two different heights (z=15 mm and z=25 mm). Very small aggregates and single particles are present low in the flame as shown in Figure 3.12C and D. Larger aggregates are formed higher up as shown in Figure 3.12A and B. At both heights the micrograph on the left hand side corresponds to the annular region of the flame. It is also apparent from these figures that the particles outside of the annular region are far less agglomerated and display a substantially smaller primary particle size (Figure 3.12B and D). The above observations prove that agglomeration on the probe does not occur in the case of the methane-air diffusion flame.

Examining a series of electron micrographs at different heights on a SMI Micro-comp data acquisition system, we were able to produce quantitative

data on the primary particle size distribution as a function of height z above the burner, for particles collected from the annular region of the flame using various probes. With the use of a digitizing tablet the primary particle diameter of about 100 particles at each height was measured. A basic statistical analysis at each height, performed by the same system, produced the mean value D_p and standard deviation σ of the primary particle diameter as a function of z. The values of D_p vs. z are plotted in Figure 3.13. These values of D_p compare favorably with the sizes observed with the SEM observations on the soot samples collected with the bulk specimen carrier. The maximum size shown in Figure 3.13 occurs at z=40 mm which coincides with the axial position of the maximum local soot volume fraction found by optical tests (see curve labeled "NS annulus" of Figure 7a in ref. 85). We consider this level to mark the lower boundary of the oxidation region.

The evolution of the primary particle size distribution with height for particles transported on the annular region can be characterized by the ratio σ/D_p. From our measurements we obtain that σ/D_p = 0.22, 0.18, 0.15 and 0.13 corresponding to heights z=10, 20, 30 and 40 mm respectively. The above values show that the primary particle size distribution narrows considerably with height above the burner mouth. This behavior clearly illustrates the dominant effect of surface growth reactions on soot morphology at low and intermediate heights of the flame.

As we see from Figure 3.13, there are no data points at heights below z=10 mm. This region of the flame was probed at a height z=5 mm. The soot sample collected at this height showed an aggregated stage, and a maximum primary particle size almost identical to that at z=10 mm. However

the radial positions at which D_p achieved a maximum (thermophoretically determined r_c) showed no reproducibility, thus indicating that the lower portions of the flame cannot be sampled consistently using the thermophoretic method.

Figure 3.13 provides information on the specific surface growth rate f(t) of the soot particles corresponding to $r=r_c$. The specific growth rate is defined as the mass deposition rate per unit of particulate surface area, and it is generally a function of the axial location z. The dependence on z translates to a dependence on the residence time t of the particles through a series of particle trajectory measurements reported by Santoro et al.[86] for the identical flame. The specific surface growth rate is related with the material density ρ_p and the t-gradient of the primary particle diameter through

$$f = \frac{\rho_p}{2} \frac{dD_p}{dt} \tag{3.8}$$

This equation was derived assuming a monodisperse primary particle size distribution function at each height z. This assumption was validated from an extensive evaluation of the electron micrographs which showed that the primary particle size is almost uniform for each aggregate corresponding to a specific location of the flame. If v_z the axial component of the flow velocity inside the flame at the annular region then

$$\frac{d}{dt} = v_z \frac{d}{dz} \tag{3.9}$$

Then Eq. (3.8) takes the form

$$f = \frac{\rho_p v_z}{2} \frac{dD_p}{dz} \tag{3.10}$$

The axial velocity profiles as a function of z and r are taken from ref. 86. The values of $D_p(z)$ are displayed in Figure 3.13 for the particles corresponding to the annular region. In order to calculate dD_p/dz we used a second order polynomial fit of the values of $D_p(z)$ which was subsequently differentiated algebraically. Using Eq. (3.10) we calculated the values of f as a function of z for the particles in the annular region. The z-dependence was converted to t-dependence through the particle residence time profiles calculated by Santoro[81] for the identical flame.

A soot density of 1.86 gr/cm^3 was assumed in Eq. (3.10). Thus we retrieve the values of f that are given in the following table

TABLE 3.1

Selected Data for the Ethene Diffusion Flame.

z (mm)	r_c [a] (mm)	v_z [b] (cm/s)	res. time t [c] (sec)	f (gr/cm^{2}s)
5	5.10	45	0.020	-
10	4.50	67	0.028	9.4×10^{-5}
15	4.00	90	0.034	10.5×10^{-5}
20	3.60	110	0.039	10.1×10^{-5}
30	3.10	140	0.047	6.2×10^{-5}
35	-	152	0.050	3.1×10^{-5}
40	2.70	165	0.054	-
50	2.40	-	0.059	-

[a] From refs. 85, 86
[b] From ref. 86
[c] From ref. 81

The calculations performed above demonstrate the potential of the thermophoretic method to give a quantitative description of the surface growth rate of soot inside a flame. No assumptions were adopted about the size distribution of the soot aggregates or the regime these particles belong to. The above data for the values of f(t) are used later on as an input to a theoretical model, in order to interpret the information derived by both the thermophoretic and optical methods about the soot field in the ethene diffusion flame.

Some comparisons are now made of the specific surface growth rates of soot calculated in our diffusion flame with those reported recently, concerning the soot growth rates in various flame environments. Our studies resulted in a maximum value of $f=10.5\times10^{-5}$ gr/cm^{2}s corresponding to an axial location z=15 mm above the burner mouth (t=0.034 sec). Harris and Weiner[38,39] reported a maximum value of $f=8\times10^{-5}$ gr/cm^{2}s for a series of rich premixed ethylene-air, flat flames. This value was calculated by them using purely optical observations of the soot partice field, adopting Rayleigh scattering theory and assuming a self-preserving size distribution of smooth spheres. Some uncertainty related to the choice of the refractive index of soot was estimated to be rather unimportant. Miller et al.[70] reported a similar value for a methane-air diffusion flame on a slot burner. The relatively higher value calculated for our system is compatible with the fact that methane has a lower sooting tendency than ethene under similar conditions.

Surface growth of soot particles in premixed flames has been attributed to various species. Prado and Lahaye[77] suggested that polyacetylenes or polyaromatic compounds are the principal growth species. Homann and Wagner[47] concluded that only the largest polyacetylenes are most likely the growth compounds. More recently Harris and Weiner[38,39] presented evidence that acetylene is the principal growth species in premixed ethylene flames, and reported first order surface growth rate constants. Even though the surface growth mechanism has been thoroughly investigated in premixed flames[2,4,6,7,41,43,98] there is too little known about the same mechanism in a diffusion flame environment. However it is known[68,70,90] that acetylene is a major intermediate species in a diffusion flame. In a recent study of the

acetylene production rates in a methane/air diffusion flame Miller et al.[70] reported a significant loss mechanism for C_2H_2 in regions where soot particles are detected in high concentrations. These observations suggest[89] that acetylene may be the soot growth species in a diffusion flame environment. Under this assumption the surface growth rate can be expressed as

$$f = K\left[C_2H_2\right]^j \tag{3.11}$$

where K is the rate constant for the surface reaction that converts C_2H_2 into soot, $[C_2H_2]$ the mole fraction of acetylene and j the reaction order. Unfortunately our data for f start from an axial location of z=10 mm while the mass spectrometric measurements reported by Miller[68] include acetylene concentration profiles up to z=9 mm. It is not possible therefore to estimate the reaction order from a lnf vs. $\ln[C_2H_2]$ plot for our diffusion flame. If we further assume first order surface growth reaction kinetics, as supported by previous studies[41,94], we obtain

$$f = K\left[C_2H_2\right] \tag{3.12}$$

We should stress that the surface growth process in diffusion flames may be fundamentally different from that in premixed flames. Some recent studies[70] however showed no proof of such a difference. Using the mass spectrometric measurements by Miller[68] for our diffusion flame system, we have $[C_2H_2]\approx 0.022$ corresponding to r_c at a height z=9 mm. Using the corresponding value for f at z= 10 mm from Table 3.1 we can calculate from Eq. (3.12) the surface growth reaction constant $K\approx 4\times10^{-3}$ gr/cm^{2}s atm

corresponding to the annular region at a height of z=9 mm above the burner mouth where T≈1700K. These values compare favorably with Harris and Weiner's estimates for "young soot" in a premixed ethene flame.[41]

The radial dependence of the soot morphological characteristics can be investigated using the various modified versions of the bulk specimen carrier. Examination of soot samples collected at three heights (z=10 mm, z=15 mm and z=30 mm) using three different probes showed that the thermophoretically determined values of r_c (radial position of maximum soot concentration) were consistently lower than those detected by the optical technique. The descrepancy in the value of r_c was higher down low (z=10 mm), while it was substantially reduced higher in the flame (z=30 mm). The radial positions, up to which particles were detected at a specified height, were also lower than expected from the optical measurements. These observations lead us to the conclusion that the three dimensional character of the flow field around the probe critically invalidates the position correspondence between the original radial position of the particles and the position at which they are ultimately captured on the probe. However our observations indicate that the radial dependence of the morphology of the soot particles maintains its original character for heights z>10 mm even though the steep concentration gradients are obviously obliterated by the insertion of the thermophoretic probe. For axial locations z<10 mm the flow field of the combustion gases was probably highly disturbed by the insersion of the thermophoretic probe. This disturbance, combined with the sensitive chemical character of the flame at these heights, created a low reproducibility of the thermophoretically determined values of r_c in the lowest portion of the flame. This discussion indicates that radial changes of the soot morphology detected by the

thermophoretic method show trends corresponding to the actual ones in the soot aerosol for heights z>10 mm. We must emphasize though that the "particle profile shift" discussed above should not affect the size of the primary particles and its dependence on both radial and axial coordinates.

At all three heights sampled with the modified probes we found that the primary particle size as well as the degree of agglomeration peak at $r=r_c$ (its corresponding lower value). This is demonstrated by Figure 3.14 showing particles collected from an axial location of z=30 mm and at three different radial positions. The probe used was the type I probe. An interesting observation can be made related to the particles collected from the fuel side of the annular region ($r<r_c$). As Figure 3.14 shows there is a difference in the nature of the particles corresponding to $r<r_c$ from those corresponding to $r\geqslant r_c$. The particles at $r<r_c$ possess a transparent or less dense appearance which may be associated with a liquid phase. A tentative explanation that these particles are associated with the onset of oxidation of the carbon substrate is not reasonable, since the oxidation should start from larger radial positions where the temperatures are higher and the concentrations of oxidative species (oxygen etc.) considerably larger. It is clear from Figure 3.14B and C that oxidation of the carbon substrate at positions $r\geqslant r_c$ does not take place. The particles corresponding to $r<r_c$were stable under the electron beam when captured on a carbon substrate. However when captured with the edge probe (type III) some motion was observed when the particles were irradiated by the beam. Figure 3.15 shows soot particles collected from three different radial positions using the edge probe at a height z=10 mm. The particles on the fuel side of $r_c(r<r_c)$ were further coated by a liquid phase deposit as displayed

by Figure 3.15A. The above deposit can be associated with condensation processes of various species that exist in the flame environment. This condensation may be a result of the cooling of these species induced locally by the cold probe during the sampling procedure. The particles on $r=r_c$ (Figure 3.15B) display a slightly larger primary size but no sign of the liquid deposit is apparent. Figure 3.16 shows particles collected from the fuel side of r_c with the type IV probe from a height of z=30 mm. It is evident from Figure 3.16A that the particles collected on the edge of the probe were further coated by a liquid phase deposit which is not as dense as in Figure 3.15A (z=10mm). The primary particle size shown in Figure 3.16A compares favorably with that of the neighboring particles shown in Figure 3.16B, which were collected on the grid supported carbon substrate of the probe.

As Figure 3.14A shows, the particles inside the annular region ($r<r_c$) are of smaller primary size and display a smaller degree of agglomeration compared with the particles of the annular region ($r=r_c$). However, some clusters of larger primary particle size were present, probably collected from the annular region as suggested by their morphology (compare Figures 3.14A and 3.14B). This fact does not allow for definite conclusions on the morphological characteristics of the particles at $r<r_c$.

Another important observation refers to the particles outside of the annular region ($r>r_c$). For these particles the primary size and the state of agglomeration decreases drastically with increasing radius. This is demonstrated by Figure 3.17 showing particles collected from an axial location z=30 mm at three different radial positions ($r\geqslant r_c$) using the type IV probe. This observation was consistent with all probes and all sampled heights (see Figures

3.15 and 3.18 corresponding to z=10 and z=15 mm respectively) as well as with our previous SEM observations using the original bulk specimen carrier as the thermophoretic probe.

Statistical analysis of the morphological data of soot collected from the annular region performed by the SMI Micro-comp data acquisition system yielded the mean primary particle diameter D_p at the sampled heights. These values are shown in Figure 3.13 and are in very good agreement with the mean sizes found by using the grids.

A detailed comparison of the particle sizes found through the thermophoretic method with those of the optical method[85] requires quantitative data on the aggregate morphology. Basic definitions of various terms used in carbon black image analysis are discussed in ref. 1. Various methods[46,63] have been developed in order to analyze the aggregate size and shape of carbon black particles by electron microscopy. The agreement between these methods has not always been satisfactory. Medalia's formulation on the morphology of aggregates[61-63,65] was adopted in our present work in order to acquire quantitative morphological data on the soot samples collected using the thermophoretic technique. If D_p is the primary particle diameter then the projected area and the volume of a primary particle are given by

$$A_p = \frac{\pi D_p^2}{4} \tag{3.13a}$$

$$V_p = \frac{\pi D_p^3}{6} \tag{3.13b}$$

According to Medalia's computer simulated random floc studies, an aggregate of projected area A consists of N_p primary particles given by

$$N_p = \left(A/A_p\right)^{1.15} \tag{3.14}$$

This formula was found to be accurate enough for $2 \leq N_p \leq 136$. The equivalent volume of the aggregate is then given by

$$V_a = N_p \, V_p \tag{3.15}$$

Considering the equivalent sphere of diameter D_a and volume V_a we obtain

$$D_a = D_p \, N_p^{1/3} \tag{3.16}$$

A series of micrographs of particles collected from a height of z=15 mm was analyzed in order to obtain data on the size distribution of the soot aggregates. The type I probe was used to thermophoretically capture the particles. Two sets of micrographs corresponding to two different radial positions ($r \approx r_c$ and $r > r_c$) were prepared for the image analysis. Each set consisted of about 10 photographic prints with approximately 90 numbered aggregates. Generally each particle that appeared continuous was treated as a single aggregate. However the low areal coverage of the prints reduced substantially the problems from overlapping. Aggregates that were cut off by the border of the prints were not measured. Each one of the particles was individually traced using the light pen of a Dapple Image Analysis system in order to compute its projected area A. The previously measured D_p was used to calculate A_p from Eq. (3.13a) and then N_p from Eq. (3.14). Finally Eqs. (3.15) and (3.16) were used to calculate the volume of the aggregate and the equivalent sphere diameter. Two typical micrographs, one corresponding

to the annular region and the other to the outside region of r_c are reproduced in Figure 3.19A and 3.19B respectively. The primary particle diameters were found to be D_p = 22.1 nm at r = 3.05 mm = r_c and D_p = 11.8 nm at r = 3.73 mm. Figure 3.19C shows a typical micrograph of soot particles while Figure 3.19D is the equivalent digitized picture created by the Dapple system on a video image display.

In addition to the parameters described so far some other quantities were also calculated; the perimeter p of each aggregate, a shape factor defined by $f_s = 4\pi A/p^2$ showing the proximity of the projection of the aggregate to the circular geometry (f_s = 1 for a circle), and the maximum length of the aggregate passing through the center of mass of the projected area of the particle. A test of the reliability of the tracing method was performed using two different operators to analyze a selection of a few aggregates. For intermediate and large size aggregates the measurements for the projected area A were well within 10% of each other. For the smallest particles (~5% of the total number of particles measured) the values of A differed up to 50%. These differences are attributed to the poor definition of the smallest particles but are expected to contribute insignificantly to the evaluation of the generalized moment ratios of the PSDF. Generally the linear quantitites measured by the two operators compared very favorably, while area measurements were within the experimental error requirements.

The procedure described above provides the distribution of the equivalent sphere diameters D_a. In the following discussion the notation D_i is used to denote the values assumed by the equivalent sphere diameter D_a of the soot aggregates. For a general discrete distribution with k size classes and

n_i particles per class, the geometric mean diameter D_g can be calculated by

$$\ln D_g = \frac{\sum_{i=1}^{k} n_i \ln D_i}{\sum_{i=1}^{k} n_i} \tag{3.17}$$

and the mean standard deviation σ_g by

$$\sigma_g^2 = \frac{\sum_{i=1}^{k} n_i \left[\ln \frac{D_i}{D_g}\right]^2}{\sum_{i=1}^{k} n_i} \tag{3.18}$$

For the data obtained through the image analysis system n_i=1. So Eqs. (3.17) and (3.18) simplify to

$$\ln D_g = \frac{1}{k} \sum_{i=1}^{k} \ln D_i \tag{3.19a}$$

$$\sigma_g^2 = \frac{1}{k} \sum_{i=1}^{k} \left[\ln \frac{D_i}{D_g}\right]^2 \tag{3.19b}$$

where k now is the number of particles measured.

Using the same formulation, the generalized moment ratios D_{30} and D_{63} can be calculated using the following relations

$$D_{30}^{3} = \frac{1}{k} \sum_{i=1}^{k} D_i^{3} \tag{3.20a}$$

$$D_{63}^{3} = \frac{\sum_{i=1}^{k} D_i^{6}}{\sum_{i=1}^{k} D_i^{3}} \tag{3.20b}$$

These two equations provide the tool for comparisons between the soot morphological data obtained using the thermophoretic method and the data acquired through the optical studies. Using the quantitative image analysis results we can construct the following table

TABLE 3.2

Radial Dependence of Soot Morphological Data for the Ethene Diffusion Flame

	z = 15 mm					
	D_g(nm) (3.19a)	σ_g (3.19b)	D_{30}(nm) (3.20a)	D_{63}(nm) (3.20b)	f_s	N_p
r=3.05 mm ≈ r_c	60.3	0.40	72	88.3	0.52	34
r=3.73 mm	32.4	0.37	38	47.3	0.63	34

Santoro et al.[86] using Mie theory, calculated a value D_{63}≈110 nm corresponding to particles of the annular region (r=4.0 mm ≈ r_c) at a height

z=15 mm. The use of Rayleight theory produced[85] a value of D_{63}=78 nm. These values are in fair agreement with that calculated through the thermophoretic technique. As discussed previously the radial position of the annular region detected by the optical method is consistently higher than that determined by the thermophoretic technique. The calculation of D_{63} from the optical method required an assumption for the value of the complex refractive index of the soot particles. The assumed value of $\tilde{m}$=1.57 - 0.56i proved to be very reasonable. The number concentration of the soot aerosol can be derived from the optical data using an approximation of the value assumed by the ratio $f_N=(D_{63}/D_{30})^3$. Santoro et al.[85] adopted the value corresponding to a self-preserving form of the distribution function which is equal to 2.00. As we see from our measurements f_N has a value of 1.84 and 1.93 at the two radial positions analyzed.

Dobbins and Mulholland[23] modeled the soot aerosol using the assumption that all the gas to particle conversion is due to particle inception, and particle growth occurs only by coagulation. Under these assumptions the replenishment of incipient particles coexisting with coagulative growth results in a wide distribution function and very high values of f_N. This formulation, which is not inconsistent with the optical observations, is clearly shown to be incorrect by the recent morphological data obtained using the thermophoretic sampling technique. The dominant role of surface growth has the opposing effect or the variation of f_N. Our observations as well as the numerical simulations (see Chapter 4) show that surface growth causes a reduction of the width of the distribution function and lower values of the ratio f_N. In fact this quantity throughout the low portions of the flame is not greatly different from the asymptotic value that was chosen by Santoro et

al.[85] and others in reducing the optical data. The applicability of this value, which is fortuitous because the assumptions for its validity are clearly not fulfilled, now appears to be a plausible assumption on which to reduce the optical data.

The mean values of the shape factor f_s, calculated at the two positions analyzed, show that the particles are closer to a spherical shape away from the annular region. This observation is compatible with our previous comment on the radial dependence of the degree of agglomeration of the soot particles at a specified axial location. Two more points of interest are; the constant value of N_p (number of primary particles per aggregate) with radial position and the relatively high values of the mean standard deviation $\sigma_g \approx 0.4$ at both locations.

Some comparisons of the actual equivalent sphere diameter distributions are now being made with the equivalent log-normal distributions, defined as those giving the same values of D_{30} and D_{63} with these calculated in Table 3.2. For these distributions $D_g = 65$nm, $\sigma_g = 0.26$ at r_c; $D_g = 34$nm, $\sigma_g = 0.27$ at $r > r_c$. Figure 3.20 shows a comparison of the actual with the equivalent log-normal distributions at both radial positions analyzed. Generally the descrepancies are higher at the extreme values of the diameter range. However the differences at small diameters is not expected to affect the resulting values of D_{30} and D_{63}. On the contrary slight differences at large diameters would result in a substantial change of the values of D_{30} and D_{63}.

A computer experiment was performed in order to check the statistical reliability of the distributions calculated previously. Ninety

diameters were randomly generated in the equivalent sphere diameter range defined by D_{min} and D_{max}. These are the extreme values obtained by the thermophoretic method for particles corresponding to r_c at z=15 mm. The ninety diameters were used to calculate the corresponding probability function values P(D). The equivalent log-normal probability function P was used, described by D_g=65 nm and σ_g=0.26. Nine size classes were defined in order to obtain the discrete distribution of the computer generated sample. The histogram of the distribution obtained is compared to the actual log-normal form (Figure 3.21A) corresponding to the distribution of a very large sample of diameters. We can clearly see that even though the diameters were distributed according to the log-normal form, the distribution obtained is very different. Another experiment was performed using a sample of 500 randomly generated diameters. In this case the distribution obtained is much closer to the log-normal form (Figure 3.21B), thus demonstrating the need of the morphological analysis of about 500 particles at each position in order to obtain statistically reliable values of the quantities measured. The above discussion illustrates the relatively low statistical reliability of the soot morphological data obtained so far. However even if the quantities calculated were not measured accurately, we expect the trends to be right and the comparisons with the optical data fairly reasonable. A more detailed comparison of the data obtained by both methods is needed, in order to evaluate the soot particle morphological characteristics in the ethene diffusion flame. However this comparison requires extensive work which is not pursued at the present time.

3.6 A hypothetical description of the physical aspects of soot formation and transport in the laminar axisymmetric ethene diffusion flame.

The data acquired through the optical and thermophoretic methods provide extensive information on the soot field inside the laminar ethene diffusion flame under investigation. These observations are now combined and evaluated in order to interpret the mechanisms of soot formation and transport in the lower and intermediate heights of the flame.

During the discussion about the appearance of the ethene flame, we mentioned that the luminous yellow regions are surrounded on the air side by a thin blue hue which locates the main reaction zone. This zone, which is visible low in the flame but becomes indistinct higher up, contains the surface of maximum temperature that is named "flame sheet". The reaction zone also coincides[72,90] with the location of maximum concentration of the combustion products (CO_2, H_2O etc.). The fuel side of the flame sheet defines the fuel rich region, while the air side is known as the fuel lean region. Figure 3.22 shows the reaction zone surrounding the flame regions where soot particles are detected. The locus of maximum soot volume fraction ϕ_{max} (annular region) is also shown, corresponding to radial positions on the fuel rich side of the flame sheet. Particle paths as calculated by Santoro et al.[86] are displayed throughout the flame. In the upper portion of the flame (z>20 mm), the line of ϕ_{max} corresponds to a particle path which probably is nearly coincident with the streamlines of the flow field. It is apparent from Figure 3.22 that the particle trajectories penetrate the soot annulus ($r=r_c$) at axial locations z lower than 15 mm. From that height the particles are convected upwards following trajectories parallel to r_c. This behavior of the particle trajectories is due to the strong entrainment of air and the high temperature

gradients in the lower portions of the flame, and has not been thoroughly investigated so far in connection with the particle formation processes.

Almost a quarter of a century ago, Wolfhard and Parker[100,101] examined spectroscopically various diffusion flames on the slot burner, which now has their name. They found that in the ethylene and methane/air diffusion flames they examined, the sooting zone occurs some millimeters to the fuel rich side of the reaction zone. Haynes and Wagner[44], and Santoro et al.[85] in recent studies of laminar ethylene/air diffusion flames observed that the particle number concentration increases toward the reaction zone. The number concentration subsequently decreases toward the fuel zone while the particle size increases, and the soot volume fraction achieves a maximum on $r=r_c$ (Figure 3.22). However, Santoro et al.[85] found that the number concentration goes through a minimum and then increases towards smaller radial positions (see N profile in Figure 3.22). This behavior of N cannot be attributed to the use of Rayleigh theory for the reduction of the optical data in ref. 85, since the particle sizes low in the flame are clearly in the Rayleigh limit.

The high number concentration of particles close to the reaction zone occurs under a negligible soot loading (low ϕ). This can only happen when the particles are very small ($d<2nm$) which suggests that the particles are formed locally in large numbers on the fuel rich side of the reaction zone. The radical and ion concentrations are highest close to the position where the temperature maximum occurs. These species have been associated with the particle inception mechanisms and are considered[55] to be potential soot precursors. Additionally at the lowest portions of the flame where the

particle trajectories intersect the soot annulus, there exists a maximum of the Q_{vv} signal[82] occuring at $r=r_c$. If we accept that the particles are formed outside r_c close to the reaction zone, then these particles are transported into the cooler, more fuel rich interior of the flame by the strong convective as well as thermophoretic forces. During this transport surface growth becomes important since the temperature and radical/ion concentrations become too low to create more particles. This period is also associated with intense coagulation because of the high particle concentrations. This mechanism may account for the minimum of the number concentration at the radial position where ϕ displays a maximum. The maximum of the value of ϕ is caused by the surface growth mechanisms which become more intense as the particles move from the zone of their formation towards the interior of the flame. These regions contain various species as acetylene[68] and other unsaturated as well as polyaromatic hydrocarbons[90], which are considered to be the major growth compounds. Mass spectrometric measurements on an identical flame performed by Miller[68], showed that the acetylene production rate peaks at $r=r_c$ implying that the surface growth mechanisms at these locations are very intense. The above locations are also characterized by lower temperatures and display visible fluorescence during the optical tests. According to Tesner[93], surface growth can continue to increase the soot loading (ϕ) at temperatures much below those required for particle inception. The transport of the particles into regions of even lower temperatures, associated with a decline of the reactivity of the gases, causes a steady decline of the surface growth rate. The particles also lose their reactivity[38] by various mechanisms which are not well established at this point.

The above discussion suggests that the first particles, called incipient

particles, are formed on the fuel rich side of the reaction zone in a region where the temperature is a few hundred degrees lower than that on the flame sheet. The Q_{vv} profile-changes quoted by Santoro and Miller[82] at the lower portion of the flame indicate that the characteristic time for the particle inception processes is of the order of 1 ms. According to Harris et al.[42], who studied a premixed flat ethylene/argon/oxygen flame, the particle inception process lasts for about 2-3 ms in that flame. It is generally believed that this time scale characterizes the soot particle inception mechanism in a flame environment.

The following discussion gives a tentative explanation of the variation of the primary particle size of the aggregates along the radial coordinate at a specific axial location z. This theory is consistent with the previously presented mechanism of soot particle inception in the lower portions of the ethylene/air diffusion flame under investigation.

Particles on the fuel side of r_c were found to have a smaller primary size than those of r_c, at all heights examined using the thermophoretic method (see Figure 3.14). These particles were created low in the flame (z<4 mm) where surface growth is not a significant factor. At these heights the Q_{vv} signal was very weak. According to Santoro and Miller[82] the first axial location displaying the familiar Q_{vv} annular structure was found to be at z=4 mm. The particles created below this height were transported to the interior of the flame by the combustion gases (see Figure 3.22). These regions ($r<r_c$) are also associated with lower surface growth rates as mentioned previously. The above mechanism explains the smaller primary particle size at $r<r_c$ compared to that at $r=r_c$ at all heights. This model can also account for the higher

number concentration on the fuel side of the annular region $r<r_c$ (see N profile in Figure 3.22). This point is discussed in chapter 4, where a bimodal integral solution of the aerosol dynamic equation is presented, and subsequently used to model the soot aerosol processes in the ethene diffusion flame.

Particles present on the annular region at lower axial locations of the flame ($4<z<10$ mm) were formed outside r_c at even lower heights. During their transport toward r_c, these particles grow through gas phase surface reactions. The particles on $r=r_c$ at $z=10$ mm travel in a richer[68] growth species environment and are relatively younger than those existing on the annular region at $z=5$ mm. The competition between the two factors could account for the observation of the thermophoretic method that the maximum primary particle size is almost constant in that height interval. From that point and on ($z>15$ mm), the particles are convected upwards along path lines that do not intersect the soot annulus. During this transport they further grow through agglomeration and surface growth reactions until they enter the upper part of the flame ($z=40$ mm) where oxidation mechanisms dominate.

Particles on the air side of r_c have been formed outside r_c lower in the flame. They were subsequently convected upward thus never having traveled through the region of maximum concentration of the growth species. The primary particle size is therefore smaller than that of the particles at r_c. Another possible explanation for the smaller size as well as the lower degree of agglomeration of these particles is the presence of oxidative species in ample concentrations in a high temperature environment. These species (mainly O_2) diffuse into the interior of the flame thus attacking the various particles and compounds in an environment which promotes the oxidation

mechanisms.

The existence of smaller particles on the air side of r_c, which was consistent at all heights using the thermophoretic technique (see Figures 3.14, 3.15, 3.17 and 3.18), is also in agreement with the optical observations. As shown previously in Table 2.2 for a height z=30 mm, the depolarization ratio ρ_v drops by a factor of 3 from r_c to $r>r_c$. According to the definition of ρ_v this suggests that the scatterers (soot particles) exhibit less material and/or geometrical anisotropy toward the air side of r_c.

The above discussion attempts to combine the information provided by both methods for the ethene/air diffusion flame, in order to describe the physical aspects of soot formation and transport in that flame. However there are still steps that are not well established (i.e. number concentration anomaly at low heights), and more studies are required in order to gain a complete understanding of the physical processes associated with the soot formation mechanisms in diffusion flames.

CHAPTER 4

THEORETICAL

4.1 A bimodal integral solution of the aerosol dynamic equation

The wide range of data related to the soot aerosol acquired through the optical and the thermophoretic methods was extensively evaluated in the previous chapter. In this chapter a mathematical model examining the aerosol dynamics is discussed when particle formation, coagulation and surface growth are present. The term coagulation is used to describe the process during which two spherical particles collide and form another spherical particle. This mechanism is used as a first approximation of the agglomeration processes inside the soot aerosol. The model accounts for a time varying bimodal representation of the aerosol particle size distribution function and provides a theoretical framework for the interpretation of the experimental data. The bimodal solution is an approximate solution since it forces the size distribution function to be of a prescribed form (logarithmic normal). However the properties of this distribution are time dependent thus accounting for the evolution of the aerosol particle sizes. Upon completion of the model the effects of the various parameters on the development of the distribution function are investigated. Some conclusions about the soot aerosol are drawn contributing toward a better understanding of the mechanisms leading to the formation and growth of soot in diffusion flame systems. The model can be used to study the physical processes acting upon the particulate phase in various aerosol systems in which intense particle generation mechanisms are present.

The model is developed from the general aerosol dynamic equation by an integral formulation that includes the above physical/chemical mechanisms. Other models currently used to study the aerosol behavior are briefly discussed and extensively compared to this model. These comparisons show that the model provides a tool which could predict the effects of various parameters on the behavior of an aerosol, to assist the interpretation of experimental investigations. The development of the present model is discussed below in detail.

4.1.1 Description of the model

The time varying particle volume distribution function (PVDF) is the main quantity to characterize the growth of soot particles. A very common assumption in the past has been that the particles are of uniform size (monodisperse). However the existence of agglomeration strongly argues against this assumption and assures its invalidity. Another assumption has been the self preserving form[31] of the PVDF in the case of an aerosol undergoing coagulation by Brownian motion in the free molecular regime. This self-preserving form of the distribution function (SPDF) was studied extensively by Lai et al.,[57] Graham and Homer[36], and Graham and Robinson[37]. These studies concluded that the SPDF is an asymptotic solution of the coagulation equation that is independent of the initial distribution of a time evolving aerosol. A necessary condition though for the validity of the self-preserving form is the constancy of the particle volume fraction ϕ as discussed by Lai et al[57]. This condition is violated when particle formation or surface growth are present as in the case of the soot aerosol in diffusion flames.

Numerous studies of samples of soot aggregates collected from various flames showed the particle volume distribution function to be approximately logarithmic normal or Gaussian (corresponding to a log-normal distribution with low standard deviation):

Wersborg et al.[98] studying a flat acetylene-oxygen low pressure flame concluded that the PVDF is nearly Gaussian as long as most of the particles are spherical and it becomes log-normal when chain formation becomes predominant.

In the pyrolytic decomposition of benzene diluted in nitrogen at temperatures around 1400K and atmospheric pressure, Lahaye et al.[56] reported that for small particles (soot formation stage) the PVDF is Gaussian, while for large particles a log-normal distribution is observed.

Chippett and Gray[12] studying soot aggregates extracted from atmospheric pressure acetylene-air premixed flames have shown the sizes to be distributed according to the logarithmic-normal law.

Bockhorn et al.[5] (1981) came to the same conclusion for the PVDF for particles collected from atmospheric pressure propane-oxygen premixed flames and propane-oxygen flames to which hydrogen or ammonia were added.

Bochkorn et al.[3] (1986) found the log-normal form to describe better the PVDF derived from EM studies of soot, collected from

premixed hydrocarbon-oxygen low pressure flat flames using various hydrocarbons (C_3H_8, C_2H_2, C_6H_6).

The above observations under various experimental environments led to the wide use of the log-normal form as the best approximation to the PVDF.[58-60,99]

A continuous size distribution n(v,t) of an aerosol undergoing interparticle collisions in the presence of particle inception (formation) is governed by the following nonlinear integro-differential equation

$$\frac{\partial}{\partial t} n(v,t) = -n(v,t) \int_0^\infty K(v,u)\, n(u,t)\, du + \frac{1}{2} \int_0^v K(u,v-u)\, n(u,t)\, n(v-u,t)\, du + S(v,t) \qquad (4.1)$$

where n(v,t)dv is the number of particles in the particle volume range v to v+dv per unit volume. The first integral in the above equation represents the loss of particles from that volume range because of collisions with particles of any volume. The second integral represents the gain of particles in the specified volume interval as a result of collisions between smaller particles. The source term S(v,t) accounts for the particle formation mechanisms and specifies the number of particles created in that size range per unit volume and time. The collision frequency factor K(v,u) represents the number of collisions of particles of volume v with particles of volume u per unit concentration of each size and its form depends on the size of the particles.

The particle volume probability function (PVPF) is then defined by

$$P(v,t)\,dv = \frac{n(v,t)}{N}\,dv$$

where N is the number of particles of all sizes per unit volume of the aerosol. It is obvious that $\int_0^\infty P(v,t)\,dv = 1$.

The kth moment of n(v,t) is defined by

$$M_k(t) = \int_0^\infty v^k\, n(v,t)\,dv = N \int_0^\infty v^k\, P(v,t)dv \qquad (4.2)$$

Multiplying Eq. (4.1) by v^k and integrating over all sizes

$$\frac{dM_k}{dt} = \frac{1}{2}\int_0^\infty \int_0^\infty f(u,v,k)\, K(v,u)\, n(v,t)\, n(u,t)\, dvdu + \int_0^\infty S(v,t)v^k\, dv \qquad (4.3)$$

$$\text{where } f(u,v,k) = \begin{cases} -1\ ; & k = 0 \\ 0\ ; & k = 1 \\ 2uv\ ; & k = 2 \end{cases}$$

From Eq. (4.2) we derive that M_o=N, and $M_1 = \phi$ the particle volume fraction (total volume of particles per unit volume of system). Another variable of interest

is the dimensionless second moment defined as

$$f_N = \frac{NM_2}{\phi^2}$$

The quantities defined above have a physical interpretation related to the optical properties of small absorbing particles in the Rayleigh regime. The extinction coefficient is proportional to ϕ (see Eq. 2.4) while the volumetric scattering cross section is proportional to M_2 (see Eq. 2.1). As shown from the definition of f_N, this quantity is used to arrive at the value of N from the combined measurements of extinction and scattering.

A general analytic solution for the first three moments with an arbitrary initial condition, does not exist due to complexities involved in the integro-differential form of the corresponding equations and the particle size dependency of the collision frequency K(v,u). Simplifications imposed on the form of K(v,u) can lead to analytic solutions. However in the case of coagulation due to Brownian motion in the free molecular regime (particles much smaller than the mean free path of the molecules of the host gas) the complicated expression for K(v,u) imposes the search for numerical solutions. In this case

$$K(v,u) = K_{fm}\, g(u,v) \tag{4.4}$$

where $K_{fm} = \left[\frac{3}{4\pi}\right]^{1/6} \left[\frac{6KT}{\rho_p}\right]^{1/2}$

and $$g(u,v) = \left[u^{1/3} + v^{1/3}\right]^2 \left[\frac{1}{u} + \frac{1}{v}\right]^{1/2}$$

It is $K = 1.38 \times 10^{-16}$ erg molec^{-1} K^{-1} (Boltzmann's constant)

ρ_p: particle density

T: Temperature of the aerosol

This weakly singular form of the collision frequency is integrable, thus introducing no irregularities in the numerical integration of the integro-differential equation (4.3).

The above form of the collision frequency factor is derived in the kinetic theory of gases for collision among particles that behave as rigid elastic spheres. This assumption is reasonable for the soot aerosol at the early stage of soot formation where the particles may coalesce upon colliding. However at later stages the particles retain their structure and chainlike clusters are formed. These highly structured particles called agglomerates or aggregates further collide under an "agglomerate coagulation coefficient" generally different from the form given in Eq. (4.4). Some recent numerical simulation studies by Mulholland et al.[73] examine the form of this coefficient using a relatively small number of particles (~500). The law describing the Brownian motion of the particles is given by Langevin's equation and some fractal theory concepts are used in their analysis.

A strong particle formation term in the presence of coagulation would obviously result in a bimodal distribution that produces a double humped particle size distribution function[99]. The first peak is the particle

inception (formation) mode and its height is determined by the strength of the source term. Once particles of the particle inception mode collide with one another they create new particles forming the growth mode whose properties are time dependent. The overall PVDF can be decomposed as

$$n(v,t) = n_1(v,t) + n_2(v,t) = N_1 P_1(v,t) + N_2 P_2(v,t) \tag{4.5}$$

the two terms corresponding to the inception and growth mode respectively. Substituting Eq. (4.5) into (4.3) using (4.4)

$$\frac{dM_k}{dt} = K_{fm} \frac{N_1^2}{2} Z_{fm_1}^{(k)} + K_{fm} \frac{N_2^2}{2} Z_{fm_2}^{(k)} + K_{fm} N_1 N_2 Z_{fm_b}^{(k)} + \int_0^\infty S(v,t) v^k dv \tag{4.6}$$

where the collision integrals are defined by

$$Z_{fm_i}^{(k)} = \int_0^\infty \int_0^\infty f(u,v,k)\ g(u,v)\ P_i(v)\ P_i(u)\ dvdu \qquad (i = 1,2) \tag{4.7a}$$

$$Z_{fm_b}^{(k)} = \int_0^\infty \int_0^\infty f(u,v,k)\ g(u,v)\ P_1(v)\ P_2(u)\ dvdu \tag{4.7b}$$

Equation (4.7a) gives the collision integrals resulting from interparticle collisions between particles of the same mode (i = 1 for inception mode,

i = 2 for growth mode) while (4.7b) results from collisions between particles of different modes.

The source term is decomposed $S(v,t) = S_t(t)\ P_o(v)$

where $P_o(v)$ the time independent, source particle volume probability function and $S_t(t)$ gives the number of particles of all sizes created per unit volume and time. Then Eq. (4.6) becomes

$$\frac{dM_k}{dt} = \frac{K_{fm}}{2}\left[N_1^2 Z_{fm_1}^{(k)} + N_2^2 Z_{fm_2}^{(k)} + 2N_1N_2 Z_{fm_b}^{(k)}\right] + S_t(t)\int_0^\infty v^k P_o(v)dv \quad (4.8)$$

We now prescribe the form of the time dependent particle volume probabiltiy function (PVPF) to be log-normal for both modes

$$P_i(v,t) = \frac{1}{v}\frac{1}{\sqrt{2\pi}\ \sigma_{v_i}(t)} \exp\left[-\frac{1}{2}\left[\frac{\ln\ v/v_{gi}(t)}{\sigma_{v_i}(t)}\right]^2\right]; \quad (i = 1,2) \qquad (4.9)$$

where v_{g_i} the geometric mean particle volume and σ_{v_i} the mean standard deviation. Both v_{g_i} and σ_{v_i} are time dependent with dependencies we wish to determine. We further assume that the source PVPF $P_o(v)$ is log-normal, described by v_{g_o} and σ_{v_o} both constant.

For a log-normal distribution described by v_g, $\sigma_g = \sigma_v/3$ we can show that

$$M_k = N\, v_g^{\,k} \exp\left[\frac{9}{2}\sigma_g^{\,2} k^2\right] \qquad (4.10)$$

For a bimodal distribution

$$M_k(t) = \int_0^\infty v^k \left[n_1(v,t) + n_2(v,t) \right] dv = M_k^1(t) + M_k^2(t)$$

where the notation M_k^i is adopted to denote the kth moment of the PVDF corresponding to the ith mode $(i = 1, 2)$.

Using Eq. (4.10) for a bimodal distribution consisted of two log-normal modes we obtain

$$M_k(t) = N_1 v_{g_1}^k \exp\left[\frac{9}{2} \sigma_{g_1}^2 k^2\right] + N_2 v_{g_2}^k \exp\left[\frac{9}{2} \sigma_{g_2}^2 k^2\right] \tag{4.11}$$

Generally v_{g_i} and σ_{g_i} $(i = 1,2)$ are time dependent. The last equation gives the first three moments as

$$N = N_1 + N_2 \tag{4.12a}$$

$$\phi = \phi_1 + \phi_2 = N_1 v_{g_1} \exp\left[\frac{9}{2} \sigma_{g_1}^2\right] + N_2 v_{g_2} \exp\left[\frac{9}{2} \sigma_{g_2}^2\right] \tag{4.12b}$$

$$M_2 = M_2^1 + M_2^2 = N_1 v_{g_1}^2 \exp\left[18\sigma_{g_1}^2\right] + N_2 v_{g_2}^2 \exp\left[18\sigma_{g_2}^2\right] \tag{4.12c}$$

The quantities N_i, ϕ_i and M_2^i denote the first three moments of the PVDF corresponding to the ith mode $(i = 1,2)$. The assumption on the log-normal

behavior of $P_o(v)$ simplifies Eq. (4.8) with the use of Eq. (4.10)

$$\frac{dM_k}{dt} = \frac{K_{fm}}{2}\left[N_1^2 Z_{fm_1}^{(k)} + N_2^2 Z_{fm_2}^{(k)} + 2N_1N_2 Z_{fm_b}^{(k)}\right] +$$

$$S_t(t) v_{g_o}^k \exp\left[\frac{9}{2}\sigma_{g_o}^2 k^2\right] \tag{4.13}$$

For k = 0 we obtain the equation for the particle number concentration

$$\frac{dN}{dt} = \frac{K_{fm}}{2}\left[N_1^2 Z_{fm_1}^{(0)} + N_2^2 Z_{fm_2}^{(0)} + 2N_1N_2 Z_{fm_b}^{(0)}\right] + S_t(t) \tag{4.14}$$

The first three terms of the right hand side of the above equation describe the following collision mechanisms respectively

I)	● + ● —— O	● particles of mode 1
II)	O + O —— O	O particles of mode 2
III)	● + O —— O	

As we see mechanism II does not affect N_1 while mechanism III does not affect N_2. Mechanism I affects both N_1 and N_2 in opposite directions. N_1 is reduced by two units while N_2 increases by one unit during a single collision. A loss of one unit is accounted for by a term $K_{fm}/2\ N_1^2\ Z_{fm_1}^{(0)}$. Then a gain of one unit is represented by the term $-\ K_{fm}/2\ N_1^2\ Z_{fm_1}^{(0)}$. The source term in Eq. (4.14) affects only N_1. This reasoning leads to the

following equations for N_1 and N_2 using Eqs. (4.12a) and (4.14)

$$\frac{dN_1}{dt} = K_{fm} N_1 \left[N_1 Z_{fm_1}^{(0)} + N_2 Z_{fm_b}^{(0)} \right] + S_t(t) \tag{4.15a}$$

$$\frac{dN_2}{dt} = \frac{K_{fm}}{2} \left[N_2^2 Z_{fm_2}^{(0)} - N_1^2 Z_{fm_1}^{(0)} \right] \tag{4.15b}$$

Using Eq. (4.13) for k = 1 we obtain the equation for the particle volume fraction

$$\frac{d\phi}{dt} = S_t(t)\, v_{g_o} \exp\left[\frac{9}{2} \sigma_{g_o}^2 \right] \tag{4.16}$$

Applying Eq. (4.10) with k = 1 for the first mode and differentiating with respect to time

$$\frac{d\phi_1}{dt} = \frac{dN_1}{dt} v_{g_1} \exp\left[\frac{9}{2} \sigma_{g_1}^2 \right] \tag{4.17}$$

Equation (4.17) was derived assuming that the size distribution parameters v_{g_1} and σ_{g_1} of the first mode are constant with respect to time. This assumption seems reasonable as long as the particles are generated by a log-normal type source with time independent parameters v_{g_o} and σ_{g_o}. Obviously $v_{g_1} = v_{g_o}$ and $\sigma_{g_1} = \sigma_{g_o}$. Combining Eqs. (4.12b), (4.15a), (4.16) and (4.17) we obtain

$$\frac{d\phi_2}{dt} = -K_{fm} N_1 v_{g_1} \exp\left[\frac{9}{2} \sigma_{g_1}^2 \right] \left[N_1 Z_{fm_1}^{(0)} + N_2 Z_{fm_b}^{(0)} \right] \tag{4.18}$$

From Eq. (4.13) for k = 2 we obtain the equation for the second moment

$$\frac{dM_2}{dt} = \frac{K_{fm}}{2}\left[N_1^2 Z_{fm_1}^{(2)} + N_2^2 Z_{fm_2}^{(2)} + 2N_1N_2 Z_{fm_b}^{(2)}\right] + S_t(t)\, v_{g_o}^2 \exp\left[18\sigma_{g_o}^2\right] \quad (4.19)$$

Again applying Eq. (4.10) with k =2 for the first mode and differentiating with respect to time under the assumption $v_{g_1} = v_{g_o}$ and $\sigma_{g_1} = \sigma_{g_o}$

$$\frac{dM_2^1}{dt} = \frac{dN_1}{dt}\, v_{g_1}^2 \exp\left[18\,\sigma_{g_1}^2\right] \quad (4.20)$$

Combining Eqs. (4.12c), (4.15a), (4.19) and (4.20)

$$\frac{dM_2^2}{dt} = \frac{K_{fm}}{2}\left[N_1^2 Z_{fm_1}^{(2)} + N_2^2 Z_{fm_2}^{(2)} + 2N_1N_2 Z_{fm_b}^{(2)}\right] -$$

$$-K_{fm}N_1 v_{g_1}^2 \exp\left[18\,\sigma_{g_1}^2\right]\left[N_1 Z_{fm_1}^{(0)} + N_2 Z_{fm_b}^{(0)}\right] \quad (4.21)$$

Equations (4.15a), (4.15b), (4.18) and (4.21) form a closed system with the unknowns N_1, N_2, ϕ_2, M_2^2 at a specified t. The collision integrals for the first mode $Z_{fm_1}^{(k)}$ can be calculated explicitly using the known values of v_{g_1} and σ_{g_1}. The collision integrals for the second mode $Z_{fm_2}^{(k)}$ are complicated functions of v_{g_2} and σ_{g_2} which can be expressed as functions of the unknowns through the assumption of the log-normal behaviour of the growth mode (see Appendix A). The system of the above equations can be integrated numerically using any set of arbitrary initial conditions.

Initial attempts to integrate the system of equations for N_1, N_2, ϕ_2 and M_2^2 proved to be unsuccessful because of the wide range of the primary variables involved. Using CGS units a typical number concentration value is of the order of 10^{10} -10^{12} (cm^{-3}) while a typical value for M_2^2 can be as small as 10^{-20} to 10^{-25} (cm^3). The extremely wide range of the unknowns created some difficulties during the numerical integration. A dimensionless formulation proved to be the remedy to this problem. Introducing a new variable N_o, defined as the total number of particles created by the source mechanisms over all times per unit volume, we define

$$\phi_o = N_o v_{g_1} \exp\left[\frac{9}{2}\sigma_{g_1}^2\right]$$

$$M_2^o = N_o v_{g_1}^2 \exp\left[18\sigma_{g_1}^2\right]$$

The new dimensionless variables are now defined by

$$X_1 = \frac{N_1}{N_o} \tag{4.22a}$$

$$X_2 = \frac{N_2}{N_o} \tag{4.22b}$$

$$X_3 = \frac{\phi_2}{\phi_o} = \frac{N_2 v_{g_2} \exp\left[\frac{9}{2}\sigma_{g_2}^2\right]}{N_o v_{g_1} \exp\left[\frac{9}{2}\sigma_{g_1}^2\right]} \tag{4.22c}$$

$$X_4 = \frac{M_2^2}{M_2^o} = \frac{N_2 v_{g_2}^2 \exp\left[18\sigma_{g_2}^2\right]}{N_o v_{g_1}^2 \exp\left[18\sigma_{g_1}^2\right]} \tag{4.22d}$$

The dimensionless time is given by

$$t' = \frac{t}{\tau_s} \tag{4.22e}$$

where τ_s is defined below.

So far we did not make any assumption on the form of the time dependent source function $S_t(t)$. A Gaussian pulse is a first approximation to the particle formation rate by natural sources

$$S_t(t) = S_{max} \exp\left[-\left(\frac{t - t_m}{\tau_s}\right)^2\right] = S_{max}\, f_s(t) \tag{4.23}$$

where t_m is the time of maximum formation rate, and τ_s is the e^{-1} half width of the pulse. From the definition of the total number of particles created over all times per unit volume

$$N_o = \int_0^{t_e} S_t(t)\, dt \tag{4.24}$$

where t_e is the time of observation which can be in the time interval where $S_t(t)$ is still active. Using Eq. (4.23) in Eq. (4.24), we find

$$\frac{S_{max}\,\tau_s}{N_o} = \frac{2}{\sqrt{\pi}}\left[\mathrm{erf}\left(\frac{t_m}{\tau_s}\right) + \mathrm{erf}\left(\frac{t_e - t_m}{\tau_s}\right)\right]^{-1} \tag{4.25}$$

where $\mathrm{erf}(y) = \frac{2}{\sqrt{\pi}}\int_0^y e^{-x^2}\,dx$

Dividing Eqs. (4.15), (4.18) and (4.21) by N_o , ϕ_o and M_2^o respectively and using Eqs. (4.22) and (4.23) we have the dimensionless form of the system

$$\frac{dX_1}{dt'} = K_{fm}N_o\tau_s X_1\left[X_1 Z_{fm_1}^{(0)} + X_2 Z_{fm_b}^{(0)}\right] + \frac{S_{max}\,\tau_s}{N_o} f_s(t) \tag{4.26a}$$

$$\frac{dX_2}{dt'} = \frac{K_{fm}N_o\tau_s}{2}\left[X_2^2 Z_{fm_2}^{(0)} - X_1^2 Z_{fm_1}^{(0)}\right] \tag{4.26b}$$

$$\frac{dX_3}{dt'} = -K_{fm}N_o\tau_s X_1\left[X_1 Z_{fm_1}^{(0)} + X_2 Z_{fm_b}^{(0)}\right] \tag{4.26c}$$

$$\frac{dX_4}{dt'} = \frac{K_{fm}N_o\tau_s}{2v_{g_1}^2\exp\left[18\sigma_{g_1}^2\right]}\left[X_1^2 Z_{fm_1}^{(2)} + X_2^2 Z_{fm_2}^{(2)} + 2X_1X_2 Z_{fm_b}^{(2)}\right]$$

$$- K_{fm}N_o\tau_s X_1\left[X_1 Z_{fm_1}^{(0)} + X_2 Z_{fm_b}^{(0)}\right] \tag{4.26d}$$

This system does not include the terms describing the surface growth mechanism. The development of the terms corresponding to the gas phase surface reactions is presented below in detail.

4.1.2 Surface growth term

Coagulation, the first important mechanism of particle growth, modifies the size distribution of an aerosol but it does not change the particle volume fraction. The other important mechanism of growth, caused by surface gas phase reactions, affects the size distribution and causes an increase in the particle volume fraction. This mechanism is referred to as surface growth. The process involves heterogeneous surface reactions which occur under high concentrations of the condensing species. The rate of these reactions depends on the exchange of matter and heat between a particle and the gas phase.

As discussed in a previous chapter the thermophoretic technique measurements lead to the determination of the specific growth rate f(t) of the soot particles, defined as the rate of gas phase mass deposition on the surface of the particles per unit surface area. The derivation of the form of f(t) from the EM observations did not require any assumptions about the growth species or the growth mechanism. In the following analysis the form of f(t) is considered to be a known function of time.

We consider a polydisperse aerosol growing by surface growth reactions. Following Friedlander's analysis[30] we define I(v,t) to be the particle current or number of particles per unit time and volume of gas passing the point v in the v-space. If n(v,t) the PVDF it can be shown that

$$\left.\frac{\partial n}{\partial t}\right|_g = -\frac{\partial I}{\partial v} \tag{4.27}$$

We now consider the time derivative of M_k due to growth and using Eq. (4.27)

$$\left.\frac{dM_k}{dt}\right|_g = \frac{d}{dt}\left[\int_0^\infty v^k n(v,t)\, dv\right] = \int_0^\infty v^k \left.\frac{\partial n(v,t)}{\partial t}\right|_g dv = -\int_0^\infty v^k \frac{\partial I}{\partial v}\, dv \tag{4.28}$$

From Eq. (4.28) for $k = 0$ we have

$$\left.\frac{dN}{dt}\right|_g = -\left[I\right]_{v=o}^{v=\infty} = 0 \tag{4.29}$$

In Eq. (4.29) we used the fact that there is no loss or gain of particles by growth at the two ends of the distribution. From Eq. (4.28) with $k = 1$

$$\left.\frac{d\phi}{dt}\right|_g = -\left[Iv\right]_{v=o}^{v=\infty} + \int_0^\infty I\, dv = \int_0^\infty I\, dv \tag{4.30}$$

The term in brackets was set equal to zero since there is no loss or gain of material by growth from the two ends of the distribution. Neglecting diffusion in comparison with particle migration in v-space, the particle current can be approximated by

$$I\,(v,t) \approx n\,\frac{dv}{dt} \tag{4.31}$$

For molecular bombardment in the free molecular regime[30]

$$\frac{dv}{dt} = C_{gr}\, v^{2/3} \tag{4.32}$$

where C_{gr} the surface growth coefficient depending on the molecular volume and mass of the growth species, the partial pressure of the gas phase

growth species as well as the temperature. Substituting Eqs. (4.31) and (4.32) in (4.30) we get

$$\left.\frac{d\phi}{dt}\right|_g = C_{gr}\, M_{2/3} \tag{4.33}$$

The total surface area of soot particles available for growth per unit volume of the aerosol is given by

$$S_T = \pi \int_0^\infty n\, D^2\, dv = \left[36\pi\right]^{1/3} M_{2/3} \tag{4.34}$$

If ρ_p the density of the particles and f the time dependent specific growth rate

$$\left.\frac{d\phi}{dt}\right|_g = \frac{f}{\rho_p}\, S_T \tag{4.35}$$

Using Eqs. (4.34) and (4.35), we find

$$\left.\frac{d\phi}{dt}\right|_g = \left[36\pi\right]^{1/3} \frac{f}{\rho_p}\, M_{2/3} \tag{4.36}$$

Comparing Eqs. (4.33) and (4.36) we obtain

$$C_{gr} = \left[36\pi\right]^{1/3} \frac{f}{\rho_p} \tag{4.37}$$

From Eq. (4.28) with k = 2

$$\left.\frac{dM_2}{dt}\right|_g = -\int_0^\infty v^2 \frac{\partial I}{\partial v}\, dv = -\left[Iv^2\right]_{v=0}^{v=\infty} + 2\int_0^\infty Ivdv \tag{4.38}$$

The term in brackets is again zero. Using Eqs. (4.31) and (4.32)

$$\left.\frac{dM_2}{dt}\right|_g = 2\ C_{gr}\ M_{5/3} \tag{4.39}$$

where C_{gr} is given by Eq. (4.37).

Equations (4.29), (4.36) and (4.39) describe the effect of surface growth on the first three moments of the PVDF. As we expect there is no change in the particle number concentration of the aerosol since deposition of material on the surface of the existing particles should not influence N. However, surface growth causes changes in ϕ and M_2 since the size of the particles is affected by the gas phase deposition.

From Eqs. (4.12a) and (4.29)

$$\left.\frac{dN}{dt}\right|_g = \left.\frac{dN_1}{dt}\right|_g + \left.\frac{dN_2}{dt}\right|_g = 0 \tag{4.40}$$

Since there is no certain relation between the influence of the surface growth mechanism and the number concentrations of the two modes, under the restriction expressed by Eq. (4.40), a major assumption is made at this point. The effect of the surface growth mechanism on the first (particle inception) mode is neglected. This assumption is reasonable for aerosol systems where particle inception and surface growth reactions do not coexist. Under this assumption and using the log-normal form of the growth mode Eqs. (4.29), (4.36) and (4.39) take the form

$$\left.\frac{dN_1}{dt}\right|_g = 0 = \left.\frac{dN_2}{dt}\right|_g \tag{4.41a}$$

$$\left.\frac{d\phi_2}{dt}\right|_g = C_{gr}\, N_2\, v_{g_2}^{\,2/3} \exp\left[2\sigma_{g_2}^{\,2}\right] \tag{4.41b}$$

$$\left.\frac{dM_2^2}{dt}\right|_g = 2\, C_{gr}\, N_2\, v_{g_2}^{\,5/3} \exp\left[\frac{25}{2}\,\sigma_{g_2}^{\,2}\right] \tag{4.41c}$$

where $C_{gr} = \left[36\pi\right]^{1/3} \dfrac{f}{\rho_p}$

The quantities v_{g_i} and σ_{g_i} for a log-normal particle size distribution are functions of the first three moments, given by

$$\sigma_{g_i}^{\,2} = \frac{1}{9} \ln\left[\frac{N_i M_2^i}{\phi_i^{\,2}}\right] ; \qquad i = 1,2 \tag{4.42a}$$

$$v_{g_i} = \frac{\phi_i^{\,2}}{N_i^{\,3/2}\, M_2^{i\,1/2}} ; \qquad i = 1,2 \tag{4.42b}$$

Combining these equations for i = 1,2 and using Eqs. (4.22a) - (4.22d) we obtain

$$\sigma_{g_2}^{\,2} = \sigma_{g_1}^{\,2} + \frac{1}{9} \ln\left[\frac{X_2\, X_4}{X_3^{\,2}}\right] \tag{4.43a}$$

$$v_{g_2} = v_{g_1} \frac{X_3^{\,2}}{X_2^{\,3/2}\, X_4^{\,1/2}} \tag{4.43b}$$

Starting from Eqs. (4.41), using (4.22) and (4.43) we obtain the dimensionless form of the contribution of surface growth to the first three moment equations of the PVDF

$$\left.\frac{dX_1}{dt'}\right|_g = 0 = \left.\frac{dX_2}{dt'}\right|_g \tag{4.44a}$$

$$\left.\frac{dX_3}{dt'}\right|_g = C_{gr}\frac{\tau_s}{v_{g_1}^{1/3}\exp\left[\frac{5}{2}\sigma_{g_1}^2\right]} X_2^{2/9} X_3^{8/9} X_4^{-1/9} \tag{4.44b}$$

$$\left.\frac{dX_4}{dt'}\right|_g = 2\,C_{gr}\frac{\tau_s}{v_{g_1}^{1/3}\exp\left[\frac{11}{2}\sigma_{g_1}^2\right]} X_2^{-1/9} X_3^{5/9} X_4^{5/9} \tag{4.44c}$$

where $C_{gr} = \left[36\pi\right]^{1/3} \frac{f}{\rho_p}$

We can now formulate the complete system of equations describing an aerosol system undergoing particle formation, coagulation, and surface growth. The system takes the form

$$\frac{dX_1}{dt'} = K_{fm}N_o\tau_s X_1\left[X_1 Z_{fm_1}^{(0)} + X_2 Z_{fm_b}^{(0)}\right] + \frac{S_{max}\tau_s}{N_o} f_s(t) \tag{4.45a}$$

$$\frac{dX_2}{dt'} = \frac{1}{2}K_{fm}N_o\tau_s\left[X_2^2 Z_{fm_2}^{(0)} - X_1^2 Z_{fm_1}^{(0)}\right] \tag{4.45b}$$

$$\frac{dX_3}{dt'} = -K_{fm} N_o \tau_s X_1 \left[X_1 Z_{fm_1}^{(0)} + X_2 Z_{fm_b}^{(0)} \right] + (36\pi)^{1/3} \frac{f \tau_s X_2^{2/9} X_3^{8/9} X_4^{-1/9}}{\rho_p v_{g_1}^{1/3} \exp\left[\frac{5}{2} \sigma_{g_1}^2\right]} \tag{4.45c}$$

$$\frac{dX_4}{dt'} = \frac{K_{fm} N_o \tau_s}{2 v_{g_1}^2 \exp\left[18 \sigma_{g_1}^2\right]} \left[X_1^2 Z_{fm_1}^{(2)} + X_2^2 Z_{fm_2}^{(2)} + 2 X_1 X_2 Z_{fm_b}^{(2)} \right] -$$

$$- K_{fm} N_o \tau_s X_1 \left[X_1 Z_{fm_1}^{(0)} + X_2 Z_{fm_b}^{(0)} \right] + 2 (36\pi)^{1/3} \frac{f \tau_s X_2^{-1/9} X_3^{5/9} X_4^{5/9}}{\rho_p v_{g_1}^{1/3} \exp\left[\frac{11}{2} \sigma_{g_1}^2\right]} \tag{4.45d}$$

The collision integrals $Z_{fm_i}^{(k)}$; $i = 1, 2, b$ and $k = 0, 2$ are given by Eqs. (4.7) and are functions of σ_{g_i}, v_{g_i}. As we mentioned before $\sigma_{g_1} = \sigma_{g_o}$ and $v_{g_1} = v_{g_o}$ while σ_{g_2}, v_{g_2} can be expressed as functions of the unknown dimensionless moments X_i, through Eqs. (4.43). Details about the evaluation of the collision integrals $Z_{fm_i}^{(k)}$ are given in Appendix A. The above system of equations can be integrated in time numerically using a standard integration package with any set of arbitrary initial conditions. We used a variable step fourth-fifth order Runge-Rutta method developed by Fehlberg[28]. A schematic of the various processes involved in the derivation of the system of Eqs. (4.45) is given in Figure 4.1.

In order to study the relative importance of the particle formation and the surface growth mechanisms we define R_g as the ratio of the integrated particle volume fraction due to surface growth over the integrated volume fraction due to particle formation, when both quantities refer to the same time. So

$$R_g(t) = \frac{\phi(t)\Big|_g}{\phi(t)\Big|_f} \tag{4.46}$$

But

$$\phi(t)\Big|_g = \int_0^t \frac{d\phi}{dt}\Big|_g dt \tag{4.47a}$$

and

$$\phi(t)\Big|_f = \int_0^t \frac{d\phi}{dt}\Big|_f dt \tag{4.47b}$$

From the previous discussion we can write

$$\frac{d\phi}{dt}\Big|_g = \frac{d\phi_2}{dt}\Big|_g \tag{4.48a}$$

and

$$\frac{d\phi}{dt}\Big|_f = \frac{d\phi_1}{dt}\Big|_f \tag{4.48b}$$

Using the dimensionless form of the variables and Eq. (4.17) we obtain

$$R_g(t') = \frac{\displaystyle\int_0^{t'} \left.\frac{dX_3}{dt'}\right|_g dt'}{\displaystyle\int_0^{t'} \left.\frac{dX_1}{dt'}\right|_f dt'} \tag{4.49}$$

From Eq. (4.45a)

$$\left.\frac{dX_1}{dt'}\right|_f = \frac{S_t(t)\ \tau_s}{N_o} \tag{4.50}$$

Substituting Eq. (4.50) in (4.49) and using (4.24) we obtain

$$R_g(t') = \int_0^{t'} \left.\frac{dX_3}{dt'}\right|_g dt' \tag{4.51}$$

The values of the integrand in the above equation are given by Eq. (4.44b) as a function of the dimensionless moments X_i. The integration is performed numerically using the trapezoidal rule.

Another important parameter used to check the validity of the assumption of no growth on the particle inception mode is defined below. We consider the effect of coagulation and surface growth on the particle inception (formation) mode in order to compare their relative importance in the

formulation of the model. The volumetric loss rate of material from the particle formation mode due to surface growth reactions can be found from Eq. (4.36) and is given by

$$\dot{\phi}_g = -C_{gr} N_1 v_{g_1}^{2/3} \exp\left[2\sigma_{g_1}^2\right] \tag{4.52}$$

where C_{gr} is given by Eq. (4.37).

The volumetric loss rate of material from the particle formation mode due to coagulation is obtained from Eqs. (4.17) and (4.15a)

$$\dot{\phi}_c = K_{fm} N_1 \left[N_1 Z_{fm_1}^{(0)} + N_2 Z_{fm_b}^{(0)}\right] v_{g_1} \exp\left[\frac{9}{2} \sigma_{g_1}^2\right] \tag{4.53}$$

The relative importance of the two mechanisms (coagulation and surface growth) on the particle inception mode can be studied by means of the ratio

$$R_{gc} = \frac{\dot{\phi}_g}{\dot{\phi}_c} \tag{4.54}$$

which is proportional to the specific growth rate f (included in the expression for C_{gr}) that is determined experimentally. Small values of R_{gc} support the validity of our assumption. Higher values indicate that the effect of surface growth on the first mode cannot be neglected. During our numerical simulations the surface growth rate was introduced at a later time when the particle inception mechanisms had weakened substantially. This guarantees very low values of the ratio R_{gc}.

4.1.3 Transition from the bimodal to the monomodal integral solution

As we mentioned before a strong particle formation term in the presence of coagulation would result in a bimodal PVDF. The absence of the source term would obviously result in a monomodal configuration[23] mainly due to coagulative growth that results in the transfer of particles from the first to the second mode. This rapid decay of the particle inception mode in the absence of particle formation results in a monomodal form of the PVDF. The only mode describing the aerosol system is then the growth mode and its evolution is described by the following set of equations as derived from the system describing the bimodal solution when $N_1 = 0$

$$\frac{dN_2}{dt} = \frac{1}{2} K_{fm} N_2^2 Z_{fm_2}^{(0)} \tag{4.55a}$$

$$\frac{d\phi_2}{dt} = C_{gr} N_2 v_{g_2}^{2/3} \exp\left[2\sigma_{g_2}^2\right] \tag{4.55b}$$

$$\frac{dM_2^2}{dt} = \frac{1}{2} K_{fm} N_2^2 Z_{fm_2}^{(2)} + 2 C_{gr} N_2 v_{g_2}^{5/3} \exp\left[\frac{25}{2} \sigma_{g_2}^2\right] \tag{4.55c}$$

where

$$C_{gr} = \left[36\pi\right]^{1/3} \frac{f}{\rho_p} \tag{4.37}$$

The wide range of the variables involved in the above system of equations leads once again to a dimensionless formulation. We define

$$Y_1 = \frac{N_2}{N_o} \tag{4.56a}$$

$$Y_2 = \frac{\phi_2}{\phi_o} \tag{4.56b}$$

$$Y_3 = \frac{M_2^2}{M_2^o} \tag{4.56c}$$

where N_o is the total number of particles created over all times per unit volume (see bimodal formulation) and ϕ_o, M_2^o are defined in Eqs. (4.22c) and (4.22d). The log-normal form of the PVDF leads to the following relations

$$\sigma_{g_2}^{\ 2} = \sigma_{g_1}^{\ 2} + \frac{1}{9} \ln \left[\frac{Y_1 Y_3}{Y_2^{\ 2}} \right] \tag{4.57a}$$

$$v_{g_2} = v_{g_1} \frac{Y_2^{\ 2}}{Y_1^{\ 3/2} \ Y_3^{\ 1/2}} \tag{4.57b}$$

Using Eqs. (4.56) and (4.57) in (4.55) we obtain

$$\frac{dY_1}{dt'} = \frac{1}{2} K_{fm} N_o \tau_s Y_1^{\ 2} \ Z_{fm_2}^{(0)} \tag{4.58a}$$

$$\frac{dY_2}{dt'} = \frac{C_{gr} \tau_s}{v_{g_1}^{\ 1/3} \exp\left[\frac{5}{2} \sigma_{g_1}^{\ 2} \right]} Y_1^{\ 2/9} \ Y_2^{\ 8/9} \ Y_3^{\ -1/9} \tag{4.58b}$$

$$\frac{dY_3}{dt'} = \frac{K_{fm} N_o \tau_s}{2 v_{g_1}^{\,2} \exp\left[18\, \sigma_{g_1}^{\,2}\right]} Y_1^{\,2} Z_{fm_2}^{(2)} +$$

$$\frac{2\, C_{gr}\, \tau_s}{v_{g_1}^{\,1/3} \exp\left[\frac{11}{2} \sigma_{g_1}^{\,2}\right]} Y_1^{\,-1/9} \; Y_2^{\,5/9} \; Y_3^{\,5/9} \qquad (4.58c)$$

The transition from the bimodal configuration, described by Eqs. (4.45), to the monomodal configuration described by Eqs. (4.58) happens when the number concentration of the first mode (N_1) is negligible compared to the number concentration of the second mode (N_2). The current values of X_2, X_3, X_4 are used as the initial values of Y_1, Y_2 and Y_3 for the numerical integration of Eqs. (4.58).

An important parameter in the interpretation of the optical data, called the generalized mean diameter or moment ratio[84], is defined by

$$D_{pq}^{\,p-q} = \frac{\int_0^\infty P(D)\, D^p\, dD}{\int_0^\infty P(D)\, D^q\, dD} \qquad (4.59)$$

where D is the diameter of a particle of volume v $\left[D = \left[\frac{6v}{\pi}\right]^{1/3}\right]$ and P(D) is the particle size probability function. The quantity P(D) dD represents the

fraction of all particles contained in the interval D to D + dD and has the property

$$\int_0^\infty P(D)\ dD = 1 \tag{4.60}$$

The particle volume fraction can be written as

$$\phi = \frac{\pi}{6} N D_{30}^3 \tag{4.61}$$

From Eq. (4.59), using the definition of $f_N = \dfrac{N M_2}{\phi^2}$ we can derive

$$D_{63}^3 = \frac{6 M_2}{\pi \phi} = \frac{6 f_N}{\pi N} \phi \tag{4.62}$$

From Eqs. (4.61) and (4.62) we obtain

$$f_N = \left[\frac{D_{63}}{D_{30}} \right]^3 \tag{4.63}$$

For a log-normal distribution the expression for P(D) is given by

$$P(D) = \frac{\exp\left[- \left[\dfrac{\ln D/D_g}{\sqrt{2}\ \sigma_g} \right]^2 \right]}{\sqrt{2\pi}\ \sigma_g\ D} \tag{4.64}$$

where D_g is the geometric mean diameter and σ_g the geometric mean standard

deviation. Using Eq. (4.64) it can be shown that

$$D_{pq} = D_g \exp\left[\frac{p+q}{2}\sigma_g^2\right] \tag{4.65}$$

Using Eqs. (4.63) and (4.65) we find that for a logarithmic normal distribution, f_N is related to σ_g by

$$f_N = \exp\left[9\sigma_g^2\right] \tag{4.66}$$

TABLE 4.1

Nomenclature used in Bimodal Solution

Symbol	Meaning	CGS Units
C_{gr}	surface growth coefficient	$cm\ s^{-1}$
D	particle diameter	cm
D_g	geometric mean diameter	cm
D_{pq}	generalized mean diameter	cm
f	specific surface growth rate	$gr\ cm^{-2}\ s^{-1}$
I	particle current	$cm^{-3}\ s^{-1}$
K	Boltzmann's constant	$erg\ molec^{-1}\ K^{-1}$
K(v,u)	collision frequency factor	$cm^{-3}\ s^{-1}$
K_{fm}	free molecular coefficient	$cm^{5/2}\ s^{-1}$
M_k	k^{th} moment of PVDF	$cm^{3(k-1)}$
n(v,t)	particle volume distribution function	cm^{-6}
N	particle number concentration	cm^{-3}
N_o	number of particles created over all times per unit volume	cm^{-3}
P(D)	particle diameter probability function	cm^{-1}

TABLE 4.1 (Continued)

Symbol	Meaning	CGS Units
$P(v,t)$	particle volume probability function	cm^{-3}
R_g	growth to particle formation volume fraction ratio	
R_{gc}	growth to coagulation volumetric loss rate ratio	
$S(v,t)$	particle formation rate	$cm^{-3}\,s^{-1}$
$S_t(t)$	time dependent source function	$cm^{-3}\,s^{-1}$
S_{max}	maximum value of S_t	$cm^{-3}\,s^{-1}$
S_T	total surface area of particles per unit volume of aerosol	cm^2/cm^3
t	time	sec
T	temperature	K
t_m	time of maximum particle formation rate	sec
u,v	particle volume	cm^3
v_g	geometric mean particle volume	cm^3
$Z_{fm}^{(0)}$	first free molecular collision integral	$cm^{1/2}$
$Z_{fm}^{(2)}$	second free molecular collision integral	$cm^{13/2}$

TABLE 4.1 (Continued)

Symbol	Meaning	CGS Units
Greek		
ρ_p	particle material density	$gr\ cm^{-3}$
σ_g	geometric standard deviation in terms of particle diameter	
σ_v	geometric standard deviation in terms of particle volume	
τ_s	e^{-1} half width of a Gaussian source pulse	sec
ϕ	particle volume fraction	cm^3/cm^3

Subscripts (superscripts for M_2)

o	refers to the particles created by the source
1	refers to the particle inception mode
2	refers to the growth mode
b	refers to the interaction of the two modes

Dimensionless variables

$f_N = N M_2 / \phi^2$; dimensionless second moment

$t' = t/\tau_s$; normalized time

TABLE 4.1 (Continued)

$X_1 = N_1/N_o$ $X_2 = N_2/N_o$ $X_3 = \phi_2/\phi_o$ $X_4 = M_2^2/M_2^o$	normalized quantities when both modes are present
$Y_1 = N_2/N_o$ $Y_2 = \phi_2/\phi_o$ $Y_3 = M_2^2/M_2^o$	normalized quantities when only the growth mode is present

4.2 A monomodal integral solution of the aerosol dynamic equation

In our studies of the aerosol dynamic equation we can use the monomodal integral solution as another approximate method of solution. This method represents the long time solution but it has an inherent weakness when a particle inception term is present; it falsely suppresses the particle formation mode which can be very significant when particle inception is strong. However this solution can accommodate all three physical mechanisms involved in our aerosol dynamic studies: Particle inception, coagulation and surface growth.

The equations describing the evolution of the first three moments of the log-normal PVDF can be derived following the analysis of the previous chapter. The particle formation and surface growth terms are identical with those used in the bimodal solution while the coagulation terms are those describing the growth mode of the bimodal solution when the inception mode vanishes. So

$$\frac{dN}{dt} = \frac{1}{2} K_{fm} N^2 Z_{fm}^{(0)} + S_t(t) \tag{4.67a}$$

$$\frac{d\phi}{dt} = S_t(t)\ v_{g_o} \exp\left[\frac{9}{2}\ \sigma_{g_o}^2\right] + C_{gr}\ N\, v_g^{2/3} \exp\left[2\sigma_g^2\right] \tag{4.67b}$$

$$\frac{dM_2}{dt} = \frac{1}{2} K_{fm} N^2 Z_{fm}^{(2)} + S_t(t)\, v_{g_o}^{\;2} \exp\left[18\sigma_{g_o}^{\;2}\right] +$$

$$2 C_{gr}\, N\, v_g^{\;5/3} \exp\left[\frac{25}{2}\sigma_g^{\;2}\right] \tag{4.67c}$$

where

N, ϕ, M_2 : the first three moments of the PVDF

σ_{g_o}, v_{g_o} : geometric mean volume and mean standard deviation of the particles created by the source term

σ_g, v_g : geometric mean volume and mean standard deviation of the PVDF

$S_t(t)$: Gaussian source term given by Eq. (4.23)

C_{gr} : Surface growth coefficient given by Eq. (4.37)

We use a dimensionless formulation of the above system defining the following variables

$$Y_1 = \frac{N}{N_o} \tag{4.68a}$$

$$Y_2 = \frac{\phi}{\phi_o} = \frac{N\, v_g \exp\left[\frac{9}{2}\sigma_g^{\;2}\right]}{N_o\, v_{g_o} \exp\left[\frac{9}{2}\sigma_{g_o}^{\;2}\right]} \tag{4.68b}$$

$$Y_3 = \frac{M_2}{M_2^o} = \frac{N\, v_g^{\,2} \exp\left[18\sigma_g^{\,2}\right]}{N_o\, v_{g_o}^{\,2} \exp\left[18\,\sigma_{g_o}^{\,2}\right]} \tag{4.68c}$$

where N_o is the total number of particles created over all times per unit volume defined as

$$N_o = \int_0^{t_e} S_t(t)\, dt$$

Using the dimensionless time $t' = \dfrac{t}{\tau_s}$ the system (4.67) takes the form

$$\frac{dY_1}{dt'} = \frac{1}{2} K_{fm} N_o \tau_s Y_1^{\,2} Z_{fm}^{(0)} + S(t) \tag{4.69a}$$

$$\frac{dY_2}{dt'} = S(t) + \frac{C_{gr}\,\tau_s}{v_{g_o}^{\,1/3} \exp\left[\frac{5}{2}\sigma_{g_o}^{\,2}\right]} Y_1^{\,2/9}\, Y_2^{\,8/9}\, Y_3^{\,-1/9} \tag{4.69b}$$

$$\frac{dY_3}{dt'} = \frac{K_{fm} N_o \tau_s}{2\, v_{g_o}^{\,2} \exp\left[18\sigma_{g_o}^{\,2}\right]} Y_1^{\,2}\, Z_{fm}^{(2)} + S(t) + \frac{2\, C_{gr}\,\tau_s}{v_{g_o}^{\,1/3} \exp\left[\frac{11}{2}\sigma_{g_o}^{\,2}\right]} Y_1^{\,-1/9}\, Y_2^{\,5/9}\, Y_3^{\,5/9} \tag{4.69c}$$

where $S(t) = S_t(t)\, \tau_s / N_o$

In the derivation of the above equations we used the following expressions of σ_g, v_g because of the log-normal form of the PVDF

$$\sigma_g^{\,2} = \sigma_{g_o}^{\,2} + \frac{1}{9} \ln \left[\frac{Y_1 Y_3}{Y_2^{\,2}} \right] \tag{4.70a}$$

$$v_g = v_{g_o} \frac{Y_2^{\,2}}{Y_1^{\,3/2} \cdot Y_3^{\,1/2}} \tag{4.70b}$$

The collision integrals $Z_{fm}^{(k)}$ (k=0,2) according to Eq. (4.7) are functions of σ_g, v_g which are related to Y_i through Eqs. (4.70). These integrals are calculated by various interpolation formulae presented in detail in Appendix A. The three coupled ordinary differential equations (4.69) are integrated numerically in time using a standard variable step fourth-fifth order Runge-Kutta technique, developed by Fehlberg[28].

As in the case of the bimodal solution, we define R_g as the ratio of the integrated particle volume fraction due to surface growth over the integrated volume fraction due to particle inception at a specified time t. Using dimensionless variables it can be shown that

$$R_g(t') = \int_0^{t'} \left. \frac{dY_2}{dt'} \right|_g dt' \tag{4.71}$$

The values of the integrand in the above equation are given by the last term of the RHS of Eq. (4.69b).

TABLE 4.2

Nomenclature used in Monomodal Solution

Symbol	Meaning	CGS Units
C_{gr}	surface growth coefficient	$cm\ s^{-1}$
K_{fm}	free molecular coefficient	$cm^{5/2}\ s^{-1}$
M_2	second moment of the PVDF	cm^3
N	particle number concentration	cm^{-3}
N_o	number of particles created over all times per unit volume	cm^{-3}
R_g	surface growth to particle formation volume fraction ratio	
$S_t(t)$	time dependent source function	$cm^{-3}s^{-1}$
t	time	sec
v_g	geometric mean particle volume	cm^3
$Z_{fm}^{(0)}$, $Z_{fm}^{(2)}$	first and second free molecular collision integrals	$cm^{1/2}$, $cm^{13/2}$
Greek		
σ_g	geometric standard deviation in terms of particle diameter	

TABLE 4.2 (Continued)

Symbol	Meaning	CGS Units
τ_s	e^{-1} half width of a Gaussian source pulse	sec
ϕ	particle volume fraction	cm^3/cm^3

Subscripts (superscripts for M_2)

o	refers to the particles created by the source

Dimensionless variables

$t' = \frac{t}{\tau_s}$; normalized time

$$\left.\begin{aligned} Y_1 &= \frac{N}{N_o} \\ Y_2 &= \frac{\phi}{\phi_o} \\ Y_3 &= \frac{M_2}{M_2^o} \end{aligned}\right\} \text{normalized moments of the PVDF}$$

4.3 Other models for simulating aerosol dynamics

Another existing model studying the aerosol dynamic behavior is presented in this section in order to make detailed comparisons with the integral solutions analyzed in the previous chapters. The model, called MAEROS, was developed by Gelbard and Seinfeld[32,33] for simulating the evolution of aerosol size and chemical composition distributions resulting from coagulation, intraparticle chemical reaction, gas to particle conversion and particle generation by a source mechanism. The technique is based upon dividing the entire particle size domain into m arbitrarily located sections. The particle masses of section j range from v_{j-1} to v_j where j = 1, m. Imposing conservation of mass for each of the s components for all the processes described above and approximating a form of the distribution function as a constant within each section, results in a set of m by s differential equations for the mass concentrations $Q_{j,k}$ of component k in section j (j = 1,2 . . . m; k = 1, . . . s). This set of equations is integrated in time using the fourth-fifth order Runge-Kutta method developed by Fehlberg[28]. The available code is limited in section refinement such that $v_j \geqslant 2\ v_{j-1}$ and $5 \leqslant m \leqslant 20$. In order to make comparisons with the integral solution we considered only one component (s = 1) and assumed no intraparticle chemical reaction and no surface growth. The coagulation coefficient was assumed to be that corresponding to free molecular coagulative growth (see Eq. 4.4). The Gaussian form of the particle formation rate was used (Eq. 4.23) to describe the source term generating particles within the first section. The particle mass distribution function n(v,t) is defined such that n(v,t) dv is the number

concentration of particles in the mass range [v, v + dv] at time t. Since there is only one chemical component we have

$$Q_j(t) = \int_{v_{j-1}}^{v_j} v\ n(v,t)\ dv \tag{4.72}$$

where Q_j is the mass concentration of aerosol particles in section j (j = 1,2, . . . m). It is obvious that the volume fraction over all sizes is given by

$$\phi(t) = \frac{1}{\rho_p} \sum_{j=1}^{m} Q_j(t) \tag{4.73}$$

where ρ_p is the density of the aerosol particles.

This technique considers only conservation of mass (volume). So in case we want to derive some information about the other moments of the distribution function we have the relate $Q_j(t)$ to n(v,t). Following Gelbard and Seinfeld's[33] analysis we choose the diameter D as the size variable of interest related to the mass v through

$$D = \left[\frac{6v}{\pi \rho_p}\right]^{1/3}$$

After a series of assumptions it can be shown that the particle mass

distribution function in section j is given by

$$n(v,t) = \frac{Q_j}{v^2 \ln \frac{v_j}{v_{j-1}}} \tag{4.75}$$

Then the number concentration in section j is given by

$$N^j(t) = \int_{v_{j-1}}^{v_j} n(v,t)\, dv = \frac{Q_j}{\ln\left[\frac{v_j}{v_{j-1}}\right]} \left[\frac{1}{v_{j-1}} - \frac{1}{v_j}\right] \tag{4.76}$$

The number concentration over all sizes is given by

$$N(t) = \sum_{j=1}^{m} N^j(t) \tag{4.77}$$

The sectional second moment, as defined through the PVDF corresponding to section j, can be obtained as

$$M_2^j(t) = \int_{v_{j-1}}^{v_j} \frac{v^2}{\rho_p^{\,2}}\, n(v,t)\, dv \tag{4.78}$$

Using Eq. (4.75) we have

$$M_2^j(t) = \frac{Q_j \left[v_j - v_{j-1}\right]}{\rho_p^{\,2} \ln\left[\frac{v_j}{v_{j-1}}\right]} \tag{4.79}$$

The second moment of the PVDF is then

$$M_2(t) = \sum_{j=1}^{m} M_2^j(t) \tag{4.80}$$

Equations (4.73), (4.77) and (4.80) provide the variables used to compare MAEROS to the integral solutions. We have to emphasize that the MAEROS solution does not assume a form for the distribution function. However the fact that it preserves only the volume, introduces a degree of approximation in the evaluation of the various moments of the PVDF except from the particle volume fraction.

A test related to the above approximation was performed choosing the volume as the size variable of interest, instead of the diameter D. For this case the sectional approximation of the distribution function assumes the form

$$n(v,t) = \frac{Q_j}{v\left[v_j - v_{j-1}\right]} \tag{4.81}$$

which substantially differs from Eq. (4.75) that was derived using the diameter D as the size variable of interest. These two forms of n(v,t), i.e. Eqs. (4.75) and (4.81), were used in an example describing free molecular coagulation in the presence of a Gaussian source pulse with the following values of the primary variables

$T = 2000\,K$, $t_m = 0.01$ sec, $\tau_s = 0.005$ sec, $N_o = 1.735 \times 10^{19}\ cm^{-3}$

$\rho_p = 2\ g/cm^3$, $D_{g_o} = 10$ nm and $\sigma_{g_o} = 0.0$.

The values of N and M_2 differ by as much as 5% from each other for the time interval $0 \leq t \leq 0.15$ sec. This example clearly illustrates the

dependence of the results on the choice of the sectional form of the size distribution function.

A more severe test of the assumptions introduced to calculate N and M_2 is performed for the case of a constant coagulation coefficient where an exact solution can be obtained analytically[23]. A comparison was made for a constant source term creating monodisperse particles over a specified time interval (rectangular source pulse). The two different forms of the sectional distribution function given by Eqs. (4.75) and (4.81) were used. It proved that the sectional form of the distribution function when the diameter is chosen as the variable of interest (Eq. 4.75) gave results in good agreement with the exact solution for the number concentration (within 4%), while the values of the second moment were systematically in error within 12%. However when the volume was chosen as the variable of interest the agreement was less favorable. This test resulted in the choice of Eq. (4.75) over Eq. (4.81) for the sectional representation of the distribution function.

The above examples clearly indicate the approximation introduced by the sectional form of the distribution function and address the fact that the technique should be treated as another approximate solution.

The sectional multicomponent aerosol model has been significantly expanded recently by Warren and Seinfeld[97]. The new model, called ESMAP, incorporates the mechanisms of homogeneous nucleation and condensation that are coupled to the vapor phase and conserve particle number concentration. The model allows examination of the balance between new particle formation and particle growth as well as coagulation and deposition mechanisms.

A comparative review by Seigneur et al.[87] of mathematical models of aerosol dynamics was recently published. Three different approaches were considered based on continuous, discrete (sectional) and parametrized (log-normal) representations of the aerosol size distribution. The results of this study provide useful information for the selection of an aerosol model, depending on the accuracy requirements and computational constraints associated with a specific application.

TABLE 4.3

Nomenclature used in MAEROS Solution

Symbol	Meaning	CGS Units
D	particle diameter	cm
M_2^j	sectional second moment of the PVDF for particles in section j	cm^3
M_2	second moment of the PVDF	cm^3
$n(v,t)$	particle mass distribution function	$gr^{-1}cm^{-3}$
N^j	particle number concentration in section j	cm^{-3}
N	particle number concentration over all sections	cm^{-3}
Q_j	mass concentration of particles in section j	$gr\ cm^{-3}$

TABLE 4.3 (Continued)

Symbol	Meaning	CGS Units
$Q_{j,k}$	mass concentration of component k in section j	gr cm^{-3}
t	time	sec
v	particle mass	gr
Greek		
ρ_p	particle material density	gr cm^{-3}
ϕ	particle volume fraction	cm^3/cm^3

4.4 Comparisons of the models

The two forms of the integral solution (monomodal and bimodal) are now subject to a detailed comparison with the MAEROS solution in order to investigate the reliability of the data obtained by both methods. A number of special cases is considered and the results are presented below.

The initial value problem (no source term) with free molecular collision frequency is examined first. For this example only the monomodal form of the integral solution is used since there is no particle generation term. In this case both solutions are approximate and no positive statement can be made for the accuracy of either one, since no analytical solution is available. In the example considered, the time evolution of an aerosol undergoing free molecular coagulation is studied. The initial number concentration is $N_o = 10^{11}$ cm^{-3} and the particles of density $\rho_p = 2$ gr/cm^3 are initially monodisperse with D = 10 nm. The temperature of the aerosol is T = 2000 K (flame-like conditions). Twenty sections geometrically spaced in particle diameter from 8.96 to 911 nm were used for the MAEROS solution. The particles formed by the source term had a diameter corresponding to the average diameter of the first section which was D = 10 nm. The values of N obtained by both methods were within 2% while the values of M_2 were within 17% for the time interval $0 \leq t \leq 0.23$ sec.

Another test for the accuracy of the two methods examined, is performed by the asymptotic value of the dimensionless second moment f_N defined by

$$f_N = \frac{N M_2}{\phi^2}$$

The MAEROS solution gives $f_N = 2.66$ while the monomodal integral solution gives $f_N = 2.27$, both at $t = 0.23$ sec. These values are in error by 28% and 9% respectively from the value $f_{N\infty} = 2.079$ recommended by Graham and Robinson[37] for a normalized form of the self-preserving distribution function obtained by Lai et al[57]. As we mentioned previously, the self-preserving distribution function is the asymptotic form of the PVDF for an aerosol undergoing free molecular coagulation by Brownian motion. The asymptotic value for the monomodal integral solution[23] is $f_{N\infty} = 2.297$, a 10.5% discrepancy from Graham and Robinson's value. However the MAEROS solution fails to give a reliable asymptotic value for f_N because of a finite upper limit loss due to rapid coagulative growth of the particles at relatively high concentrations. The rapid increase of the particle size causes the early arrival of a large number of particles to the upper end of the diameter range, soon producing an undesirable loss of particulate material from the end of the distribution. The finite upper limit loss results in the inability of the code to comply with the volume preservation requirement thus distorting the predictions of the model.

A more thorough comparison of the integral solutions with MAEROS is performed below for the case of free molecular coagulation with a Gaussian source pulse. The evolution of an aerosol is studied under "flame-like" temperature conditions; $T = 2000$ K. Particles with $\rho_p = 2$ gr/cm^3, $D_{go} = 5$nm and $\sigma_{go} = 0.1$ are generated by a Gaussian source pulse with $t_m = 0.03$ sec, $\tau_s = 0.01$ sec, shown in Figure 4.2A. This source term creates a steady increase of ϕ during the time interval in which it is still active. The particle volume fraction maintains a constant level after the time where the source becomes negligible as shown in Figure 4.2B. The total number of particles

created over all times is $N_o = 4 \times 10^{13}$ cm^{-3} and the time interval studied $0 \leq t \leq 0.25$ sec. Once again the unavailability of an exact solution does not permit any positive statement about the accuracy of the methods. The CPU times for this particular case on a Micro-VAX were; 14 sec for the monomodal integral solution, 460 sec for the bimodal, and 214 sec for the MAEROS solution. A series of figures provides the comparison of the three methods. In Figure 4.3 the number concentration and second moment profiles for the three methods are compared. As we see the agreement of the number concentration profiles is rather good, except during the time interval where the source term decays rapidly. The bimodal solution is closer to the MAEROS solution as expected, since the monomodal solution suppresses the particle formation mode thus distorting the actual form of the distribution. Finally the MAEROS solution gives consistently higher values for the second moment and the ratio f_N as shown in Figure 4.4. It is also clear from the previous figures that both forms of the integral solution tend to converge at very late times.

The MAEROS solution is unable to give an asymptotic value of any of the variables, since the long simulation times are associated with a substantial loss of particulate material from the upper end of the size distribution. This fact is demonstrated by Figure 4.5 which shows the time evolution of the mass concentration histograms of the aerosol. The bimodal configuration is clear at a time where the source term is strong ($t = 0.02$ sec) as shown in Figure 4.5A. The distribution assumes the monomodal configuration (Figure 4.5B) immediately after the particle formation term is turned off. The mass concentration histogram at $t = 0.16$ sec shows that the

largest particles have already reached the upper limit of the diameter range used in the calculation (Figure 4.5C). In fact the loss of material becomes important at a later time (t = 0.20 sec) where a substantial decay in the values of the volume fraction is observed. In order to avoid the finite upper limit loss a new definition of the diameter sections is required corresponding to larger sizes.

Figure 4.6 presents the particle size distribution function n(v,t) computed with the two forms of the integral solution at a time t = 0.03 sec, when the source term achieves a maximum. The bimodal solution gives a very wide growth mode (σ_{g2} = 0.517) due to intense coagulation between the particles. The monomodal solution gives an even wider PVDF corresponding to σ_g = 0.603. The bimodal character of the PVDF is clearly indicated in the figure, from which one can see that a log-normal or self preserving form would be obviously inappropriate to represent this distribution. Frenklach and Harris[29] came to the same conclusion using a discrete model to examine a problem with simultaneous nucleation, coagulation and surface growth (see Fig. 6 in ref. 29).

An important point is brought up by the form of the PVDF shown in Figure 4.6 for the bimodal solution. The particles formed by the source mechanism are characterized by a geometric mean volume v_{go} and a standard deviation σ_{go} which define the lower limit of the particle sizes involved in the calculation. Strong coagulation during the time when the source term is active creates a rapid broadening of the growth mode (Figure 4.9) which at the time corresponding to Figure 4.6 is characterized by a value of σ_{g2} = 0.517. This broad distribution in the numerical calculation creates an

artifact with no natural meaning i.e., particles of substantially smaller size than v_{go} are present in relatively high concentrations as depicted clearly by Figure 4.6. However the effect of those small particles in the integral evaluation of N is surprisingly low as illustrated in Figure 4.3A which shows very good agreement of the profiles for all three solutions. This indicates the significance of the right hand side of the distribution function in Figure 4.6 (corresponding to higher values of the volume) which almost coincides for both forms of the integral solution.

The importance of the presence of the smaller particles in the numerical evaluation of the higher moments is expected to be much lower, since n is multiplied by the volume v or v^2 for the calculation of ϕ and M_2 respectively. This above numerical artifact of the bimodal solution is present only during the time when the source term is active as shown in Figure 4.7 which shows the PVPF of the growth mode at various times. We can see that the growth mode becomes very broad when the source term is strong. The PVPF moves quickly toward larger sizes after the source term vanishes. The numerical artifact discussed above is expected to be weaker when a very narrow Gaussian source pulse is used to represent the particle formation mechanisms.

Figure 4.8 presents the number concentration and volume fraction profiles corresponding to the two modes, as calculated using the bimodal integral solution. At the early stage ($0 \leq t << t_m$) N_1 accounts for almost all the total number concentration of the aerosol. At the region of maximum formation rate ($t \approx t_m$) N_2 is appreciably higher than before but always smaller than N_1. Both N_1 and N_2 peak near t_m with N_1 decaying very

rapidly thereafter. It is apparent that $N_1 \approx N_2$ when the source term has a maximum, corresponding to quasi equilibrium between the coagulation and particle inception mechanisms expressed by $dN/dt \approx 0$. Comparing the volume fraction profiles for the two modes we conclude that even at the moment of peak formation rate, where ϕ_1 achieves a maximum, ϕ_2 accounts for almost all the total volume fraction, i.e., $\phi_2 \approx \phi$. At later times when the source term becomes very weak or negligible, N_2 accounts for the biggest part of N since the source cannot further support the loss of particles from the inception mode due to intense coagulation. Figure 4.9 presents the variation of the geometric standard deviation of the growth mode σ_{g2} with time. As we see a strong particle formation rate implies a very wide distribution function due to explosively intense coagulation. After the source term weakens substantially the value of σ_{g2} converges to a value $\sigma_{g2} \approx 0.3$. The bimodal solution finally reduces to the monomodal one after the source term has terminated and the inception mode vanishes.

4.5 Bimodal solution predictions for the soot aerosol in the coannular ethene/air diffusion flame.

The bimodal solution is now used to model the soot formation processes in the axisymmetric ethene/air diffusion flame under investigation. The formation, growth and transport of soot particles along the path line merging with the annular region at a height z=15 mm (see Fig. 3.22) is studied in detail. As discussed previously during the experimental investigation of the soot field, these particles are first formed between the flame sheet and the annular region. The particle inception stage occurs in the lowest regions of the flame and its characteristic time is of the order of 1 ms. The newly formed particles follow the path lines leading to the interior of the flame and at the same time they are convected upwards to higher axial locations. During this transport the particles grow through surface growth reactions, while agglomeration results in the reduction of their number concentration. Finally the particles move into the upper oxidation region of the flame where they are ultimately depleted under the attack of the oxidative species.

According to Figure 3.22 the path line which merges with the annular region at a height z=15 mm, crosses the flame sheet at an axial location z=4 mm. Since the exit plane of the fuel nozzle was chosen as the initial location (t=0) for the calculation of the particle residence times, this event corresponds to t=16 ms. Combining the information provided by Figure 2.6A and B, reproduced from refs. 86 and 81 respectively, we can calculate the residence times t corresponding to various axial locations z, for the particles being transported along the path line merging with r_c at z=15 mm. The values of t

and z are given in the following table

TABLE 4.4

Residence Time Data[a] for Particles Ultimately Transported on the Annular Region

z (mm)	4	5	10	15	20	30	40
t (ms)	16	20	28	34	39	47	54

[a] Data from ref. 81.

This table suggests that the particles are created over a time interval which starts at an instant $t \geqslant 16$ ms. These particles follow a path that merges with the annular region at a time $t \approx 34$ ms, as they are transported upwards. This implies that the transport of these particles, from the region where they are formed ($z \approx 4$ mm) to radial positions corresponding to the annular region ($z \approx 15$ mm), does not last longer than 18 ms. During this transport the particles grow and their surface growth rate is expected to be lower than that calculated from the data of the thermophoretic method for particles corresponding to $r=r_c$. As soon as the particle path merges with the soot annulus, the surface growth processes can be described by the growth rates of particles transported along the annular region. These rates, which were derived by EM observations described previously, are given in Table 3.1.

The value of the surface growth rate at a height z=10 mm for the path line under investigation, is expected[68] to be lower than that of 9.4×10^{-5} g/cm^2 s which corresponds to the annular region. Assuming a value of 7.5×10^{-5} g/cm^2 s, a second order polynomial fit of the surface growth rate along this

particular path line gives f(t) for t≥20.5 ms as

$$f(t) = A + Bt + Ct^2 \quad ; \qquad [g/cm^2\ s \quad ; t \text{ in sec}]$$

where $A=-0.443\times10^{-3}$, B=0.030 and C=-0.410. The above equation was used during the numerical simulation, to describe the specific growth rate derived using the thermophoretic sampling method, for residence times t≥20.5 ms, and f=0 for t<20.5 ms.

As we mentioned previously, the bimodal solution assumes particles of spherical shape. The calculated values of f(t) were obtained from measurements of the actual soot aggregates examining a series of electron micrographs. Let us consider an aggregate of volume V_a which consists of N_p primary particles of uniform diameter D_p. If we neglect the bridging of the particles, the total surface of the aggregate is given by

$$S_a = \pi N_p D_p^{\ 2}$$

Considering the equivalent sphere of volume V_a we calculate its surface area as

$$S_{eq} = \pi N_p^{\ 2/3}\ D_p^{\ 2}$$

We then calculate the ratio

$$f_R = \frac{S_a}{S_{eq}} = N_p^{\ 1/3} \tag{4.82}$$

This ratio, which can be very different from unity, is a result of the nonspherical character of the soot aggregates. It is used in the numerical simulation as a multiplicative factor of the calculated values of f(t), in order

to compensate for the smaller area of the aggregated particles when they are considered to have a spherical shape.

The variables of the numerical simulation are the following quantities: t_m, τ_s describing the Gaussian source pulse used to simulate the particle inception mechanisms along the path line ultimately merging with the soot annulus at z=15 mm, N_o giving the total number of particles per unit volume generated by the particle inception mechanisms along the same path, D_{g_o} and σ_{g_o} describing the log-normal size distribution of the incipient soot particles, and finally f_R defined by Eq. (4.82) which accounts for the nonsphericity of the soot aggregates.

The data acquired through the optical method provide information on volume fraction, particle size and number concentration of the soot aerosol for particles corresponding to the annular region. Figure 2.7 reproduced from ref. 86, which describes the results of optical observations from the soot field of this flame, was used to retrieve the following information

TABLE 4.5

Selected Optical Data for Particles in the Annular Region of the Ethene Diffusion Flame

t (ms)	z (mm)	ϕ (cm^3/cm^3)	D_{63} (nm)	N (cm^{-3})
20	5	3.7×10^{-7}	20	$>10^{11}$
28	10	1.8×10^{-6}	73	1.8×10^{10}
34	15	3.7×10^{-6}	110	1.1×10^{10}
39	20	5.2×10^{-6}	135	8.7×10^{9}
47	30	8.0×10^{-6}	150	8.6×10^{9}
54	40	8.0×10^{-6}	140	1.3×10^{10}

The values listed on the above table were taken using the extrapolated curves of Figure 2.7 labeled 3.85 cc/s. The reliability of the optically calculated quantities decreases from ϕ to N. These quantities were calculated using Mie light-scattering analysis for polydisperse spheres, with a self-preserving size distribution function and a complex refractive index $\tilde{m}$=1.57-0.56i. As we see this series of assumptions causes some questions related to the reliability of the data acquired through the optical method.

The particle volume fraction profile $\phi(t)$ is used as the most reliable quantity in our numerical simulations. The values shown in table 4.5 correspond to the annular region of the flame at all heights. Thus they do not describe the particles whose path ultimately merges with r_c, for heights below z=15 mm. At a height z=10 mm the peak value of ϕ was found to be 1.8×10^{-6} cm^3/cm^3. Using Figure 3.22 we estimate that the particles under investigation cross the axial location z=10 mm at a radial position 0.5 mm outside r_c. This corresponds to a reduction of the related value of ϕ, suggesting that at z=10 mm (t=28 ms) the numerically calculated ϕ should therefore be lower than the one corresponding to the annular region.

An additional constraint suggested by the optical measurements was imposed on the numerical simulation. Equation (2.1) was used to calculate Q_{vv} as a function of residence time for the particles being transported on the path under investigation. These values of Q_{vv} are valid only when the particles are in the Rayleigh regime. This means that the calculated values of Q_{vv} have to be consistent with the optically determined ones for heights $z \leq 10$ mm ($t \leq 28$ ms), where the Rayleigh theory can describe the soot aerosol reliably. From the

optical data we obtain that the lowest Q_{vv} signal that can be detected is of the order of $1x10^{-8}$ $cm^{-1}str^{-1}$. Using Figure 3.22 and refs. 85 and 86 for the particles whose path merges with r_c at z=15 mm, we obtain $Q_{vv}<10^{-8}$ $cm^{-1}str^{-1}$ and $Q_{vv}=3.x10^{-5}$ $cm^{-1}str^{-1}$ corresponding to heights z=5 mm and z=10 mm respectively. The numerical simulations of the soot aerosol using the bimodal integral solution have to be consistent with these two conditions in order to be acceptable.

A Gaussian source pulse creating almost monodisperse particles (σ_{g_o}=0.1) is used to simulate the particle inception mechanisms along the path ultimately merging with the soot annulus. The incipient soot particles are small (D_{g_o}=1.5 nm), and are generated over a short time interval. The time of maximum particle formation rate (t_m) was chosen to correspond to a position close to the flame sheet on the fuel rich region. The total number of particles per unit volume generated by the source pulse was of the order of 10^{13} cm^{-3}. We assumed a soot density of 1.86 g/cm^3 according to refs. 19,64,67 and a constant temperature T=2000 K for the soot aerosol. The value of f_R was found to be 3.7 in order to account for the sharp increase of ϕ over the range 10 to 30 mm of heights above the burner mouth. The following set of variables was used as one that gives agreement between the ϕ profiles calculated using the bimodal solution, and the values determined by the optical method:

t_m=17.5 ms, τ_s=0.6 ms, $N_o=1.2x10^{13}$ cm^{-3}, D_{g_o}=1.5 nm, σ_{g_o}=0.1, and f_R=3.7

The above set of variables satisfied the constraint of compatibility of the calculated Q_{vv} values with the ones determined optically.

The assumption of no growth on the particle inception mode is now checked in order to assure the validity of the simulation. The bimodal character of the solution is preserved until the time t=23.5 ms, where the transition to the monomodal configuration occurs. At this instant it is $N_2/N_1 \approx 500$. The surface growth rate achieves non zero values after t=20.5 ms when $N_2/N_1 \approx 22$. This means that when the surface growth term enters the calculation, the bimodal distribution is such that less than five percent of the particle population belongs to the inception mode. At times t=21 and 22 ms the ratio N_2/N_1 achieves values 36 and 90 respectively. The rapidly decreasing ratio N_2/N_1 during the time period $20.5<t<23.5$ ms, illustrates the insignificant error introduced when we neglect the surface growth mechanisms acting on the particle inception mode.

Figure 4.10 shows the particle volume fraction profile calculated by the bimodal solution which was used to fit the profile determined experimentally using the optical tests. The particle generation mechanisms create over a short period of time an initial soot loading of about $2.\times10^{-8} cm^3/cm^3$, which is very low compared to the loading higher up in the flame. Surface growth reactions cause a significant increase of the soot volume fraction thereafter, up to the higher portions of the flame where the reactivity of the particles decreases drastically and these reactions terminate. This is the point where oxidation mechanisms start to dominate thus causing a gradual decrease of ϕ with time. The oxidation mechanisms have not been modeled in the bimodal solution.

Figure 4.11A shows the calculated particle diameter D_{63} versus residence time. The values found using the optical and thermophoretic

techniques are also shown. We can see that the predictions of the model are consistently lower than the experimental values. Figure 4.11B shows the particle number concentration, as calculated by the bimodal solution, to achieve a maximum at $t=t_m$. The number concentration subsequently decreases monotonically with time as a result of coagulative mechanisms. The optical data corresponding to intermediate heights of the flame are also displayed. Figure 4.12A displays the variation of f_N as calculated by the bimodal solution. The dimensionless second moment achieves a maximum at the time of maximum particle inception rate (t_m), and subsequently decreases because of the intense surface growth mechanisms. As the surface growth rate weakens at later times, f_N converges slowly to the value corresponding to the self preserving distribution function. This value cannot be achieved in the short time available because of the presence of particle inception or surface growth processes throughout the lower and intermediate regions of the ethene diffusion flame. Figure 4.12A also demonstrates the numerical result that higher values of f_N are associated with intense particle generation mechanisms. Low values of f_N result due to surface growth reactions which tend to narrow the size distribution. This is illustrated at the time interval during which the surface growth mechanisms are active, thus causing the values of f_N to drop below the value corresponding to the self-preserving form. The coagulative mechanism of growth tends to broaden the distribution causing an increase of f_N. The simultaneous presence of both growth processes creates a competition that results in the dominance of the surface growth reactions. However it is clear that the values of f_N throughout the period of intense surface growth reactions are not very different from the self-preserving value. The result of the above numerical simulation is in agreement with the studies of Bockhorn et al.[3]

on low pressure hydrocarbon/oxygen premixed flat flames. In these flames they estimated the duration of particle inception to be 2 to 3 ms assuming an incipient particle diameter of 1.5 nm.

Figure 4.12B shows the particle inception pulse S_t used during the numerical simulation. We see that a maximum inception rate of about 1.1×10^{16} $cm^{-3}s^{-1}$ was employed in order to simulate the first stage of the soot related processes in the ethene diffusion flame. The e^{-1} half width of the pulse τ_s=0.6 ms and its value affects the maximum value of S_t. A higher value of τ_s would decrease the corresponding values of S_t. A favorable reproduction of the experimentally determined volume fraction profile, can only be obtained using particle inception rates above the value of 10^{16} cm^{-3} s^{-1}. A sensitivity analysis related to the values of the particle inception rate was also performed. Using an incipient particle size of D_{g_o}=1 nm we obtained an equally good fit of the volume fraction profile with $N_o=4.2 \times 10^{13}$ cm^{-3} and the rest of the variables unchanged. During this simulation a maximum particle inception rate of 3.9×10^{16} cm^{-3} s^{-1} was employed. Once again the numerically calculated values of Q_{vv} were consistent with the optically determined ones.

Figure 4.13 shows the Q_{vv} time variation corresponding to the lower portion of the flame as calculated by the bimodal solution using Rayleigh scattering theory. As we see the Q_{vv} signal would not be detectable for $t \leq 20$ ms. This means that the optical method can not "see" the particle inception stage but starts detecting the particles at a later stage when they have grown over a certain size. This numerical result demonstrates that the particle concentration increase in the region of the flame sheet can be associated with the formation of large numbers of small particles (incipient particles). The

existence of the particle inception pulse, that is inferred by the application of the aerosol dynamic equation as depicted in Figure 4.12B, is seemingly impossible to verify experimentally. At this height, z=3-5 mm, the optical experiment does not yield results because the transmission is too low to permit any measurement in a reliable manner. The thermophoretic experiment lacks the spatial resolution that is necessary to identify a particle inception pulse, which is marked by coexisting coagulative growth at early times and surface growth soon thereafter. Thus the particle inception pulse is inferred largely by a process of numerical extrapolation at earlier times. While this procedure brings into question the accuracy of the derived inception rate, the importance of these attempts to understand the early events cannot be doubted.

Our studies concluded that the soot inception rate for the ethene diffusion flame is almost three orders of magnitude higher than that determined by Wersborg et al.[98] for a low pressure acetylene/oxygen premixed flat flame. In that flame they observed a maximum soot volume fraction smaller by a factor of 500 (ϕ=1.5x10^{-8} cm^3/cm^3) while the incipient particle size was assumed to be 1.5 nm. The maximum number concentrations were of the order of 10^{10} cm^{-3}. Bockhorn et al.[3] reported a particle inception rate of the order of 10^{14} cm^{-3} s^{-1} for their low pressure premixed flat flames assuming an incipient particle diameter of 1.5 nm. Harris et al.[42] calculated an inception rate of 10^{16} cm^{-3} s^{-1} for an atmospheric pressure premixed ethene/argon/oxygen flat flame. They considered a particle inception pulse with a duration of 2-3 ms generating particles of the same size (1.5 nm), and they observed number concentrations as high as 10^{12} cm^{-3}. In their calculation they used a constant coagulation coefficient as Wersborg et al. did. Kent et

al.[51] determined an inception rate of 10^{15} cm^{-3} s^{-1} for an atmospheric pressure laminar ethene diffusion flame on a Wolfhard-Parker burner. As we see the inception rates calculated through our numerical simulations are generally in agreement with the rates reported previously for the ethene flames. The variety of the flame conditions, not to mention the uncertainties involved in the calculations, could certainly account for the different values of particle inception rate that are reported.

As described previously the quantity R_g is defined as the ratio of the integrated particle volume fraction due to surface growth, over the integrated volume fraction due to particle formation. This quantity expresses the relative contribution of the two growth mechanisms to the final soot loading inside the ethene diffusion flame. The numerical simulation gave a value of $R_g \approx 500$ corresponding to a height z=40 mm (onset of oxidation). This means that only 0.2% of the final soot volume fraction is due to the particle inception mechanisms, while 99.8% is due to soot surface growth reactions. This result is in agreement with previous studies performed by Harris and Weiner[38,39,41] (atmospheric pressure premixed ethene-air flat flames), and Bockhorn et al.[3] (low pressure premixed hydrocarbon-oxygen flat flames) who concluded that surface growth accounts for the bulk of soot generated in the flames they studied.

Another significant result of the numerical simulation is the value of f_R which was used as a factor to account for the nonsphericity of the soot aggregates and was defined by Eq. (4.82). A value of f_R=3.7 was used throughout the flame. According to Eq. (4.82) this suggests an average number of primary particles per aggregate $N_p \approx 50$. The average value determined by the

thermophoretic method for particles corresponding to the annular region at a height z=15 mm, was N_p=34 which is in fair agreement with the value obtained numerically. However this expresses an average value and is not expected to describe accurately all the local values of N_p inside the flame. Howard, Wersborg and Williams[48,98] estimated that N_p≈10 for a low pressure premixed acetylene/oxygen flat flame. The higher number concentrations in our diffusion flame suggest higher agglomeration rates which imply a larger value of N_p.

Equation (4.34) of the bimodal solution was employed to calculate the surface area of the soot particles ultimately transported on r_c as a function of residence time. As shown in Figure 4.14A, during the time interval of intense particle inception, an increase of the surface area occurs which is related to the generation of a large population of fine particles. The soot surface area subsequently decreases because of strong coalescence between the particles. This decrease occurs only in the absence of surface growth which tends to increase surface area. After the onset of the surface growth mechanisms (the specific growth rate used is shown in Figure 4.14B) there is a strong competition of the two growth processes. The steady increase of the surface area, displayed by Figure 4.14A during that period, suggests the dominance of the surface growth term over the coagulation term. The subsequent cessation of the surface growth mechanisms triggers another stage of surface area decrease, associated with slower coagulation mechanisms as a result of the lower particle number concentrations. The above picture is not consistent with the observations of Harris and Weiner[38,39,41] for a premixed ethene/air flame under atmospheric pressure conditions. They reported an almost constant value of the soot surface area for three different stoichiometries. A series of assumptions employed by

both methods does not permit any conclusions about the reliability of the data, which refer to two flames of different nature.

The number concentration increase on either side of r_c, as determined by the optical method, was also investigated using the bimodal solution. As we mentioned previously, the annular region coincides with the location where the surface growth mechanisms display their maximum intensity. The surface growth reactions on both sides of the annular region ($r>r_c$ and $r<r_c$) can be substantially weaker as demonstrated by the acetylene production rate studies performed by Miller[68]. This behavior was modeled using the bimodal solution with no surface growth term. The rest of the variables were the ones used previously to describe the soot aerosol on the path line merging with r_c at $z=15$ mm. An important point was inferred from these calculations. Figure 4.15 shows the time variation of the particle number concentration and the particle size with and without the surface growth term. As we see the absence of surface growth reactions results in slower coagulation rates leading to higher number concentrations and smaller particle diameters. This numerical result illustrates that the number concentration anomaly, as determined by the optical measurements, may be a result of the weaker surface growth reactions occuring on both sides of the annular region.

CHAPTER 5

CONCLUSIONS AND RECOMMENDATIONS

A technique for extracting soot or other combustion generated (fumed) particulates from flames has been devised that affords a detailed examination of particle morphology and its regional variation within a flame environment. The technique is useful for gaining information on particle morphology that is not yielded by scattering and extinction measurements. The thermophoretic technique provides additional information for absorbing particles ($Q_{vv} \propto nv^2$, $K_{ext} \propto nv$), while for dielectric particles (Q_{vv} & $K_{ext} \propto nv^2$) the method is even more important. The method uses no assumption on the shape or the size distribution of the particles examined and provides additional information on the particle field which is necessary to reduce the data yielded by the optical experiments.

The method was used to study an overventilated coannular laminar ethene/air diffusion flame that releases no soot to the surroundings. The morphological features of the particles, examined by TEM for best image quality, provide not only valuable qualitative information on particle agglomeration, surface growth, and oxidation but also quantitative data on primary particle size as a function of flame coordinates. The technique proved to be rather unsuccessful in the lowest portion of the flame where particle inception occurs and where the reproducibility of the morphological data showed no consistency. Observations of soot samples collected from the low and intermediate portions of the flame consistently show an increasing primary size with height above the burner. This proves the dominance of surface growth reactions on the morphology of soot particles in the ethene flame

environment. The specific surface growth rate of particles transported on the annular region can be calculated throughout the intermediate regions of the flame without any approximations on the form of the particle size distribution, if particle velocity data are also available. A maximum growth rate of 10.5×10^{-5} g/cm^{2}s was measured occuring at an axial location z=15 mm above the burner mouth. The primary particle size was found to decrease as the particles move to the upper regions of the flame, probably through oxidative attack of various species.

Our studies further show that, at a specific axial location for intermediate heights in the flame, the primary particle size and the degree of agglomeration peak on the radius of maximum soot volume fraction ($r=r_c$). Both SEM and TEM observations show that the primary particle size and the state of agglomeration are substantially reduced on the air side of r_c, where particles smaller than 5 nm were detected throughout the interval $10<z<40$ mm. A similar trend is also present on the fuel side of r_c but the particle sizes there are not as small. However the observations corresponding to $r<r_c$ are less reliable since these regions are surrounded by an annulus of high soot concentration. The above observations led to the conclusion that the soot particles are formed locally in low regions of the flame near the reaction zone (maximum temperature region). This mechanism can account for the increase of the particle number concentration close to the reaction zone as determined by the optical measurements.

A comparison of the volume equivalent mean diameters obtained by the thermophoretic and the optical methods at a height z=15 mm above the burner mouth showed a fair agreement between the two techniques, thus

supporting the assumptions adopted by the optical tests for the data reduction at this height. The number of soot aggregates manually analyzed using an image analysis system proved to be inadequate to determine the form of the size distribution in a reliable manner.

The bimodal integral solution, used to model the soot formation processes in the ethene flame, provided additional information on the transpozt of particles along the path line merging with the annular region at a height z=15 mm. Our numerical simulations assumed incipient particles of 1.5 nm diameter generated by a Gaussian source pulse with a e^{-1} half width of 0.6 ms, creating a soot loading of the order of 10^{-8} cm^3/cm^3. A maximum particle inception rate of 10^{16} cm^{-3} s^{-1} was employed, a rate that is in agreement with the values reported previously for ethylene flames. The amount of soot generated during the particle inception stage was found to be negligible (0.2%) compared to that caused by surface growth reactions which accounts almost entirely for the bulk of soot ultimately formed. The value of the dimensionless second moment f_N was found to be higher during the particle inception stage and was almost constant during the interval of intense surface growth. Finally the soot surface area was found to increase during the surface growth stage which lasts throughout the low and intermediate regions of the flame.

Some recommendations on future directions of the current program are now suggested:

The investigation of the higher portions of the flame can provide valuable information on the soot oxidation rate in the ethene flame. The

potential of the method to obtain surface growth or oxidation rates has been proven and can be used to study the phenomena that trigger the release of soot to the environment under appropriate flow conditions.

Even though the soot field of the coannular ethene diffusion flame has been thoroughly investigated, though not completely understood, no extensive study of the chemical structure of the flame is available. Some previous attempts have given only limited amount of data proving the difficulty of such measurements. A mass spectrometric analysis of the basic species profiles would provide valuable information about the chemical steps leading to the formation, growth and depletion of soot throughout the flame.

In the theoretical model some improvements can be incorporated in the formulation of the collision term of the dynamic equation in order to account for the more complicated agglomeration mechanisms. An appropriate collision factor, modeling the nonspherical character of the soot aggregates, would obviously create a better description of the collision mechanisms of the particles inside the flame.

The thermophoretic sampling method can be used to provide soot morphological data related to other diffusion or premixed flames that have been already investigated optically and chemically. The combination of these techniques can contribute potentially to a detailed understanding of the soot formation processes in flames, which is far from our grasp at this time.

APPENDIX A

Numerical evaluation of the collision integrals

The collision integrals were defined by Eqs. (4.7). Assuming a log-normal form of the PVDF and using the following transformation

$$x_1 = \frac{\ln v/v_{g_i}}{3\sqrt{2}\,\sigma_{g_i}} \qquad (i = 1,2)$$

$$x_2 = \frac{\ln u/v_{g_i}}{3\sqrt{2}\,\sigma_{g_i}} \qquad (i = 1,2)$$

it can be shown that

$$Z_{fm_i}^{(0)} = -\frac{v_{g_i}^{1/6}}{\pi} \int_{-\infty}^{\infty}\int_{-\infty}^{\infty} G_i\left(x_1, x_2\right) \exp\left(-x_1^2 - x_2^2\right) dx_1\, dx_2 \qquad (A.1)$$

and

$$Z_{fm_i}^{(2)} = 2\,\frac{v_{g_i}^{13/6}}{\pi} \int_{-\infty}^{\infty}\int_{-\infty}^{\infty} f_i\left(x_1, x_2\right) G_i\left(x_1, x_2\right) \exp\left(-x_1^2 - x_2^2\right) dx_1\, dx_2 \qquad (A.2)$$

where $f_i\left(x_1, x_2\right) = \exp\left[3\sqrt{2}\,\sigma_{g_i}\left(x_1 + x_2\right)\right]$

$$G_i\left(x_1, x_2\right) = \left[\exp\left(\sqrt{2}\,\sigma_{g_i} x_1\right) + \exp\left(\sqrt{2}\,\sigma_{g_i} x_2\right)\right]^2$$

$$\left[\exp\left(-3\sqrt{2}\,\sigma_{g_i} x_1\right) + \exp\left(-3\sqrt{2}\,\sigma_{g_i} x_2\right)\right]^{1/2}$$

In order to express $Z_{fm_b}^{(k)}$ in the same form, define

$$y_1 = \frac{\ln u/v_{g_1}}{3\sqrt{2}\,\sigma_{g_1}}$$

$$y_2 = \frac{\ln v/v_{g_2}}{3\sqrt{2}\,\sigma_{g_2}}$$

Then

$$Z_{fm_b}^{(0)} = \frac{v_{g_1}^{1/6}}{\pi} \int_{-\infty}^{\infty}\int_{-\infty}^{\infty} G_b\left(y_1, y_2\right) \exp\left(-y_1^2 - y_2^2\right) dy_1\, dy_2 \qquad \text{(A.3)}$$

$$Z_{fm_b}^{(2)} = \frac{2}{\pi} v_{g_1}^{7/6}\, v_{g_2} \int_{-\infty}^{\infty}\int_{-\infty}^{\infty} f_b\left(y_1, y_2\right) G_b\left(y_1, y_2\right) \exp\left(-y_1^2 - y_2^2\right) dy_1\, dy_2 \qquad \text{(A.4)}$$

where

$$f_b\left(y_1, y_2\right) = \exp\left[3\sqrt{2}\left(\sigma_{g_1} y_1 + \sigma_{g_2} y_2\right)\right]$$

and

$$G_b\left[y_1, y_2\right] = \left[\left(\frac{v_{g_2}}{v_{g_1}}\right)^{1/3} \exp\left[\sqrt{2}\,\sigma_{g_2}\, y_2\right] + \exp\left[\sqrt{2}\,\sigma_{g_1}\, y_1\right]\right]^2$$

$$\left[\frac{v_{g_1}}{v_{g_2}} \exp\left[-3\sqrt{2}\,\sigma_{g_2}\, y_2\right] + \exp\left[-3\sqrt{2}\,\sigma_{g_1}\, y_1\right]\right]^{1/2}$$

As we see from (A.1) - (A.4) all collision integrals $Z_{fm_i}^{(k)}$; i = 1, 2, b and k = 0, 2 are of the general form

$$Z_{fm_i}^{(k)} = \int_{-\infty}^{\infty}\int_{-\infty}^{\infty} F_i(x, y) \exp\left[-x^2 - y^2\right] dx\, dy \qquad \text{(A.5)}$$

This form of integral can be readily evaluated using the Gauss-Hermite Quadrature (GHQ) rule[11,25] expressed by

$$\int_{-\infty}^{\infty} e^{-x^2} f(x)\, dx = \sum_{m=1}^{n} w_m f\left[x_m\right] \qquad \text{(A.6)}$$

where w_m: weight factors

x_m: zeros of Hermite polynomials

The values of w_m, x_m for $2 \leqslant n \leqslant 20$ are given in Table 2.14 of ref. 11. For high accuracy we chose n = 20.

Applying the GHQ rule on a double integral we can express (A.5) in a series form given by

$$Z_{fm_i}^{(k)} = \sum_{m=1}^{n} w_m \sum_{j=1}^{n} w_j \, F_i \left[x_m, y_j\right] \tag{A.7}$$

This formula was used to evaluate numerically the integrals $Z_{fm_i}^{(k)}$; i = 1, 2, b and k = 0, 2.

The values of $Z_{fm_i}^{(k)}$ (i = 1,2 and k = 0,2) can be closely approximated by interpolation formulae. Dobbins and Mulholland[23] found that in the range $0 \leqslant \sigma_{v_i} \leqslant 1.2$, $Z_{fm_i}^{(k)}$ can be approximated by

$$Z_{fm_i}^{(0)} = -4\sqrt{2} \; v_{g_i}^{1/6} \; \exp\left[\frac{3}{16} \sigma_{v_i}^{2}\right] \tag{A.8}$$

$$Z_{fm_i}^{(2)} = 8\sqrt{2} \; v_{g_i}^{13/6} \; \exp\left[\frac{65}{48} \sigma_{v_i}^{2}\right] \tag{A.9}$$

However the accuracy is not acceptable for values of $\sigma_{v_i} > 1.2$. For these values of σ_{v_i} we approximate $Z_{fm_i}^{(k)}$ by

$$Z_{fm_i}^{(0)} = -4\sqrt{2} \; v_{g_i}^{1/6} \; \exp\left[a_o + a_1 \sigma_{v_i}^{2} + a_2 \sigma_{v_i}^{4}\right] \; ; \quad i = 1,2 \tag{A.10}$$

$$Z_{fm_i}^{(2)} = 8\sqrt{2} \; v_{g_i}^{13/6} \; \exp\left[a_o' + a_1' \sigma_{v_i}^{2} + a_2' \sigma_{v_i}^{4}\right] \; ; \quad i = 1,2 \tag{A.11}$$

where

$$a_o = -8.346 \times 10^{-3}, \quad a_1 = 1.842 \times 10^{-1}, \quad a_2 = 7.267 \times 10^{-3}$$

and

$$a_o' = -2.255 \times 10^{-2}, \quad a_1' = 1.359, \quad a_2' = 6.306 \times 10^{-3}$$

These interpolation formulae provide good accuracy for high values of σ_{V_i} (see table A.1)

TABLE A.1

Comparison of Collision Integrals with Interpolation Formulae

		$-Z_{fm_i}^{(0)} \Big/ \left[4\sqrt{2}\, v_{g_i}^{1/6}\right]$		$Z_{fm_i}^{(2)} \Big/ \left[8\sqrt{2}\, v_{g_i}^{13/6}\right]$	
σ_{v_i}	$\sigma_{g_i} = \frac{\sigma_{v_i}}{3}$	GHQ*	Eq. (A.10)	GHQ	Eq. (A.11)
1.50	0.50	1.560	1.557	21.536	21.461
1.80	0.60	1.941	1.944	85.063	85.242
2.10	0.70	2.568	2.574	440.44	442.08
2.25	0.75	-	-	1,112.5	1,115.4
2.40	0.80	3.645	3.646	3,016.8	3,017.5
2.55	0.85	4.471	4.467	8,785.8	8,763.5
2.70	0.90	5.599	5.588	27,477	27,357
2.85	0.95	7.161	7.151	92,199	91,920
3.00	1.00	9.354	9.375	331,307	332,898

* Evaluated using the Gauss-Hermite Quadrature rule expressed by Eq. (A.7)

REFERENCES

1. ASTM:D3849-85. Standard test method for carbon black-primary aggregate dimensions from electron microscope image analysis. Annual Book of ASTM Standards.

2. Baumgärtner, L., Hesse, D., Jander, H., and Wagner, H. Gg. (1984). Rate of soot growth in atmospheric premixed laminar flames. Twentieth Symposium (International) on Combustion, The Combustion Institute, pp.959-967.

3. Bockhorn, H., Fetting, F., and Heddrich, A. (1986). Investigation of particle inception in sooting premixed hydrocarbon-oxygen low pressure flames. Twenty First Symposium (International) on Combustion, The Combustion Institute, in press.

4. Bockhorn, H., Fetting, F., Heddrich, A., and Wannemacher, G. (1984). Investigation of the surface growth of soot in flat low pressure hydrocarbon oxygen flames. Twentieth Symposium (International) on Combustion, The Combustion Institute, pp.979-988.

5. Bockhorn, H., Fetting, F., Meyer, U., Reck, R., and Wannemacher, G. (1981). Measurement of the soot concentration and soot particle sizes in propane oxygen flames. Eighteenth Symposium (International) on Combustion, The Combustion Institute, pp.1137-1147.

6. Bockhorn, H., Fetting, F., Wannemacher, G., and Wenz, H. W. (1982). Optical studies of soot particle growth in hydrocarbon oxygen flames. Nineteenth Symposium (International) on Combustion, The Combustion

Institute, pp.1413-1420.

7. Bockhorn, H., Fetting, F., and Wenz, H. W. (1983). Investigation of the formation of high molecular hydrocarbons and soot in premixed hydrocarbon-oxygen flames. Ber. Bunsenges. Phys. Chem. 87,1067.

8. Boedeker, L. R., and Dobbs, G. M. (1986). CARS temperature measurements in annular soot zones of axisymmetric laminar diffusion flames. Paper 36, Technical meeting, Eastern Section of the Combustion Institute, San Juan, Puerto Rico.

9. Burke, S. P., and Schumann, T. E. W. (1928). Diffusion flames. Industrial Engineering Chemistry 20,998.

10. Calcote, H. F. (1981). Mechanisms of soot nucleation in flames-A critical review. Combustion and Flame 42,215.

11. Carnahan, B., Luther, H. A., and Wilkes, J. O. (1969). *Applied Numerical Methods*, John Wiley & Sons, New York.

12. Chippett, S., and Gray, W. A. (1978). The size and optical properties of soot particles. Combustion and Flame 31,149.

13. Coe, D. S., Haynes, B. S., and Steinfeld, J. I. (1981). Identification of a source of argon-ion-laser excited fluorescence in sooting flames. Combustion and Flame 43,211.

14. D'Alessio, A. (1981). Laser light scattering and fluorescence diagnostics of rich flames produced by gaseous and liquid fuels. *Particulate Carbon Formation during Combustion*, D. C. Siegla and G. W. Smith (Eds.), Plenum Press, New York, p.207.

15. D'Alessio, A., Beretta, F., and Venitozzi, C. (1972). Optical investigations on soot forming methane-oxygen flames. Combustion Sci. and Technology 5,263.

16. D'Alessio, A., DiLorenzo, A., Borghese, A., Beretta, F., and Masi, S. (1977). Study of the soot nucleation zone of rich methane-oxygen flames. Sixteenth Symposium (International) on Combustion, The Combustion Institute, pp. 695-708.

17. D'Alessio, A., DiLorenzo, A., Sarofim, A. F., Beretta, F., Masi, S., and Venitozzi, C. (1975). Soot formation in methane-oxygen flames. Fifteenth Symposium (International) on Combustion, The Combustion Institute, pp.1427-1438.

18. Dannenberg, E. M. (1952). Carbon black dispersion and reinforcement. Industrial and Eng. Chemistry 44,813.

19. Dannenberg, E. M., Heckman, F. A., and Medalia, A. I. (1970). Structure and particle size of carbon black. Presented at the International Rubber Conference, Paris, France; Cabot Corporation research paper 57-88.

20. Dave, J. V. (1978). Subroutines for computing the parameter of the electromagnetic radiation scattered by a sphere. Report 320-3237, IBM, Palo Alto Scientific Center, Palo Alto CA.

21. Dobbins, R. A., and Megaridis, C. M. (1986). Soot morphological characteristics by means of thermophoretic sampling. Poster paper PS-009, Twenty First Symposium (International) on Combustion, The Combustion Institute, Munich, W. Germany.

22. Dobbins, R. A., and Megaridis, C. M. (1987). Morphology of flame-generated soot as determined by thermophoretic sampling. Langmuir 3, No. 2, 254.

23. Dobbins, R. A., and Mulholland, G. W. (1984). Interpretation of optical measurements of flame generated particles. Combustion Sci. and Technology 40,175.

24. Eisner, A. D., and Rosner, D. E. (1985). Experimental studies of soot particle thermophoresis in nonisothermal combustion gases using thermocouple response techniques. Combustion and Flame 61,153.

25. Ferziger, J. H. (1981). *Numerical Methods for Engineering Application*, John Wiley & Sons, New York.

26. Flower, W. L., and Bowman, C. T. (1984). Measurements of the structure of sooting laminar diffusion flames at elevated pressures. Twentieth Symposium (International) on Combustion, The Combustion Institute, pp.1035-1044.

27. Flower, W. L., and Bowman, C. T. (1986). Soot production in axisymmetric laminar diffusion flames at pressures from one to ten atmospheres. Twenty First Symposium (International) on Combustion, The Combustion Institute, in press.

28. Forsythe, G. E., Malcolm, M. A., and Moler, C. B. (1977). *Computer Methods for Mathematical Computations*, Prentice Hall, Englewood N.J.

29. Frenklach, M., and Harris, S. J. (1987). Aerosol dynamics modeling using the method of moments. J. Colloid and Interface Sci., in press.

30. Friedlander, S. K. (1977). *Smoke, Dust and Haze*, John Wiley & Sons, New York.

31. Friedlander, S. K., and Wang, C. S. (1966). The self-preserving particle size distribution for coagulation by Brownian motion. J. Colloid and Interface Sci. 22,126.

32. Gelbard, F. (1984). MAEROS: Computer program and algorithm review. Aerosol Sci. and Technology 3,117.

33. Gelbard, F., and Seinfeld, J. H. (1980). Simulation of multicomponent aerosol dynamics. J. Colloid and Interface Sci. 78, 485.

34. Glassman, I., and Yaccarino, P. (1981). The temperature effect in sooting diffusion flames. Eighteenth Symposium (International) on Combustion, The Combustion Institute, pp.1175-1183.

35. Goren, S. L. (1977). Thermophoresis of aerosol particles in the laminar boundary layer of a flat plate. J. Colloid and Interface Sci. 61,77.

36. Graham, S. C., and Homer, J. B. (1973). Coagulation of molten lead aerosols. Faraday Symposium Chem. Soc. 7,85.

37. Graham, S. C., and Robinson, A. (1976). A comparison of numerical solutions to the self-preserving size distribution for aerosol coagulation in the free-molecule regime. J. Aerosol Sci. 7,261.

38. Harris, S. J., and Weiner, A. M. (1983). Surface growth of soot particles in premixed ethylene/air flames. Combustion Sci. and Technology 31,155.

39. Harris, S. J., and Weiner, A. M. (1983). Determination of the rate constant for soot surface growth. Combustion Sci. and Technology 32,267.

40. Harris, S. J., and Weiner, A. M. (1984). Soot particle growth in premixed toluene/ethylene flames. Combustion Sci. and Technology 38,75.

41. Harris, S. J., and Weiner, A. M. (1985). Chemical kinetics of soot particle growth. Ann. Rev. Phys. Chem. 36,31.

42. Harris, S. J., Weiner, A. M., and Ashcraft, C. C. (1986). Soot particle inception kinetics in a premixed ethylene flame. Combustion and Flame 64,65.

43. Haynes, B. S., Jander, H., and Wagner, H. Gg. (1980). Optical studies of soot-formation processes in premixed flames. Ber. Bunsenges. Phys. Chem. 84,585.

44. Haynes, B. S., and Wagner, H. Gg. (1980). Sooting structure in a laminar diffusion flame. Ber. Bunsenges. Phys. Chem. 84,499.

45. Haynes, B. S., and Wagner, H. Gg. (1981). Soot formation. Prog. Energy Combust. Sci. 7,229.

46. Hess, W. M., Ban, L. L., and McDonald, G. C. (1969). Carbon black morphology: I. Particle microstructure. II. Automated EM analysis of aggregate size and shape. Rubber Chem. and Technology 42,1209.

47. Homann, K. H., and Wagner, H. Gg. (1967). Some new aspects of the mechanism of carbon formation in premixed flames. Eleventh Symposium (International) on Combustion, The Combustion Institute, pp.371-379.

48. Howard, J. B., Wersborg, B. L., and Williams, G. C. (1973). Coagulation of carbon particles in premixed flames. Faraday Symposium Chem. Soc. 7,109.

49. Jacoda, I. J., Prado, G., and Lahaye, J. (1980). An experimental investigation into soot formation and distribution in polymer diffusion flames. Combustion and Flame 37,261.

50. JANAF Thermochemical Tables (1970). U. S. Government Printing Office, Sec. Edition, NSRDS-NBS37.

51. Kent, J. H., Jander, H., and Wagner, H. Gg. (1981). Soot formation in a laminar diffusion flame. Eighteenth Symposium (International) on Combustion, The Combustion Institute, pp.1117-1126.

52. Kent, J. H., and Wagner, H. Gg. (1982). Soot measurements in laminar ethylene diffusion flames. Combustion and Flame 47,53.

53. Kent, J. H., and Wagner, H. Gg. (1984). Why do diffusion flames emit smoke? Combustion Sci. and Technology 41,245.

54. Kunugi, M., and Jinno, H. (1967). Determination of size and concentration of soot particles in diffusion flames by a light-scattering technique. Eleventh Symposium (International) on Combustion, The Combustion Institute, pp.257-266.

55. Lahaye, J., and Prado, G. (1978). Mechanisms of carbon black formation. *Chemistry and Physics of Carbon*, P. L. Walker, Jr. and P. A. Thrower (Eds.), Marcel Dekker, New York, vol.14, p.167.

56. Lahaye, J., Prado, G., and Donnet, J. B. (1974). Nucleation and growth of carbon black particles during thermal decomposition of benzene. Carbon 12,27.

57. Lai, F. S., Friedlander, S. K., Pich, J., and Hidy, G. M. (1972). The self-preserving particle size distribution for Brownian coagulation in the free molecular regime. J. Colloid and Interface Sci. 39,395.

58. Lee, K. W. (1983). Change of particle size distribution during Brownian coagulation. J. Colloid and Interface Sci. 92,315.

59. Lee, K. W., and Chen, H. (1984). Coagulation rate of polydisperse particles. Aerosol Sci. and Technology 3,327.

60. Lee, K. W., Chen, H., and Gieseke, J. A. (1984). Log-normally preserving size distribution for Brownian coagulation in the free-molecule regime. Aerosol Sci. and Technology 3,53.

61. Medalia, A. I. (1967). Morphology of aggregates- I. Calculation of shape and bulkiness factors. Application to computer-simulated random flocs. J. Colloid and Interface Sci. 24,393.

62. Medalia, A. I. (1970). Morphology of aggregates- VI. Effective volume of aggregates of carbon black from electron microscopy; Application to vehicle absorption and to die swell of filled rubber. J. Colloid and Interface Sci. 32, No.1, 115.

63. Medalia, A. I. and Heckman, F.A. (1971). Morphology of aggregates- VII. Comparison chart method for electron microscopic determination of carbon black aggregate morphology. J. Colloid and Interface Sci. 36, No.2, 173.

64. Medalia, A. I., Dannenberg, E. M., Heckman, F. A., and Cotten, G. R. (1973). Characterization of new technology carbon blacks. Rubber Chem. and Technology 46, No.5, 1239.

65. Medalia, A. I., and Heckman, F. A. (1969). Morphology of aggregates-II. Size and shape factors of carbon black aggregates from electron microscopy. Carbon 7,567.

66. Medalia, A. I., Heckman, F. A., and Harling, D. F. (1969). Morphology of aggregates- IV. Particle size and structure of carbon black from electron micrographs. J. Rubber Res. Inst. Malaya 22,381.

67. Medalia, A. I., and Richards, L. W. (1972). Tinting strength of carbon black. J. Colloid and Interface Sci. 40, No.2, 233.

68. Miller, J. H. (1986). The chemical structure of an atmospheric pressure ethylene/air diffusion flame: Preliminary results. Paper 33, Technical meeting, Eastern Section of the Combustion Institute, San Juan, Puerto Rico.

69. Miller, J. H., Mallard, W. G., and Smyth, K. C. (1982). The observation of laser-induced visible fluorescence in sooting diffusion flames. Combustion and Flame 47,205.

70. Miller, J. H., Mallard, W. G., and Smyth, K. C. (1986). Chemical production rates of intermediate hydrocarbons in a methane/air diffusion flame. Twenty First Symposium (International) on Combustion, The Combustion Institute, in press.

71. Millikan, R. C. (1962). Sizes, optical properties, and temperatures of soot particles. *Temperature, Its Measurement and Control in Science and*

Industry, Vol.3, part 2, Reinhold, New York, 497.

72. Mitchell, R. E., Sarofim, A. F., and Clomburg, L. A. (1980). Experimental and numerical investigation of confined laminar diffusion flames. Combustion and Flame 37,227.

73. Mulholland, G. W., Mountain, R. D., and Baum, H. (1986). Simulation of aerosol agglomeration in the free molecular and continuum flow regimes. NBSIR 86-3342.

74. Neoh, K. G., Howard, J. B., and Sarofim, A. F. (1984). Effect of oxidation on the physical structure of soot. Twentieth Symposium (International) on Combustion, The Combustion Institute, pp.951-957.

75. Prado, G., Garo, A., Ko, A., and Sarofim, A. (1984). Polycyclic aromatic hydrocarbons. Formation and destruction in a laminar diffusion flame. Twentieth Symposium (International) on Combustion, The Combustion Institute, pp.989-996.

76. Prado, G. Jacoda, J., Neoh, K., and Lahaye, J. (1981). A study of soot formation in premixed propane/oxygen flames by in-situ optical techniques and sampling probes. Eighteenth Symposium (International) on Combustion, The Combustion Institute, pp.1127-1136.

77. Prado, G., and Lahaye, J. (1981). Physical aspects of nucleation and growth of soot particles. *Particulate Carbon Formation during Combustion*, D. C. Siegla and G. W. Smith (Eds.), Plenum Press, New York, p.143.

78. Prado, G. P., Lee, M. L., Hites, R. A., Hoult, D. P., and Howard, J. B. (1977). Soot and hydrocarbon formation in a turbulent diffusion flame.

Sixteenth Symposium (International) on Combustion, The Combustion Institute, pp.649-661.

79. Rosner, D. E. (1985). Mass transfer across combustion gas thermal boundary layers-Power production and materials processing implications. Invited lecture, 23rd ASME/AIChE National Heat Transfer Conference, Denver CO.

80. Saito, K., Williams, F. A., and Gordon, A. S. (1986). A study of the two-color soot zone for small hydrocarbon diffusion flames. Combustion Sci. and Technology, in press.

81. Santoro, R. J. (1984). Personal communication.

82. Santoro, R. J., and Miller, J. H. (1987). Soot particle formation in laminar diffusion flames. Langmuir 3, No. 2, 244.

83. Santoro, R. J., and Semerjian, H. G. (1984). Soot formation in diffusion flames: Flow rate, fuel species and temperature effects. Twentieth Symposium (International) on Combustion, The Combustion Institute, pp. 997-1006.

84. Santoro, R. J., Semerjian, H. G., and Dobbins, R. A. (1983). Interpretation of optical measurements of soot in flames. AIAA Eighteenth Thermophysics Conference, Montreal, Canada.

85. Santoro, R. J., Semerjian, H. G., and Dobbins, R. A. (1983). Soot particle measurements in diffusion flames. Combustion and Flame 51,203.

86. Santoro, R. J., Yeh, T. T., and Semerjian, H. G. (1985). The transport and growth of soot particles in laminar diffusion flames. 23rd ASME/AIChE National Heat Transfer Conference, Denver CO.

87. Seigneur, C., Hudischewskyj, A. B., Seinfeld, J. H., Whitby, K. T., Whitby, E. R., Brock, J. R., and Barnes, H. M. (1986). Simulation of aerosol dynamics: A comparative review of mathematical models. Aerosol Sci. and Technology 5,205.

88. Skolnik, E. G., and McHale, E. T. (1980). Sampling of soot in diffusion flames. Combustion and flame 37,327.

89. Smyth, K. C., and Miller, J. H. (1986). Soot inception in hydrocarbon diffusion flames. Invited paper C, Technical Meeting, Eastern Section, The Combustion Institute, San Juan, Puerto Rico.

90. Smyth, K. C., Miller, J. H., Dorfman, R. C., Mallard, W. G., and Santoro, R. J. (1985). Soot inception in a methane/air diffusion flame as characterized by detailed species profiles. Combustion and Flame 62,157.

91. Svehla, R. A. (1962). Estimated viscosities and thermal conductivities of gases at high temperatures. NASA Technical Report R-132.

92. Talbot, L., Cheng, R. K., Schefer, R. W., and Willis, D. R. (1980). Thermophoresis of particles in a heated boundary layer. J. of Fluid Mechanics 101,737.

93. Tesner, P. A. (1959). Formation of dispersed carbon by thermal decomposition of hydrocarbons. Seventh Symposium (International) on Combustion, The Combustion Institute, pp.546-553.

94. Tesner, P. A. (1973). Formation of soot particles. Faraday Symposium Chem. Soc. 7,104.

95. Tesner, P. A., Snegiriova, T. D., and Knorre, V. G. (1971). Kinetics of dispersed carbon formation. Combustion and Flame 17,253.

96. Wagner, H. Gg. (1981). Soot formation-An overview. *Particulate Carbon Formation during Combustion*, D. C. Siegla and G. W. Smith (Eds.), Plenum Press, New York, p.1.

97. Warren, D. R., and Seinfeld, J. H. (1985). Simulation of aerosol size distribution in systems with simultaneous nucleation, condensation and coagulation. Aerosol Sci. and Technology 4,31.

98. Wersborg, B. L., Howard, J. B., and Williams, G. C. (1973). Physical mechanisms in carbon formation in flames. Fourteenth Symposium (International) on Combustion, The Combustion Institute, pp. 929-940.

99. Whitby, K. T. (1981). Determination of aerosol growth rates in the atmosphere using lumped mode aerosol dynamics. J. Aerosol Sci. 12,173.

100. Wolfhard, H. G., and Parker, W. G. (1949). A new technique for the spectroscopic examination of flames at normal pressures. Proc. Phys. Soc., London, Sect. A, 62,722.

101. Wolfhard, H. G., and Parker, W. G. (1952). A spectroscopic investigation into the structure of diffusion flames. Proc. Phys. Soc., London, Sect. A, 65,2.

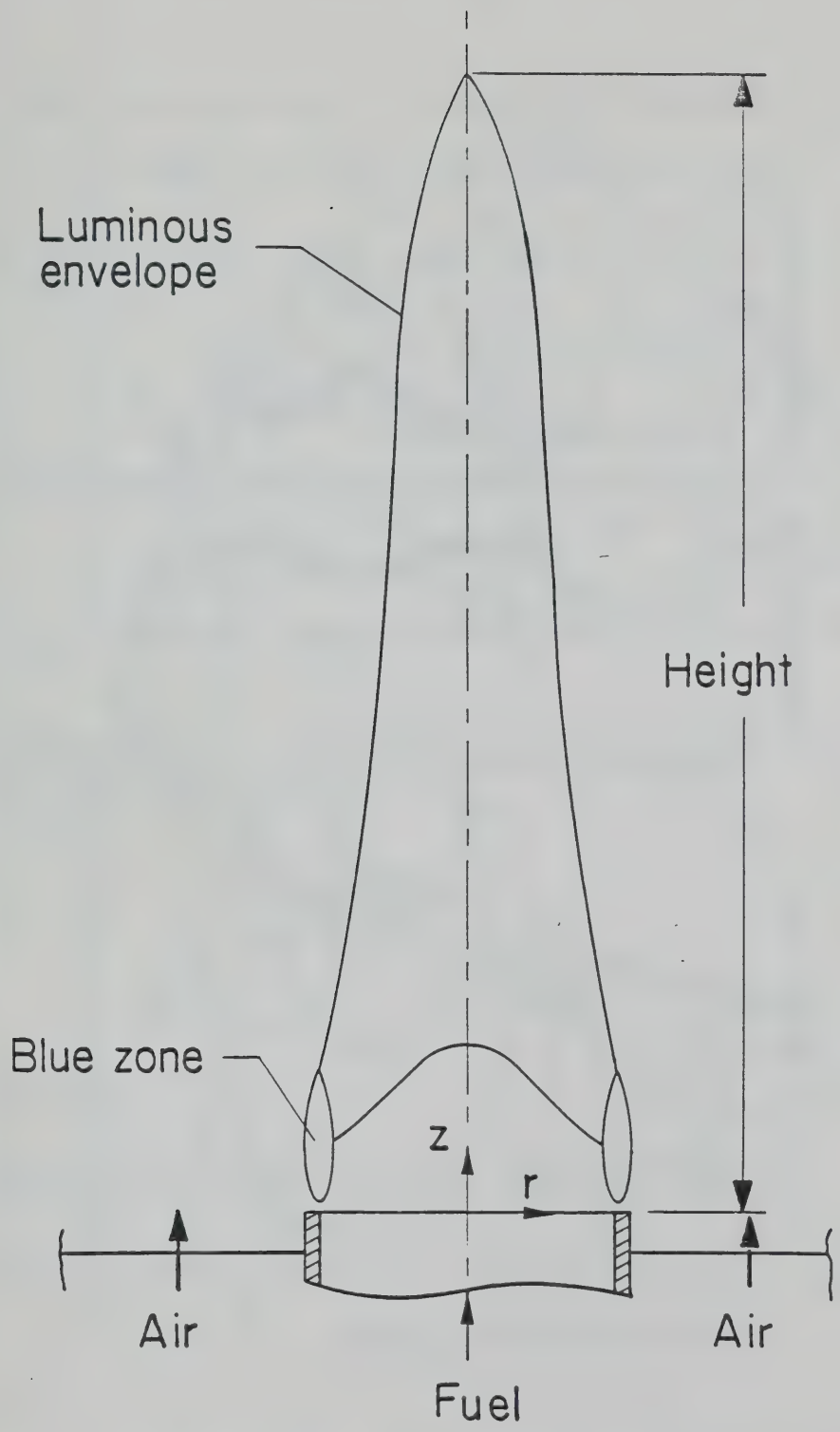

Figure 2.1 Typical structure of a nonsmoking coannular laminar diffusion flame.

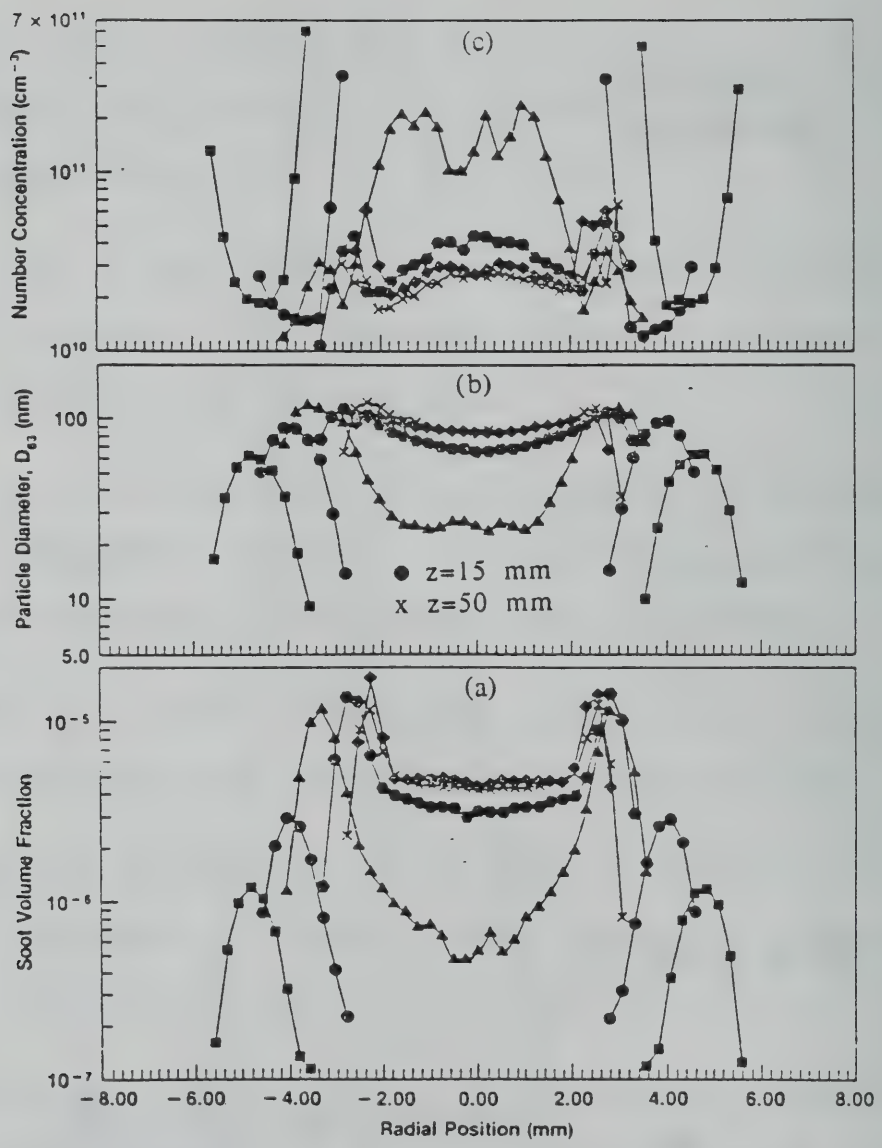

Figure 2.2 (a) Soot volume fraction, (b) particle diameter, and (c) number concentration as a function of z and r for the ethene diffusion flame. Reproduced from ref. 85.

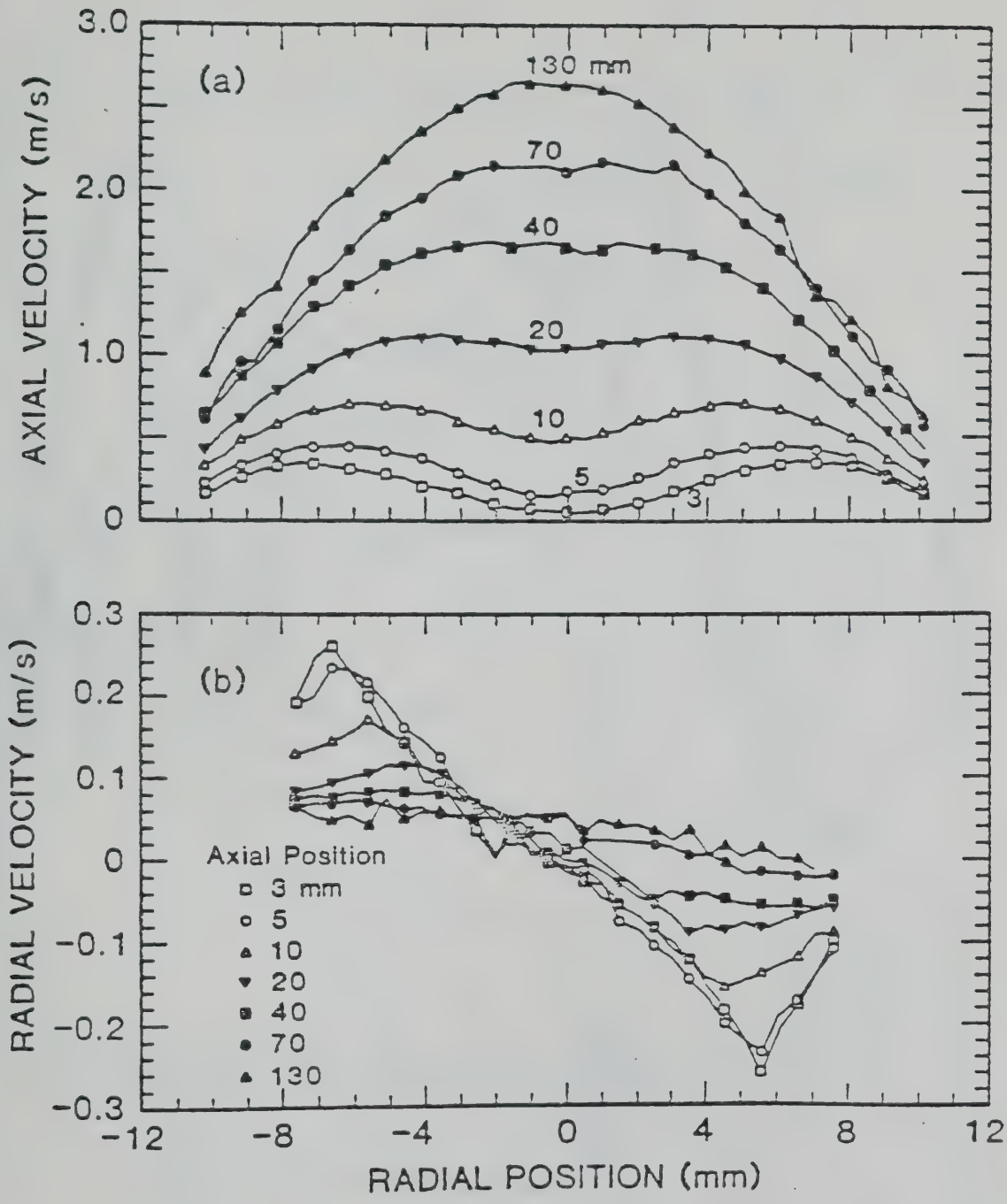

Figure 2.3 Velocity profiles in the ethene diffusion flame; (a) axial velocity component, (b) radial velocity component. Reproduced from ref. 86.

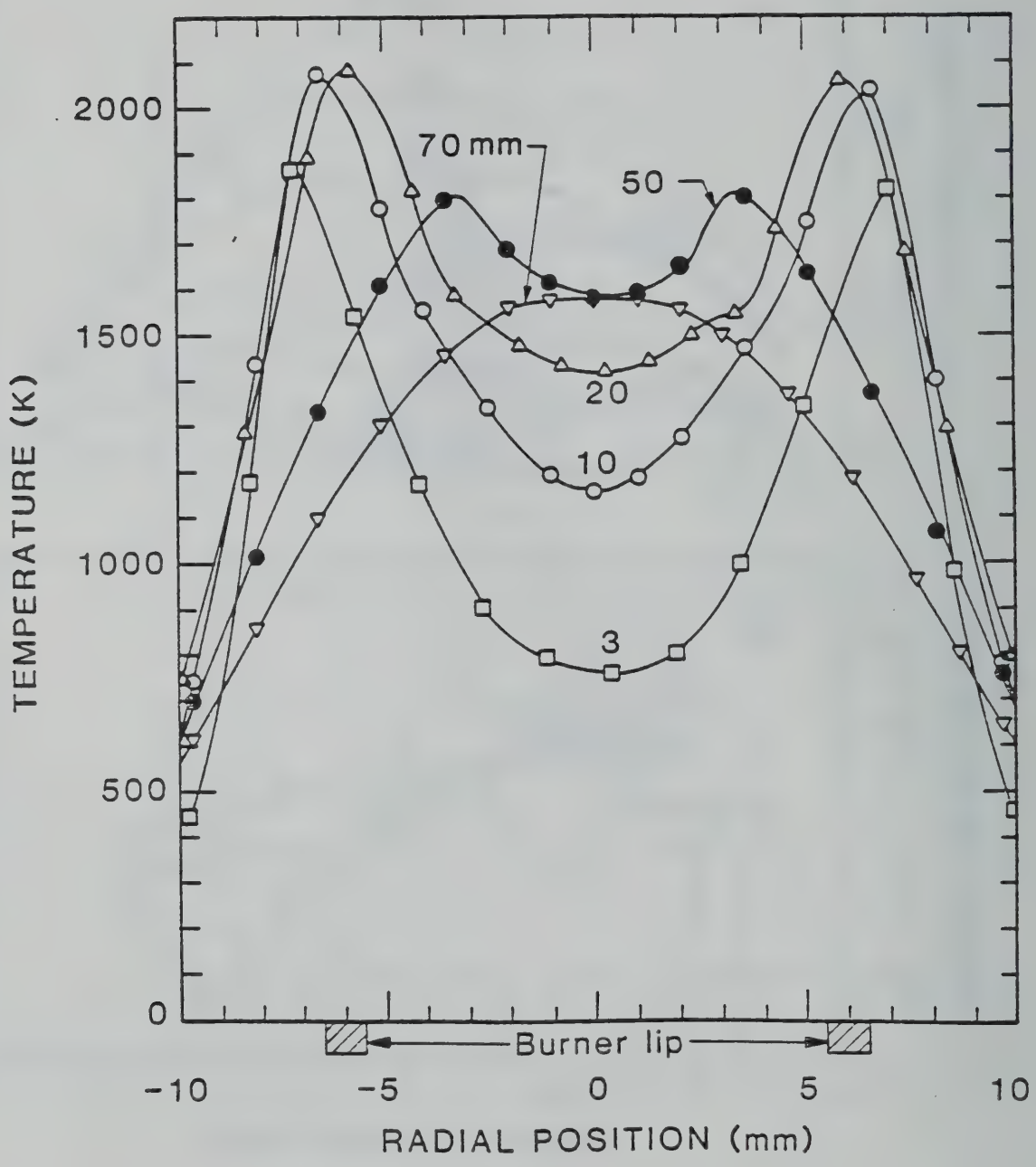

Figure 2.4 Temperature profiles in the ethene diffusion flame at various axial locations z (uncorrected thermocouple measurements). Reproduced from ref. 82.

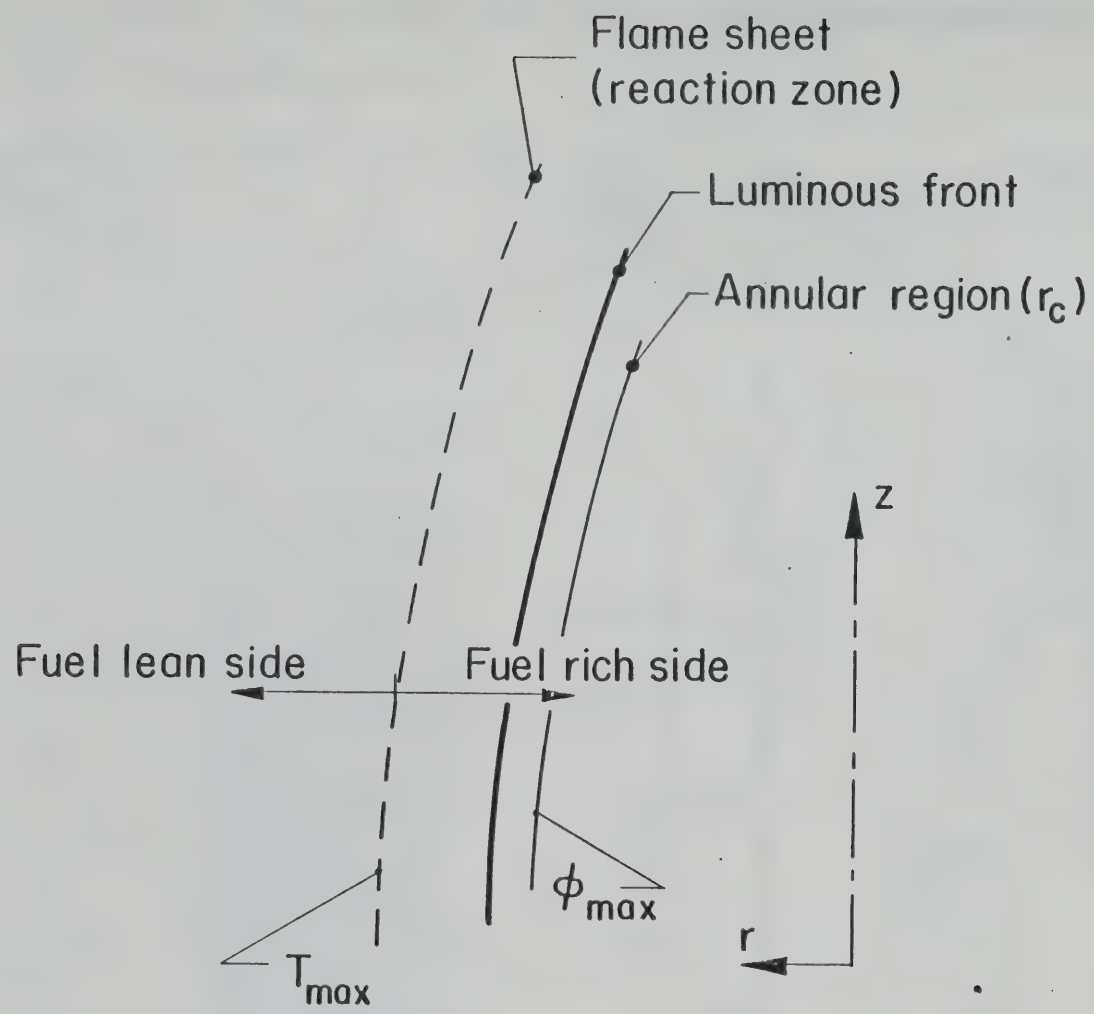

Figure 2.5 Flame front structure of a coannular laminar diffusion flame. The coordinate system is also displayed.

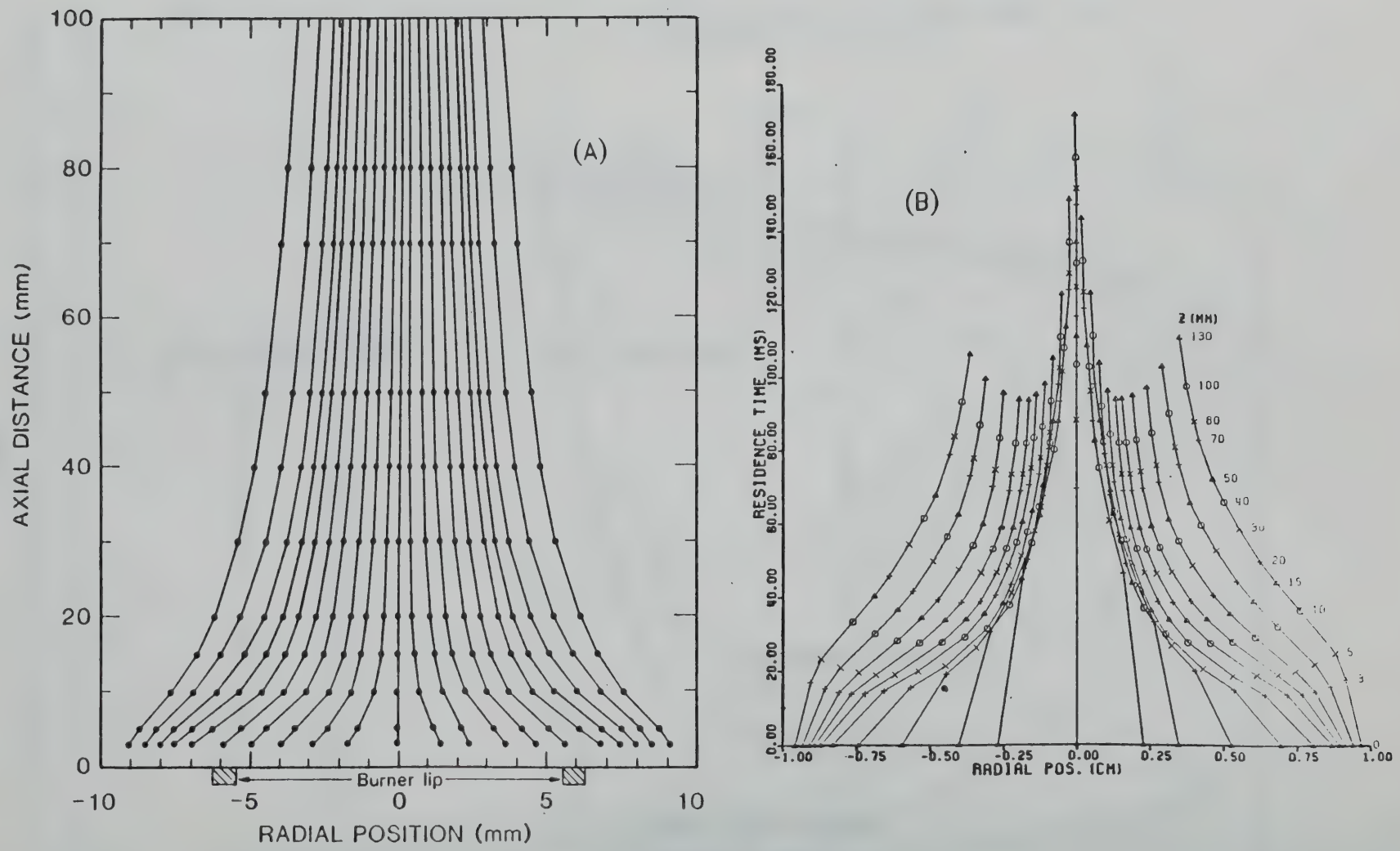

Figure 2.6 (A) Particle paths, and (B) residense times, calculated from the velocity measurements for the ethene diffusion flame. Reproduced from refs. 86 and 81 respectively.

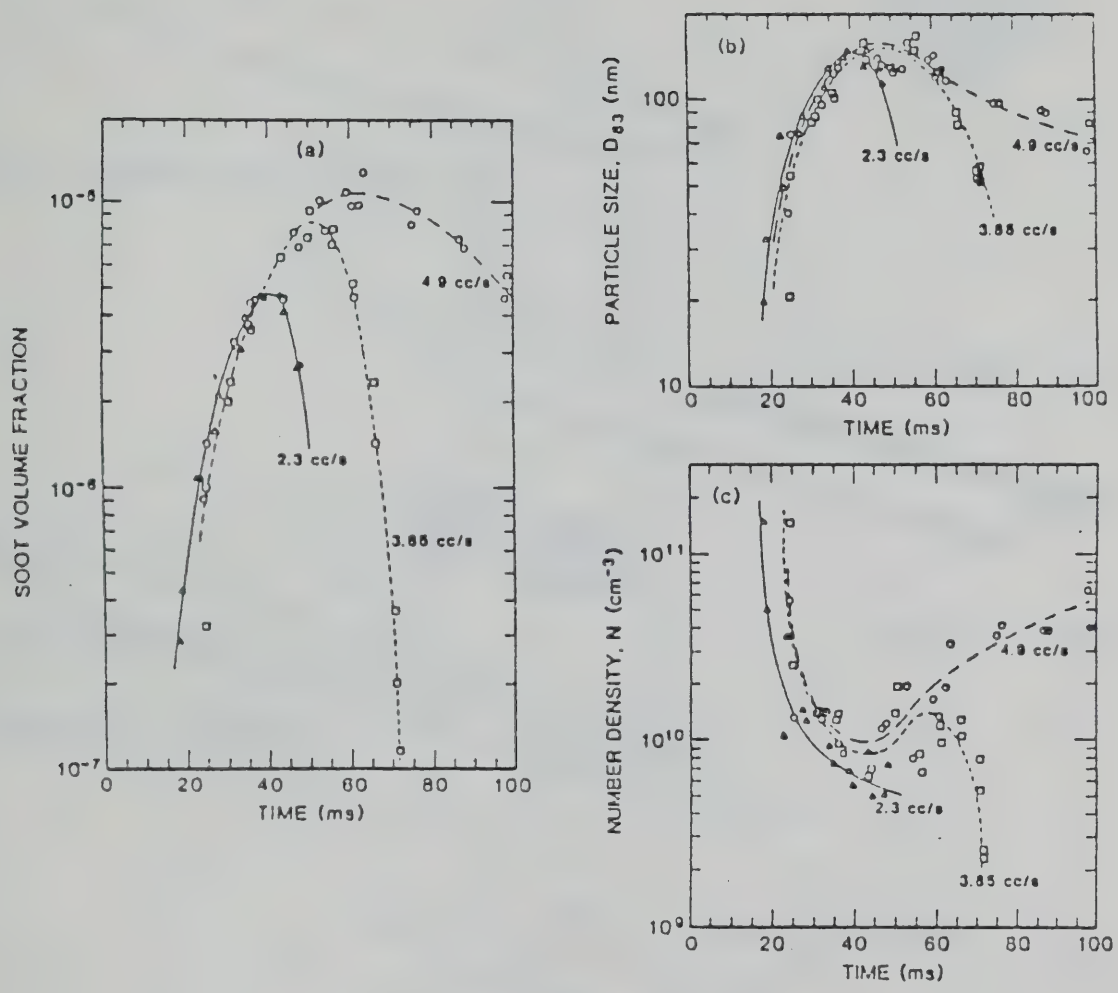

Figure 2.7 (a) Soot volume fraction, (b) particle diameter, and (c) number concentration along the line exhibiting the maximum volume fraction value. Only the curves labeled 3.85 cc/s are related to the ethene diffusion flame under investigation. Reproduced from ref. 86.

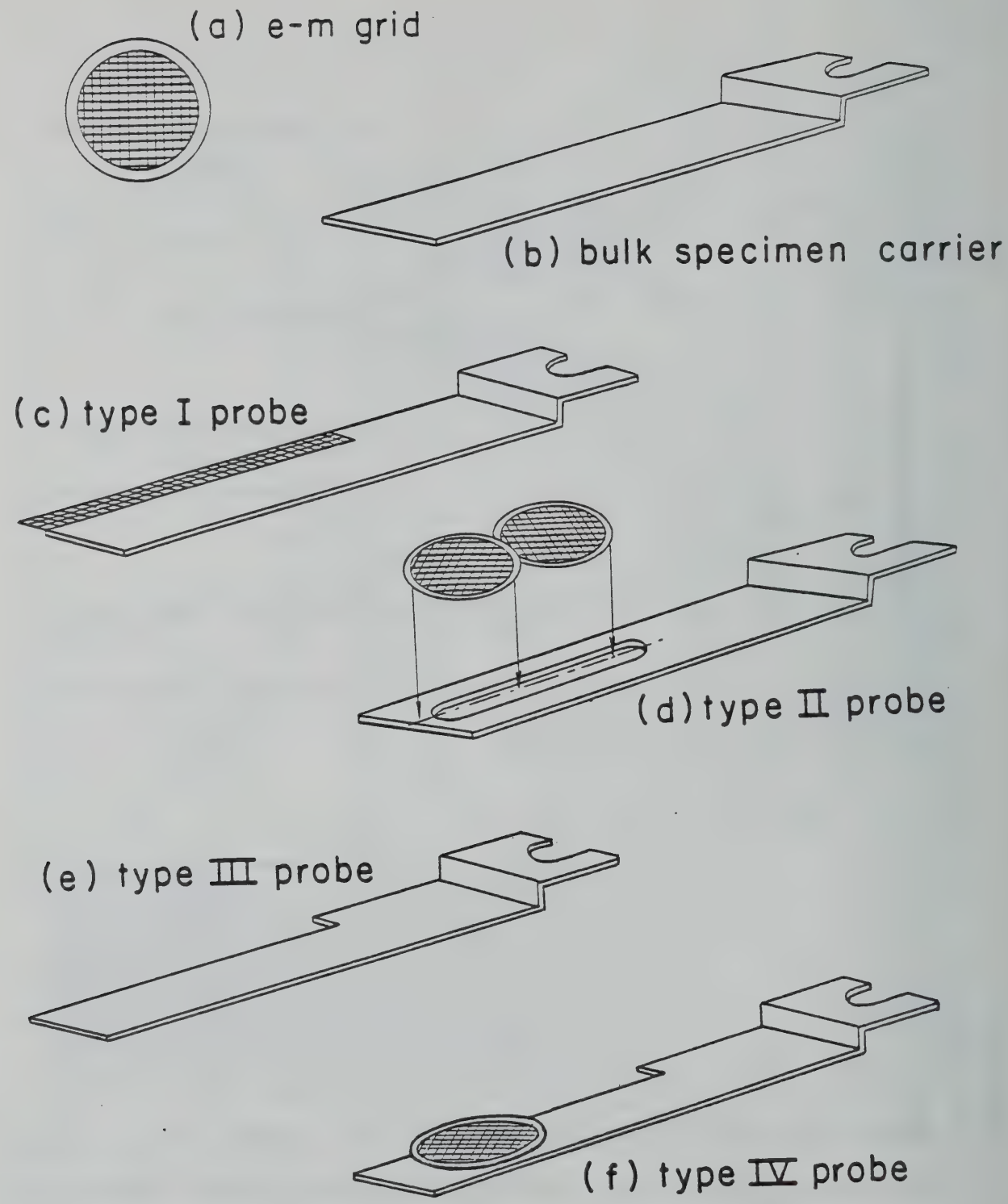

Figure 3.1 Sketch of thermophoretic probe devices; (a) circular grid, (b) bulk specimen carrier, (c)-(f) modified probes.

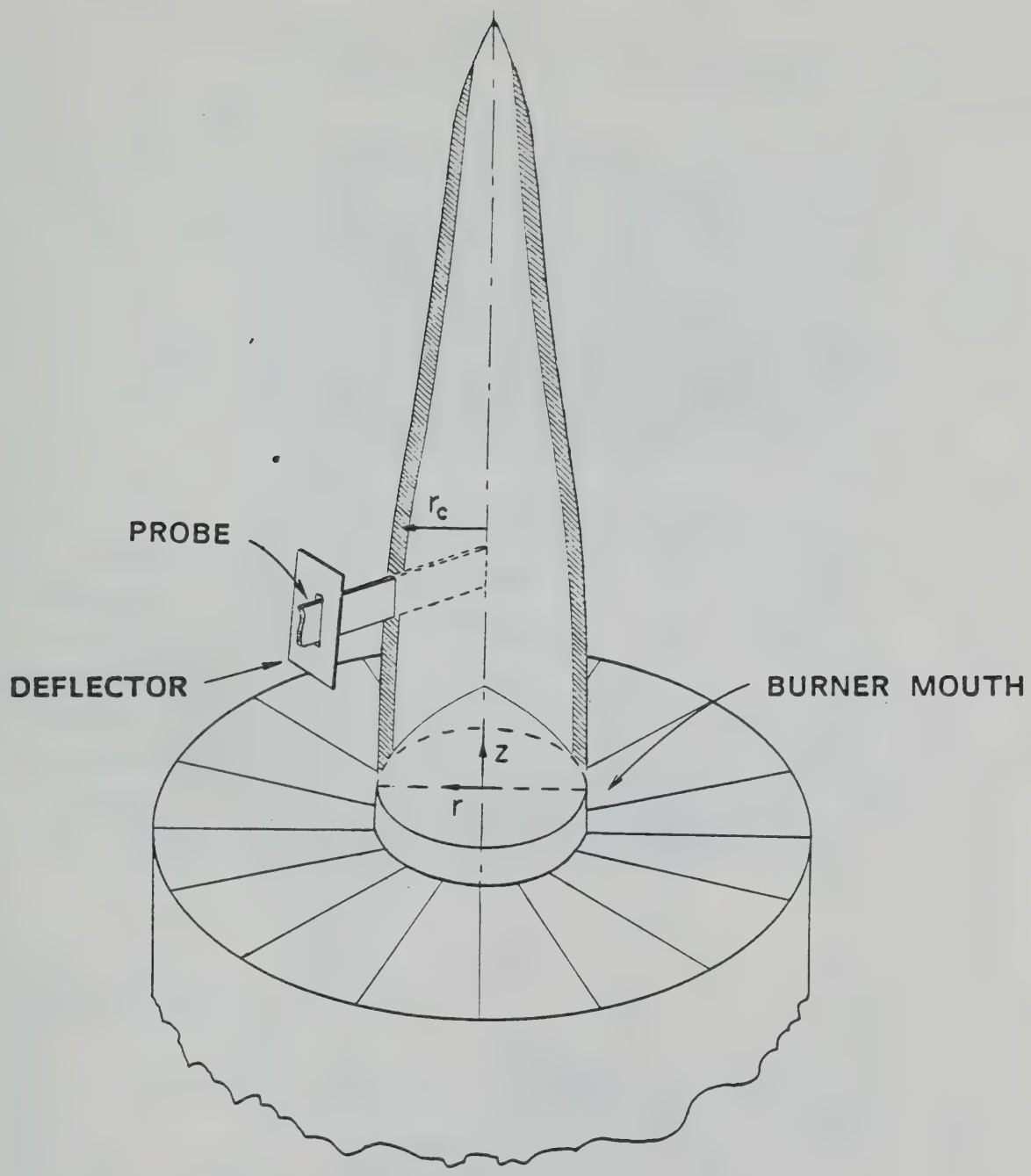

Figure 3.2 Sketch of thermophoretic probe sampling of a coannular diffusion flame. The flame coordinate system and the radial position r_c of maximum soot volume fraction are also shown.

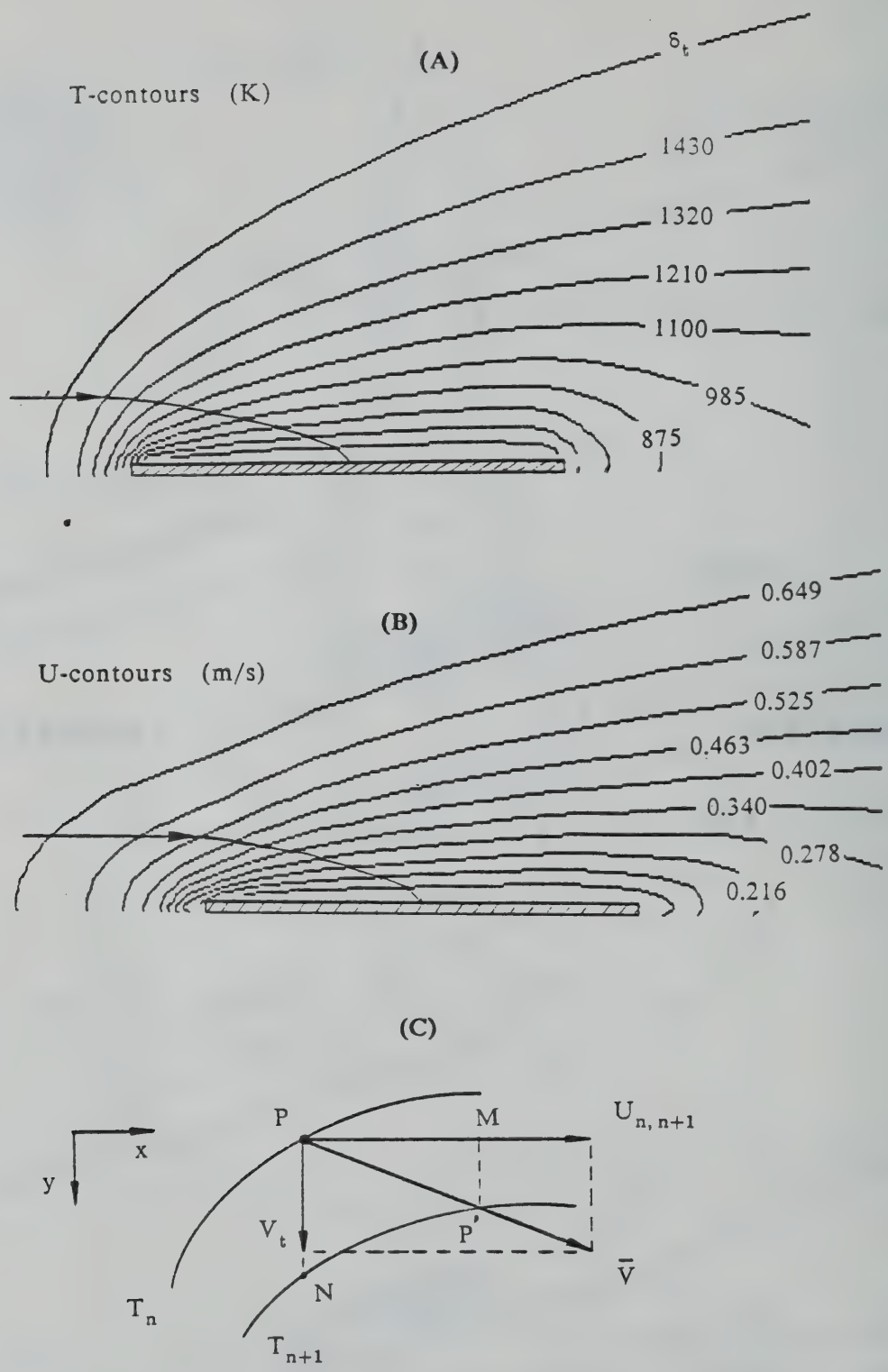

Figure 3.3 (A) Numerically calculated temperature contours, and (B) velocity contours of the flow field around the probe. The thermal boundary layer δ_t, and the trajectory of a soot particle ultimately captured halfway along the probe are also shown. (C) Schematic of a particle P traversing the distance between two neighboring isotherms.

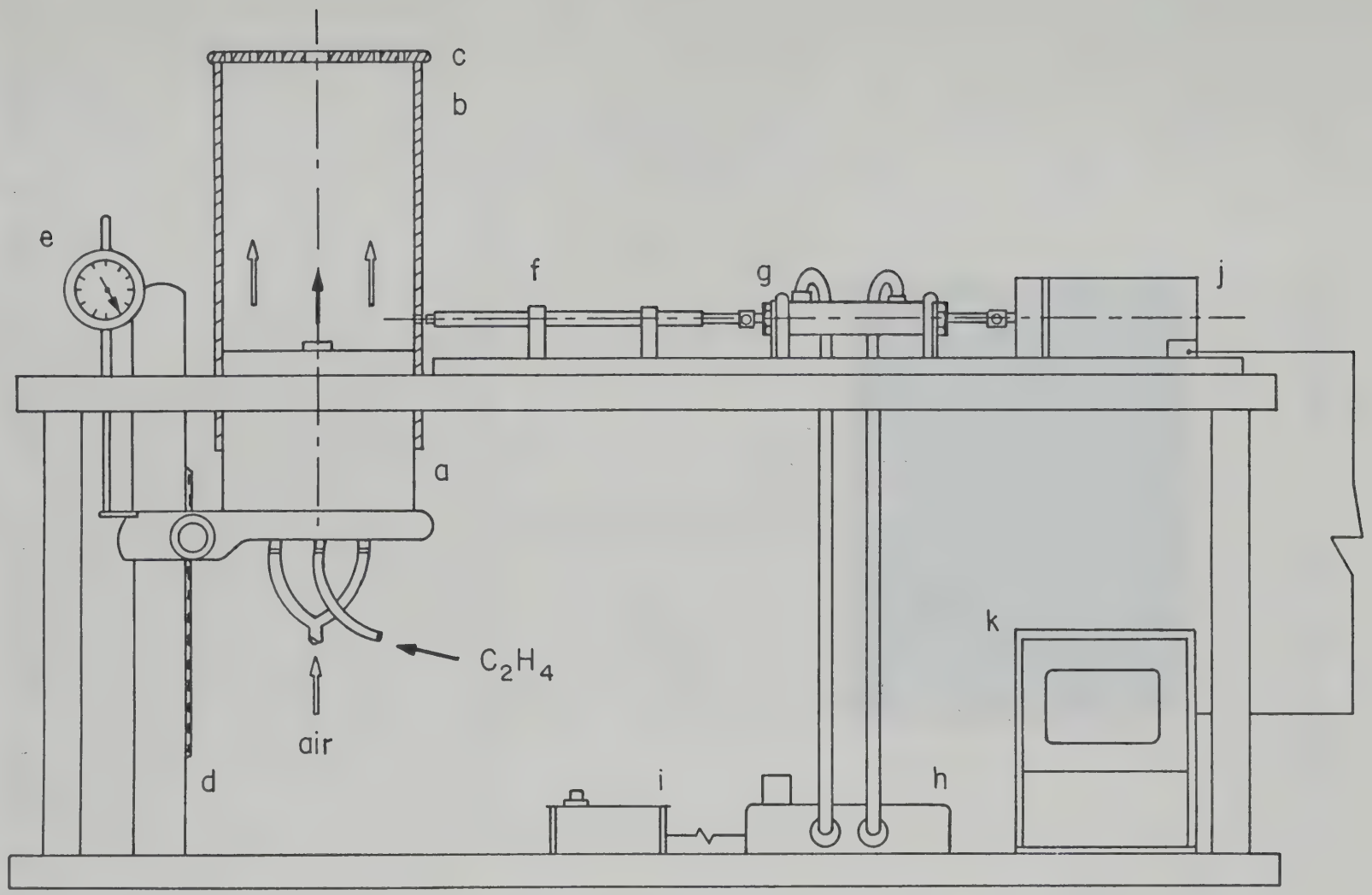

Figure 3.4 Schematic diagram of the probe control system and related equipment.

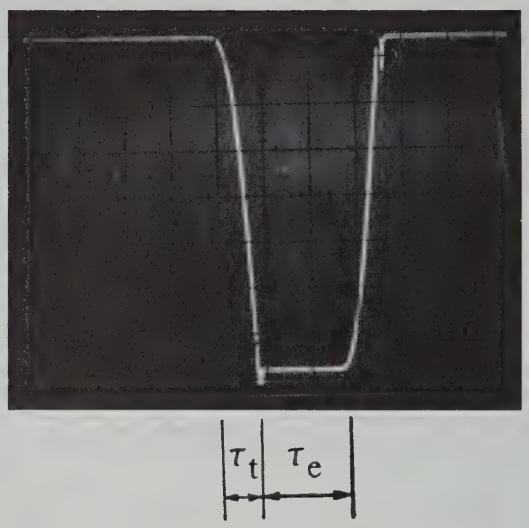

Figure 3.5 Typical oscilloscope record of the probe trajectory. Transit time $\tau_t \simeq 16$ ms, exposure (residence) time $\tau_e \simeq 36$ ms.

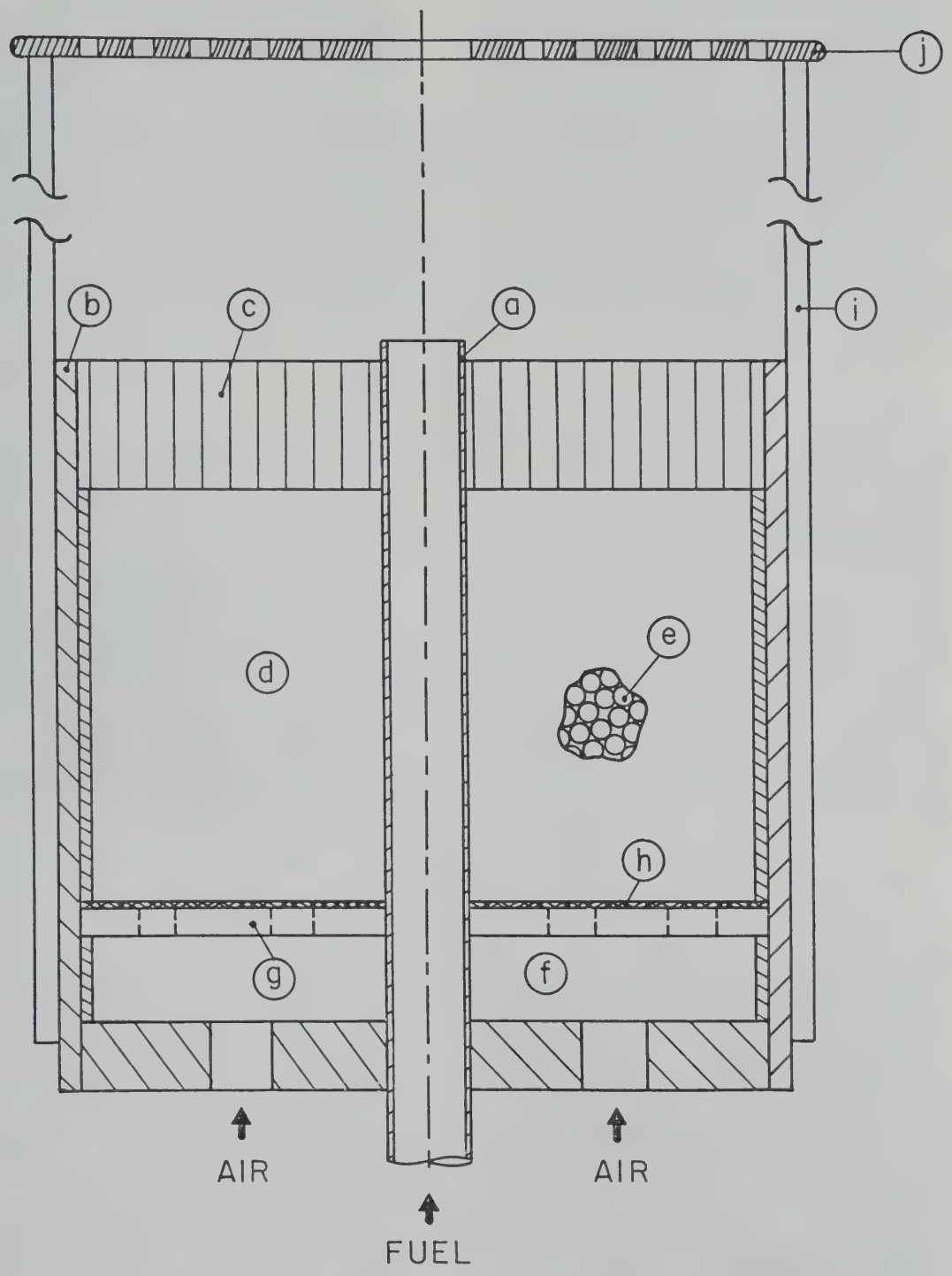

Figure 3.6 Cross sectional drawing of the coannular burner.

Figure 3.7 TEM micrograph of soot particles deposited on a carbon substrate supported by a copper grid positioned at z=30 mm. The grid bar is shown as the dark boundary. Grid exposure time τ_e≈30 ms.

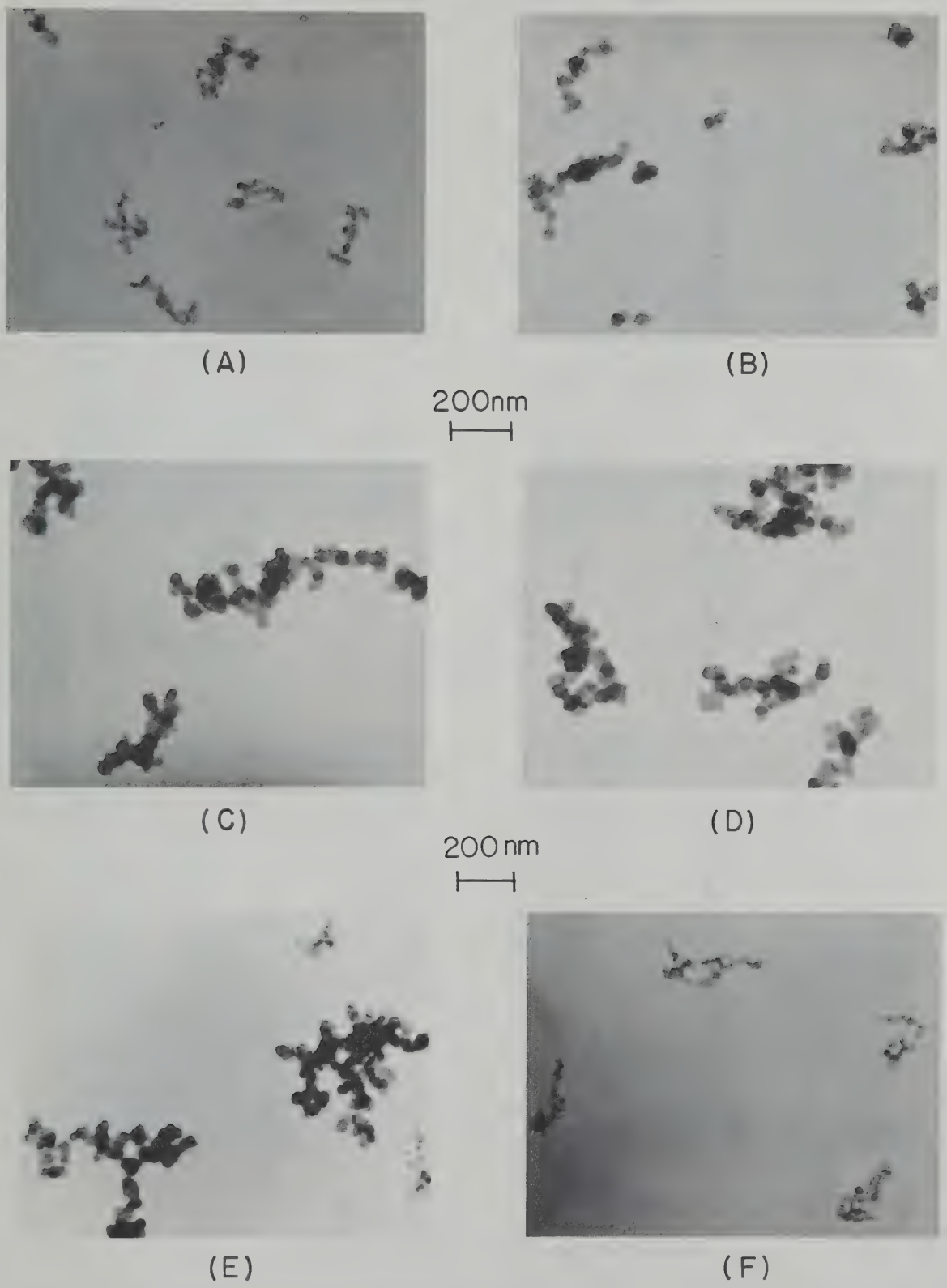

Figure 3.8 TEM micrographs of soot particles collected from the annular region of the ethene diffusion flame at various heights z, using carbon coated grids. For all cases $\tau_e \approx 30$ ms except (A) where $\tau_e \approx 120$ ms. (A) z=10 mm, (B) z=20 mm, (C) z=30 mm, (D) z=40 mm, (E) z=50 mm, (F) z=80 mm.

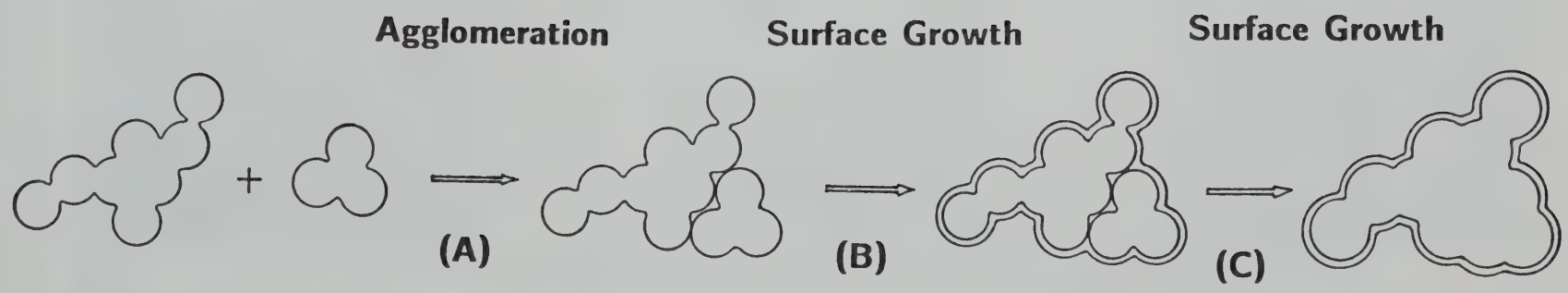

Figure 3.9 Mechanisms of soot particle growth.

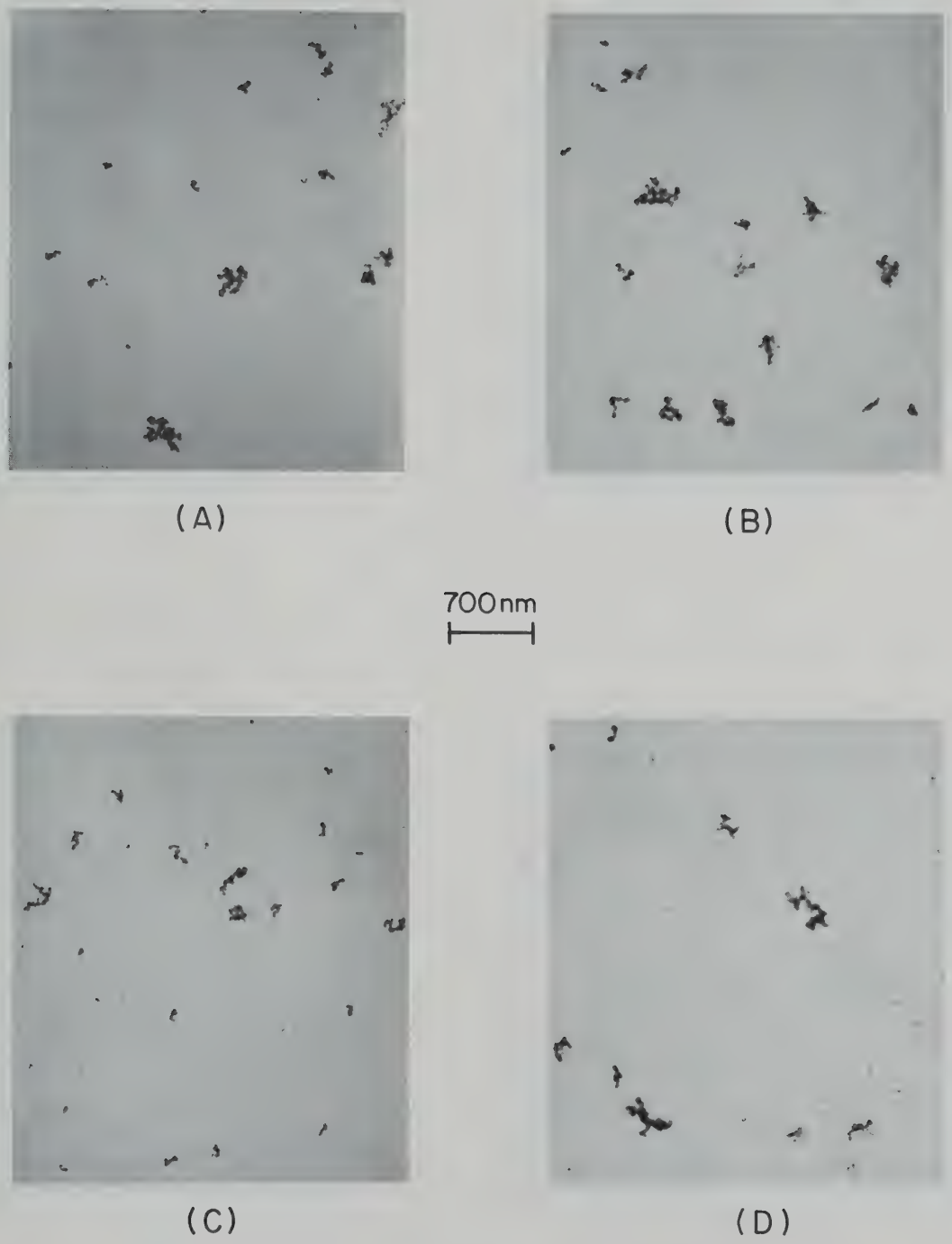

Figure 3.10 TEM micrographs of soot particles collected from the annular region of the ethene diffusion flame at a height z=20 mm, using carbon coated grids. (A) $\tau_e \simeq 30$ ms, (B) $\tau_e \simeq 50$ ms, (C) $\tau_e \simeq 70$ ms, (D) $\tau_e \simeq 90$ ms.

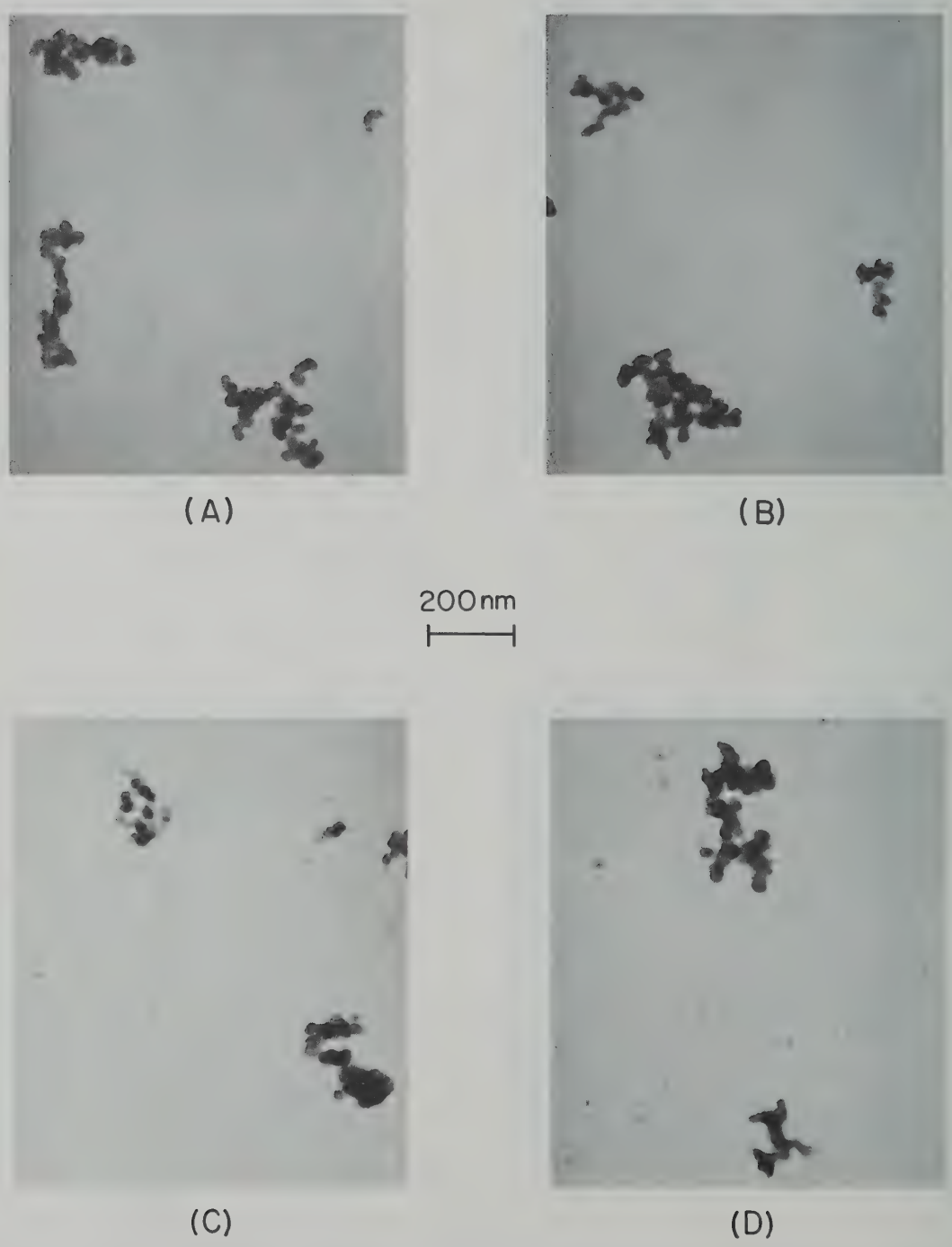

Figure 3.11 High magnification TEM micrographs of the particles described in Figure 3.10.

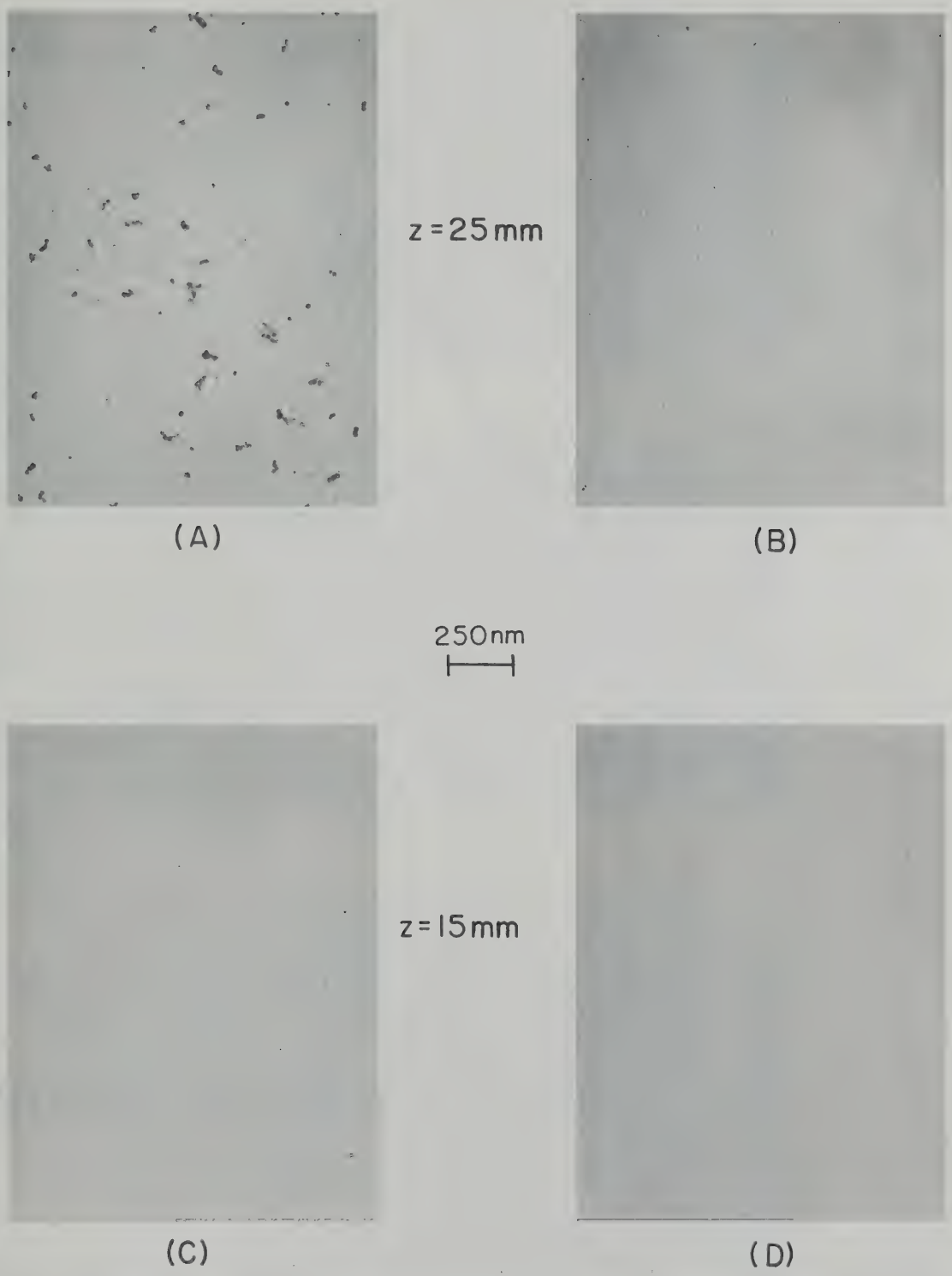

Figure 3.12 TEM micrographs of soot particles collected from the methane coannular diffusion flame using the type II probe. (A) z=25 mm, r=4.03 mm≈r_c, τ_e≈64 ms, (B) z=25 mm, r=4.77 mm>r_c, τ_e≈64 ms, (C) z=15 mm, r=4.43 mm≈r_c, τ_e≈72 ms, (D) z=15 mm, r=5.44 mm>r_c, τ_e≈72 ms.

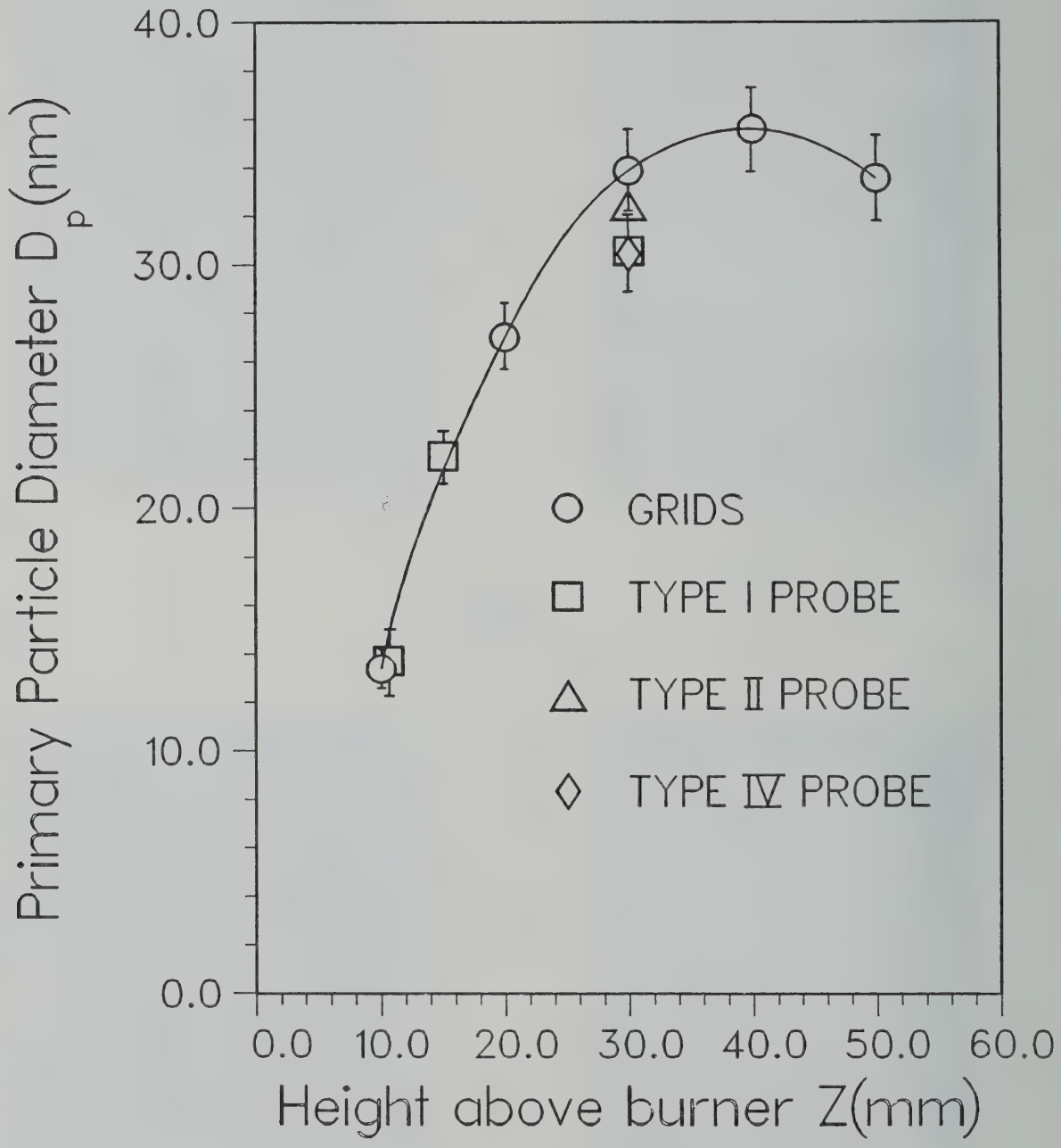

Figure 3.13 Primary particle size as function of height, near $r \approx r_c$, for the ethene diffusion flame. Each size measurement is an average over about 100 primary particles.

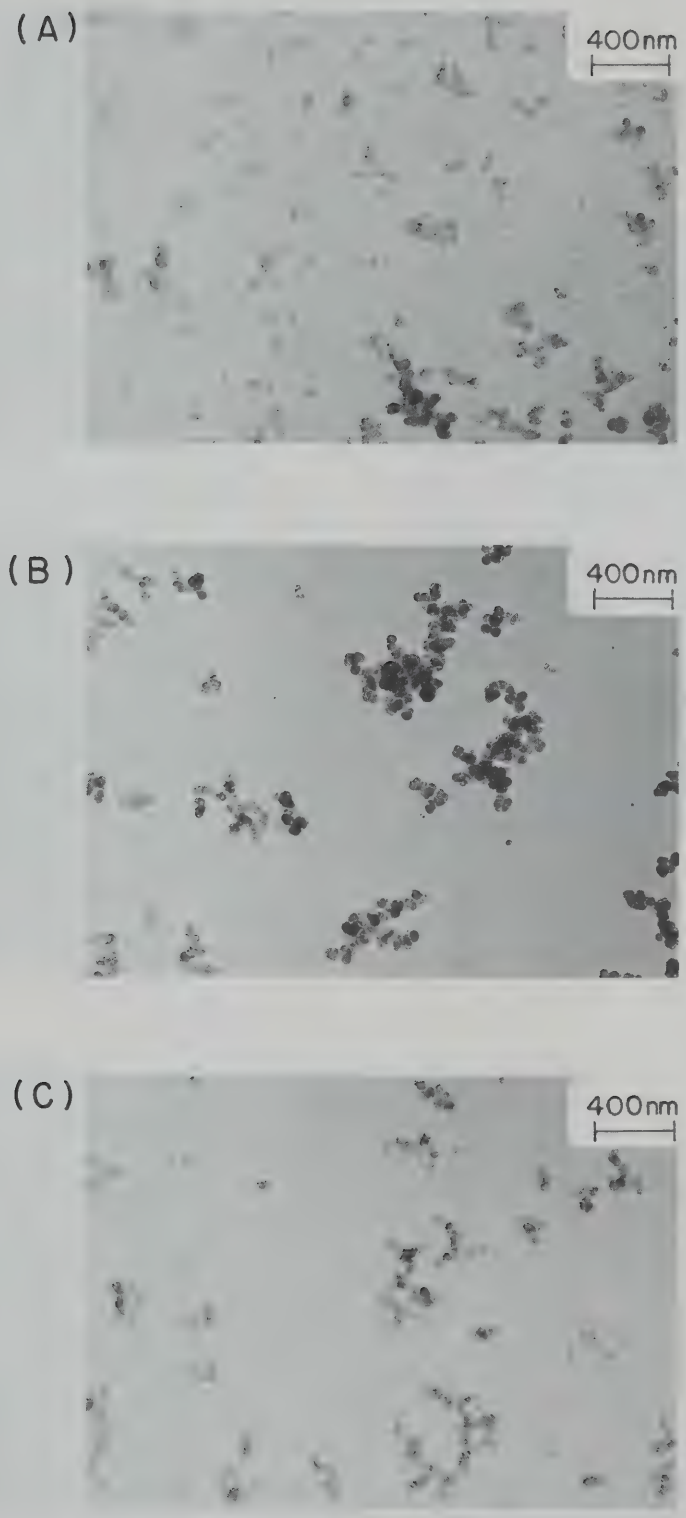

Figure 3.14 TEM micrographs of soot particles collected on a type I probe from an axial location z=30 mm of the ethene diffusion flame, and at three different radial positions (A) r=1.28 mm, (B) r=2.54 mm$\rightarrow r_c$, (C) r=2.89 mm. Probe exposure time τ_e=36 ms.

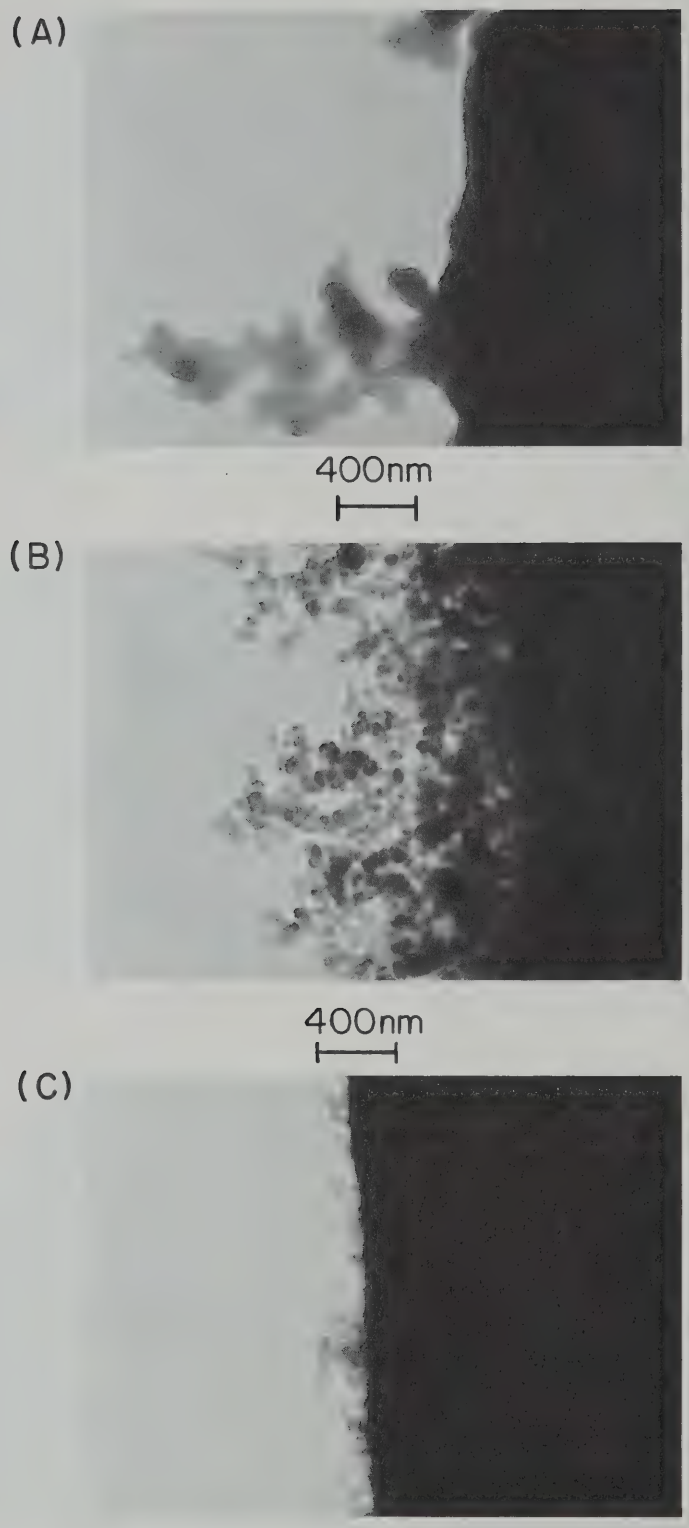

Figure 3.15 TEM micrographs of soot particles collected on a type III probe positioned at z=10 mm in the ethene diffusion flame.Probe exposure time $\tau_e \approx 48$ ms. (A) r=1.54 mm, (B) r=3.96 mm $\rightsquigarrow r_c$,(C) r=4.59 mm.

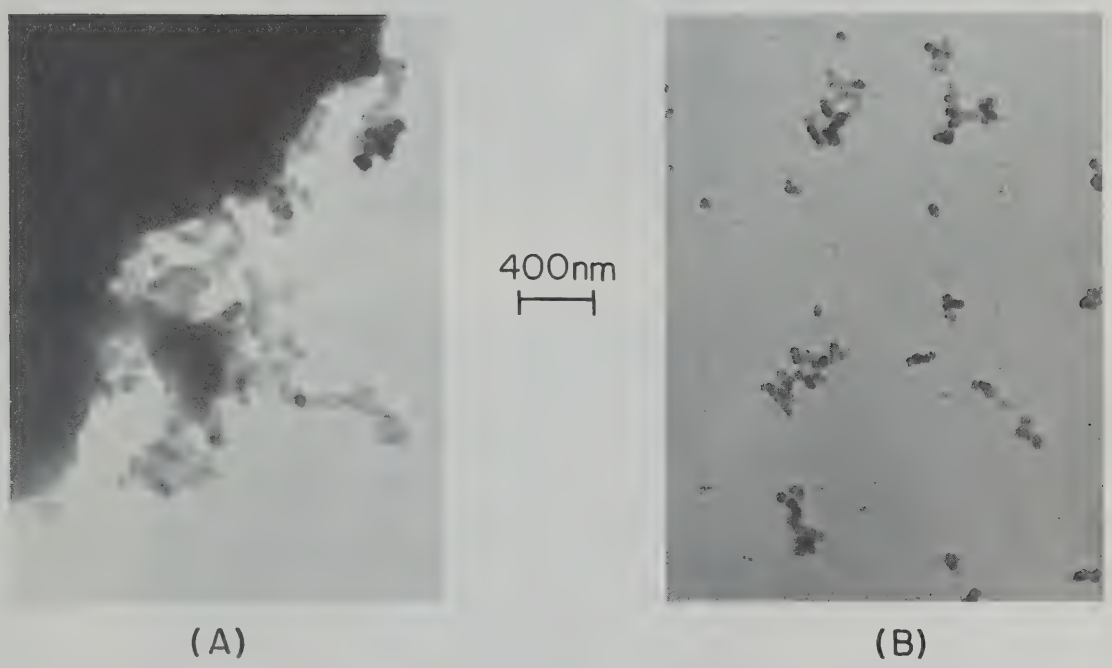

Figure 3.16 TEM micrographs of soot particles collected from the fuel side of $r_c(r<r_c)$, at z=30 mm of the ethene diffusion flame. Type IV probe exposure time $\tau_e \approx 30$ ms. (A) r=0.64 mm, (B) r=1.30 mm.

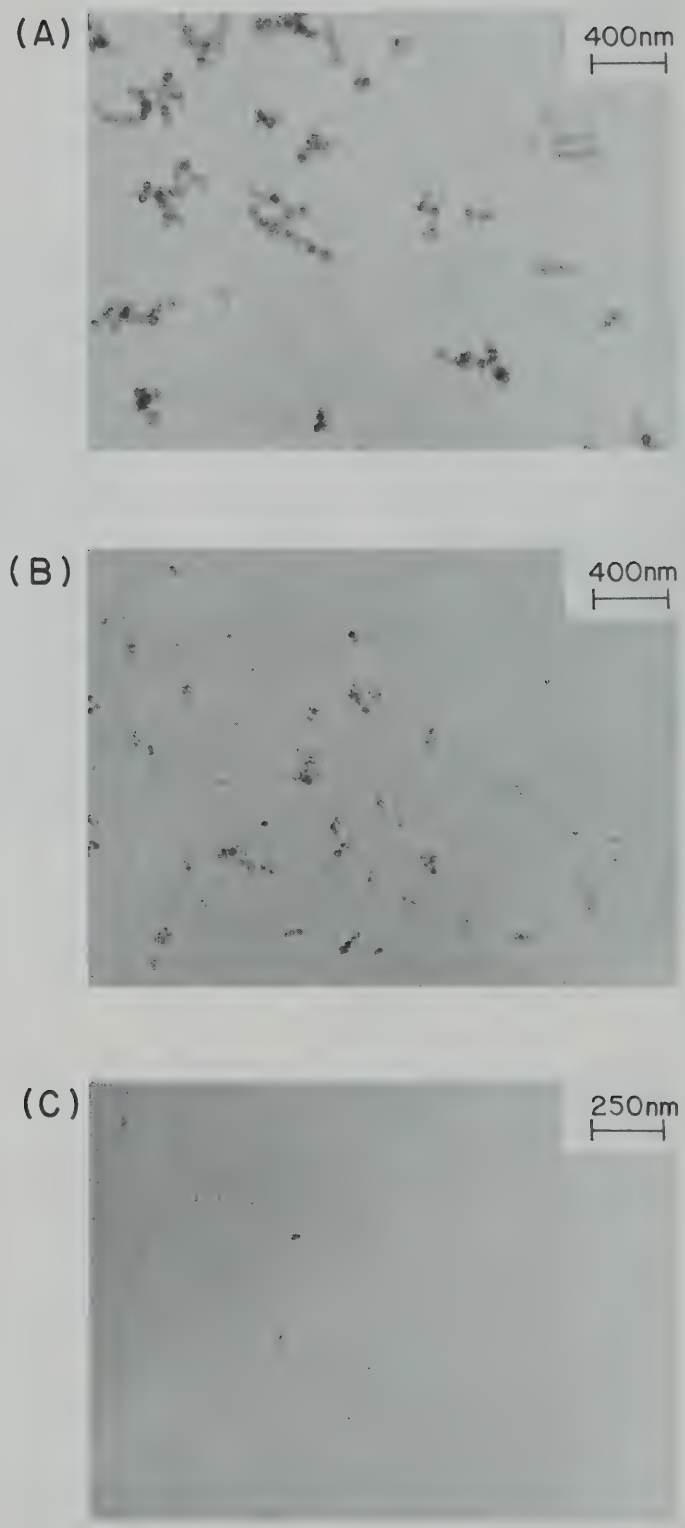

Figure 3.17 TEM micrographs of soot particles collected from the outside region of $r_c(r>r_c)$, at z=30 mm of the ethene diffusion flame. Type IV probe exposure time $\tau_e \approx 36$ ms. (A) r=2.59 mm$\rightarrow r_c$, (B) r=3.13 mm, (C) r=3.35 mm.

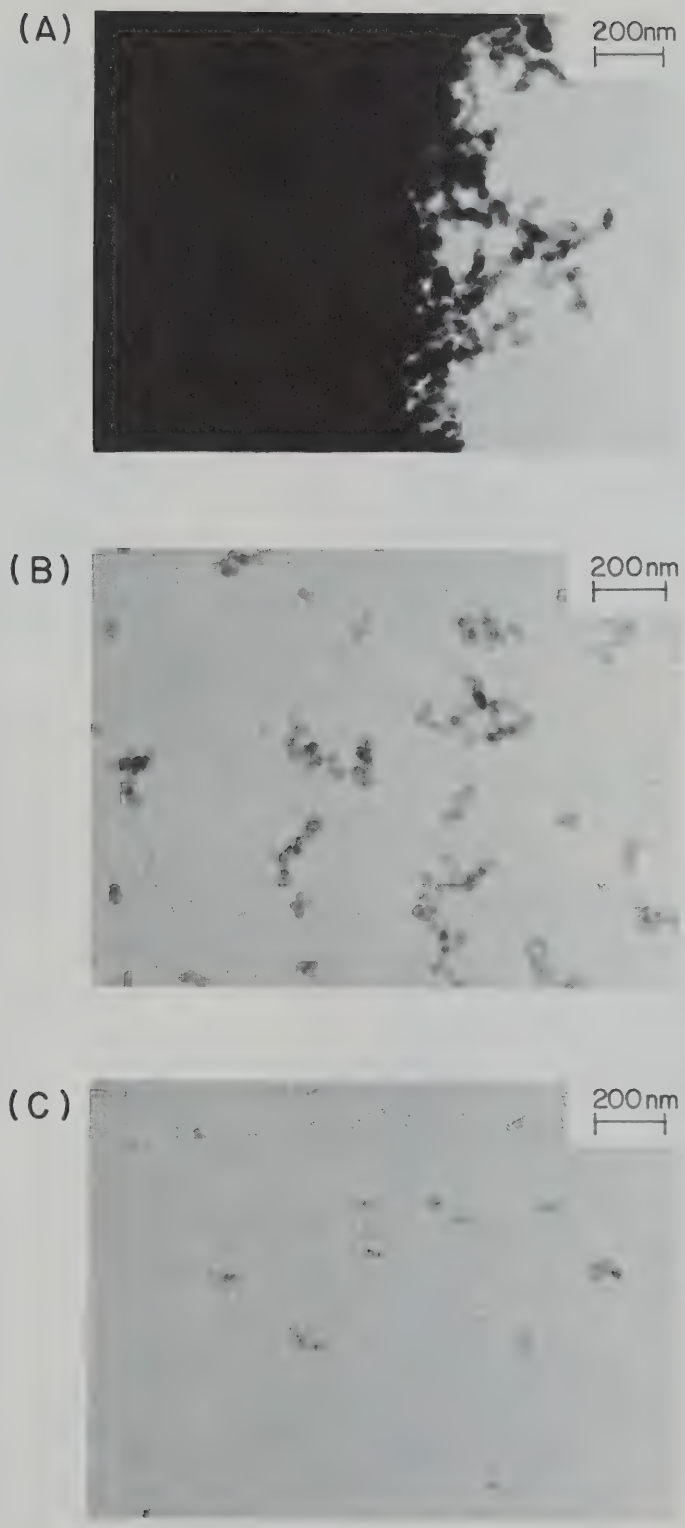

Figure 3.18 TEM micrographs of soot particles collected on a type IV probe positioned at z=15 mm in the ethene diffusion flame. Probe exposure time τ_e≈36 ms. (A) r=0.64 mm, (B) r=2.60 mm, (C) r=3.44 mm.

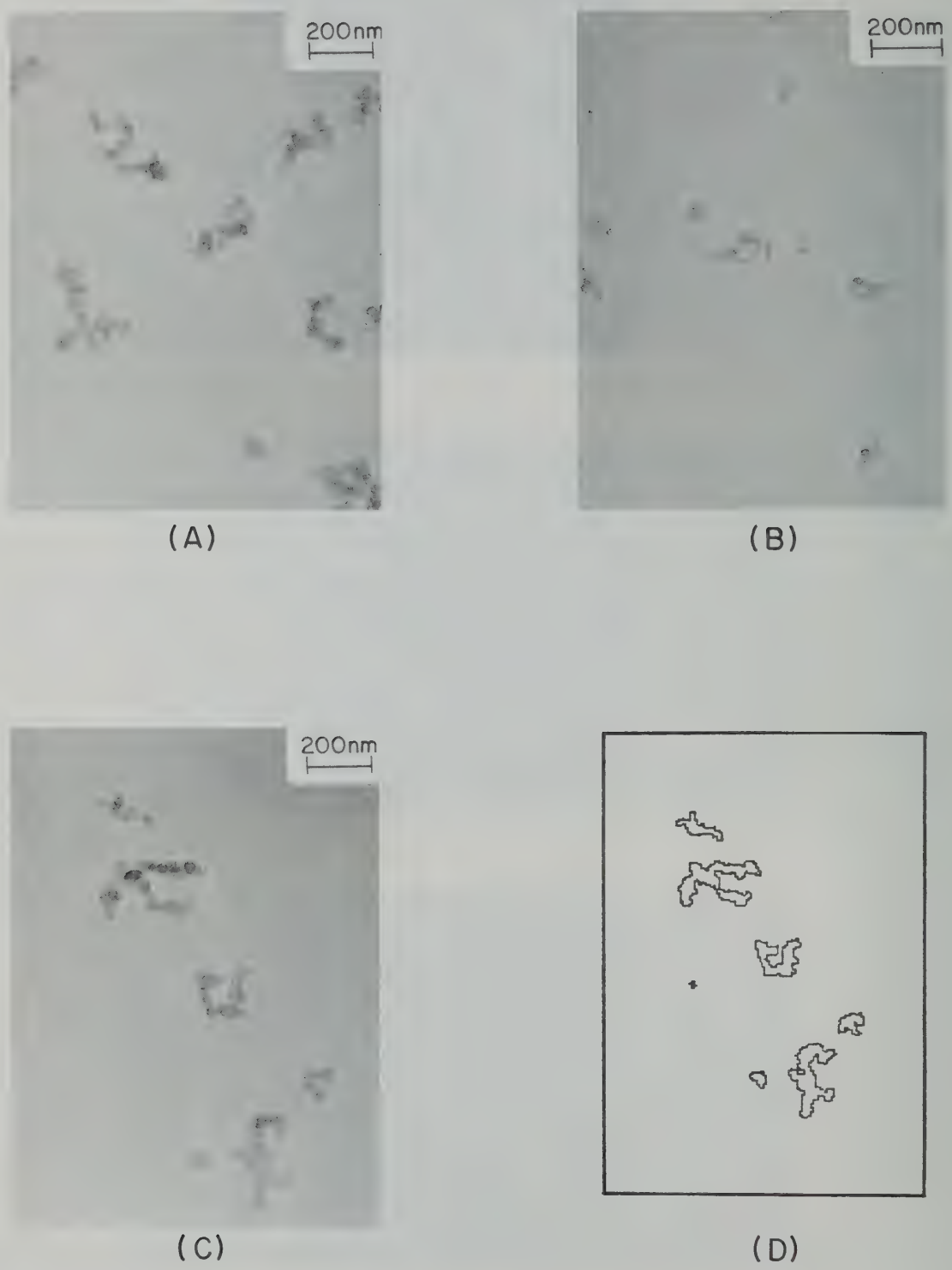

Figure 3.19 TEM micrographs of soot particles collected on a type I probe, positioned at z=15 mm in the ethene diffusion flame. Probe exposure time $\tau_e \approx 36$ ms. (A) r=3.05 mm$\rightarrow r_c$, (B) r=3.73 mm, (C) r=3.05 mm$\rightarrow r_c$, (D) digitized picture of the particles shown in C.

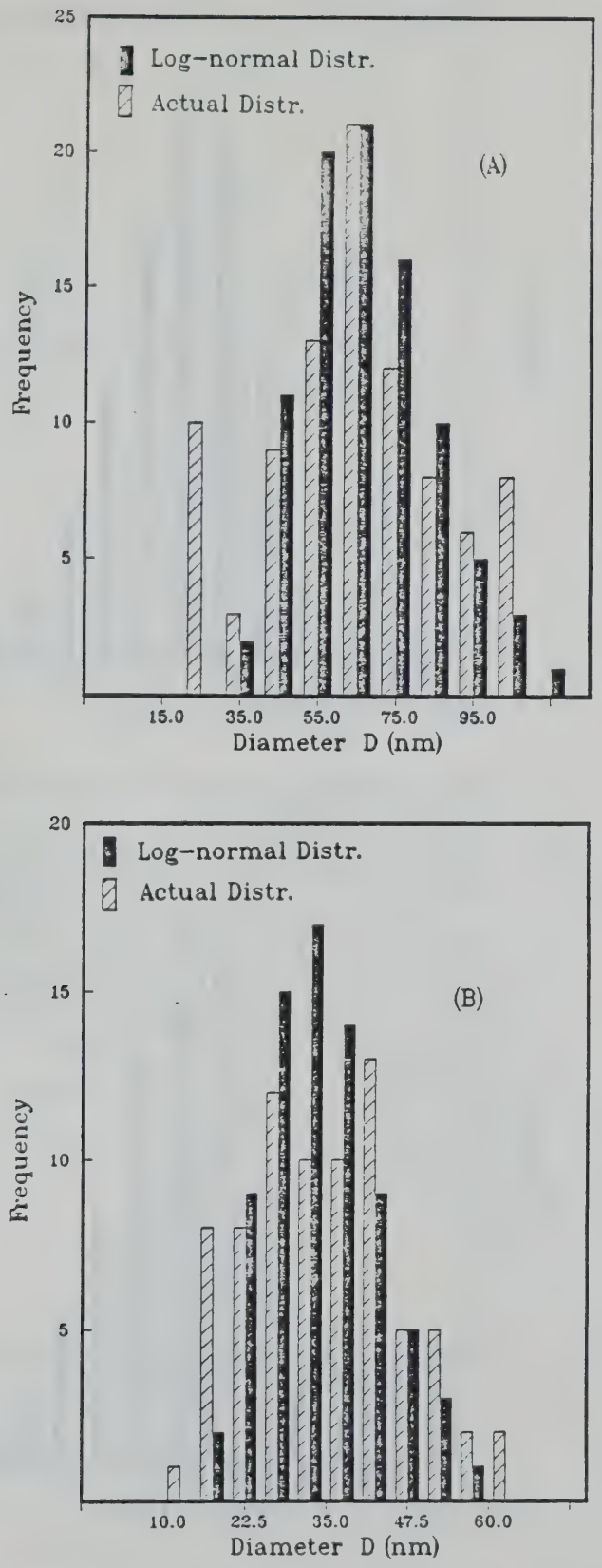

Figure 3.20 Comparison of the actual with the equivalent log-normal distributions at the two radial positions analyzed at z=15 mm. (A) r=3.05 mm, (B) r=3.73 mm.

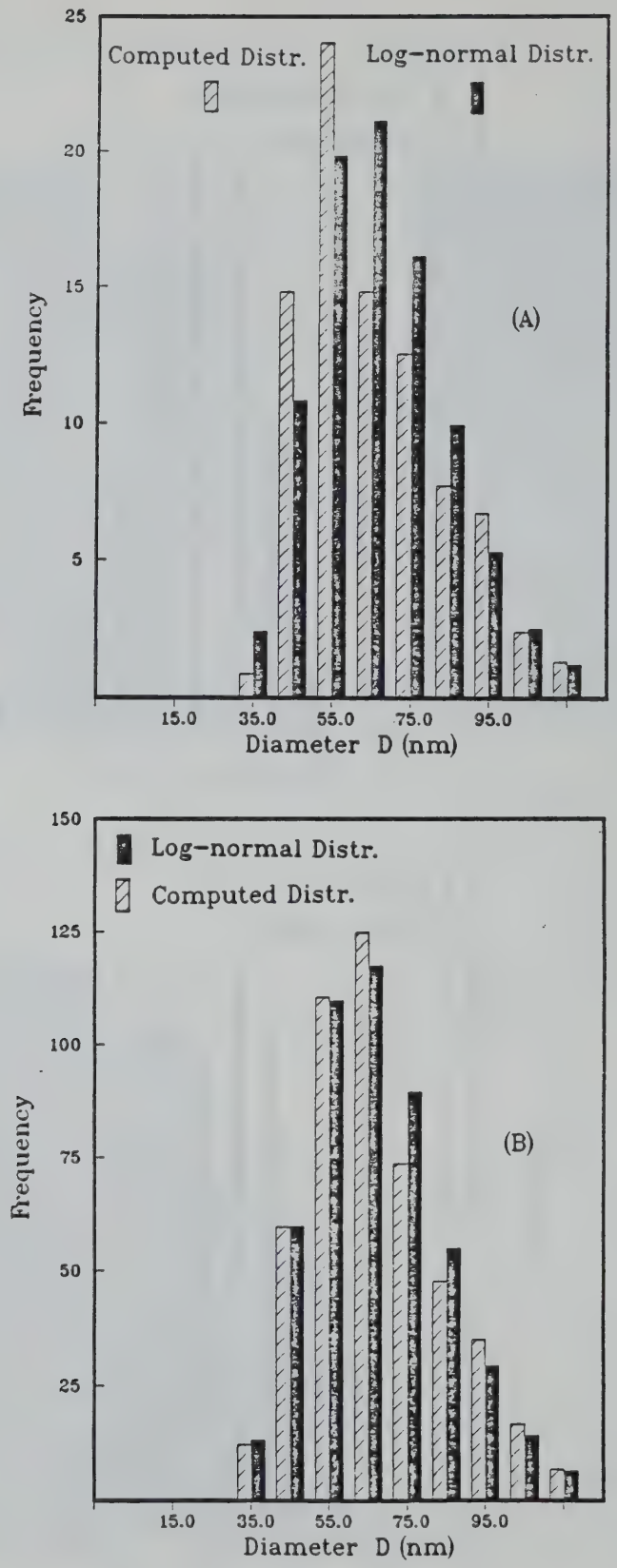

Figure 3.21 Comparison of the distributions obtained from the numerical experiment described in the text. (A) 90 randomly distributed diameters, (B) 500 randomly distributed diameters.

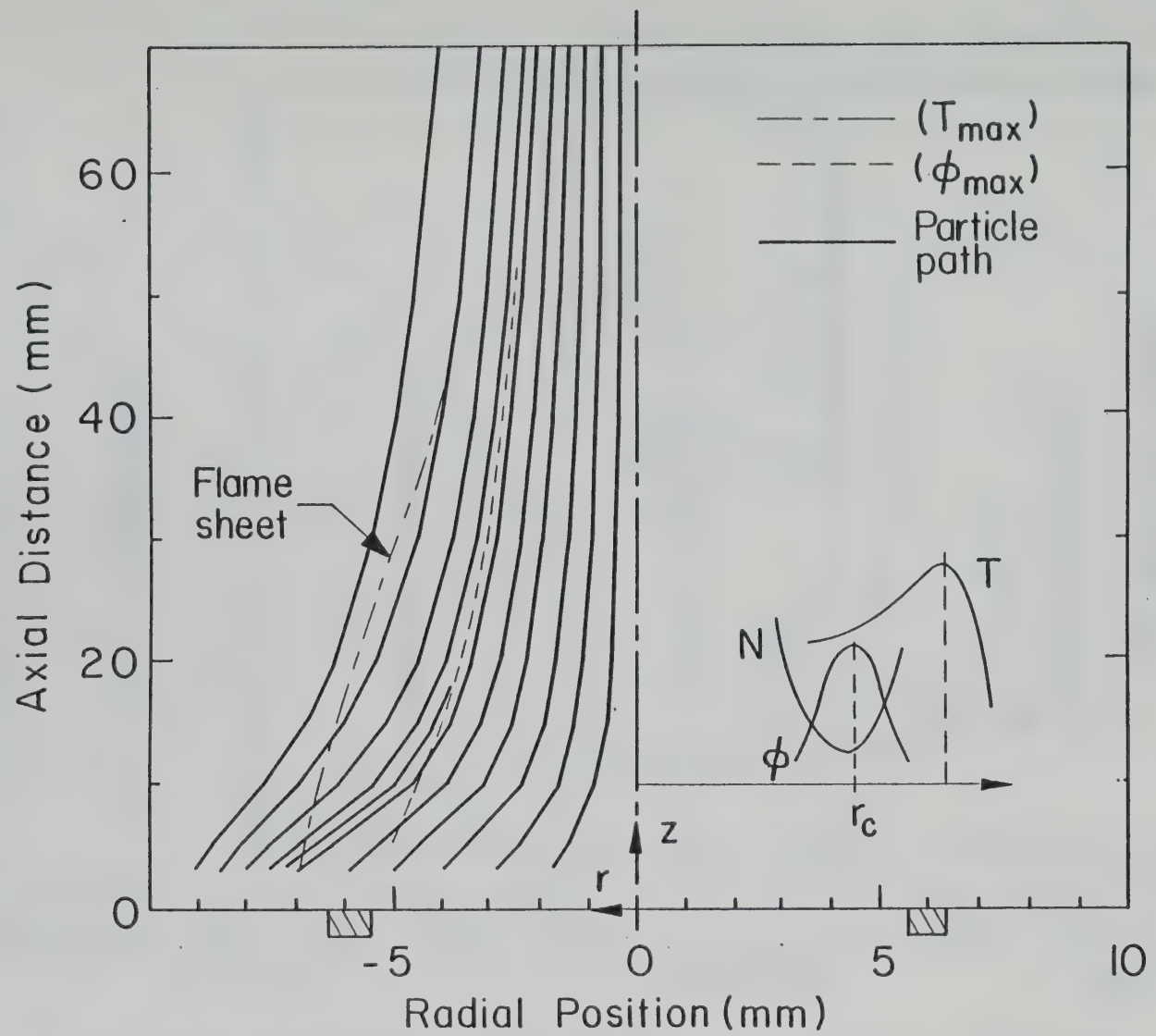

Figure 3.22 Structure of the lower and intermediate regions of the coannular ethene diffusion flame. Particle paths (trajectories) and the loci of T_{max} and ϕ_{max} are also shown. N, ϕ and T profiles corresponding to a height z=10 mm are displayed. Information obtained from refs. 85 and 86.

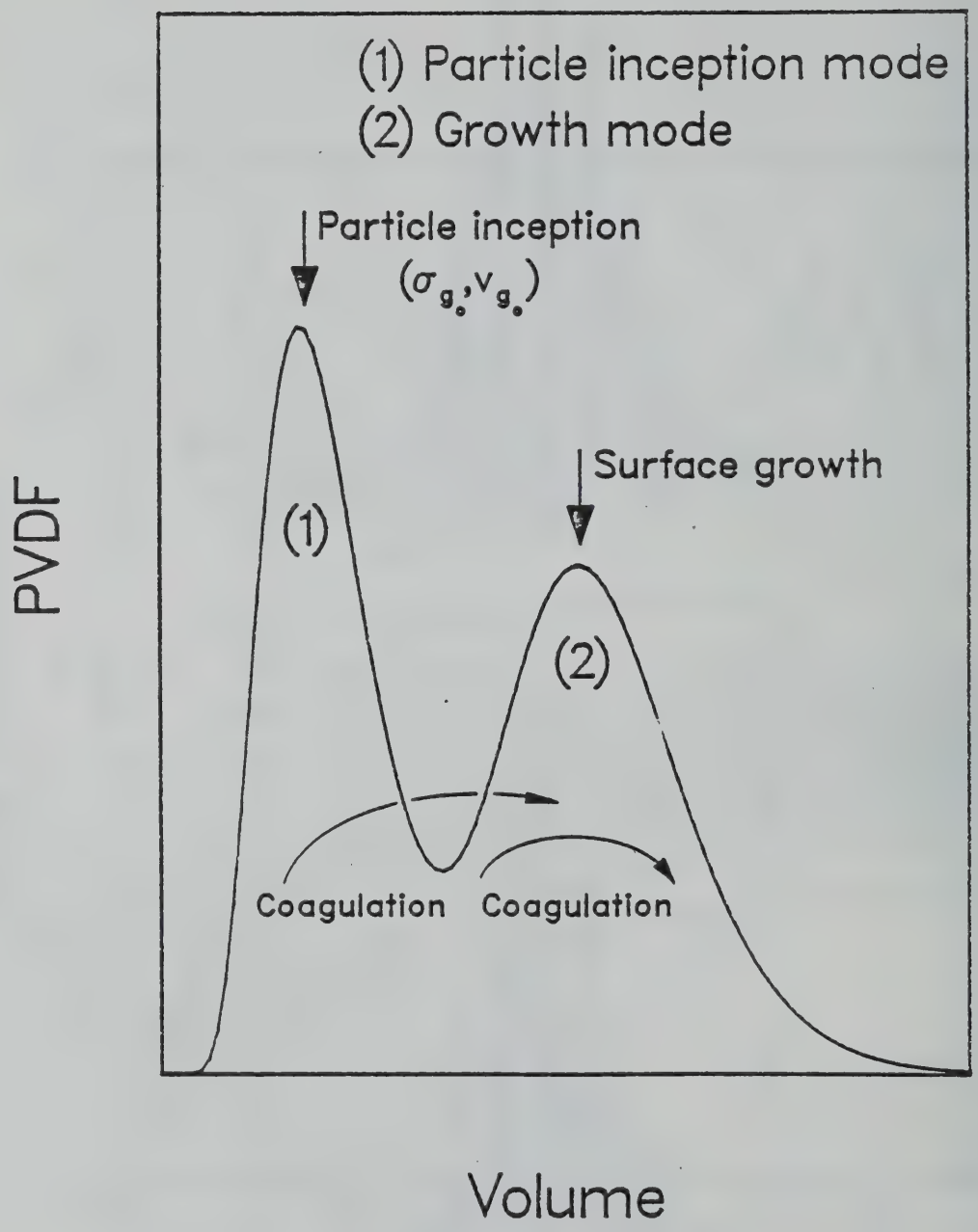

Figure 4.1 Schematic of a bimodal PVDF. The various processes involved in the formulation of the bimodal integral solution are shown.

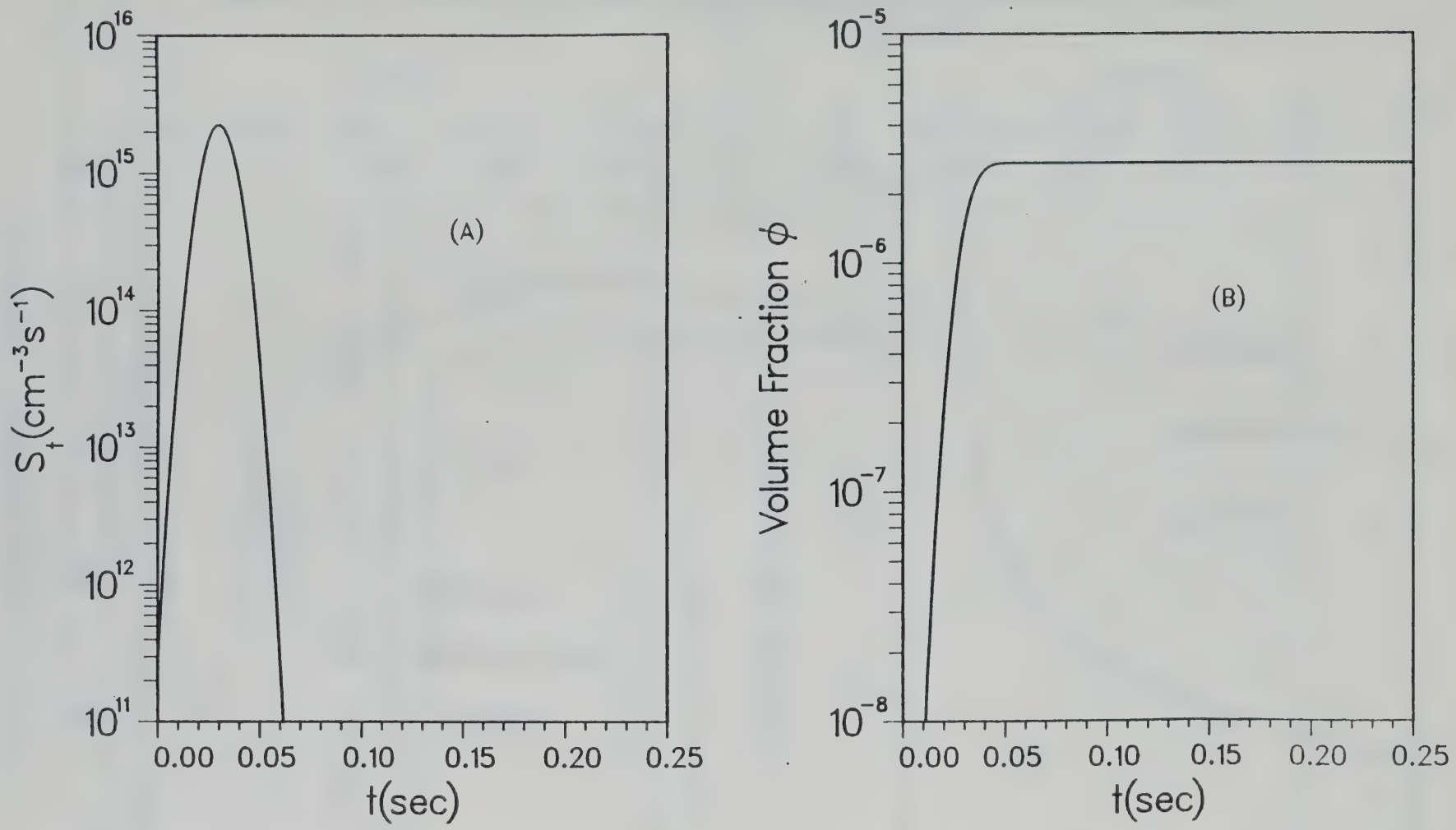

Figure 4.2 (A) Gaussian source pulse used in the example of free molecular coagulation discussed in the text. (B) Particle volume fraction versus time for the same example.

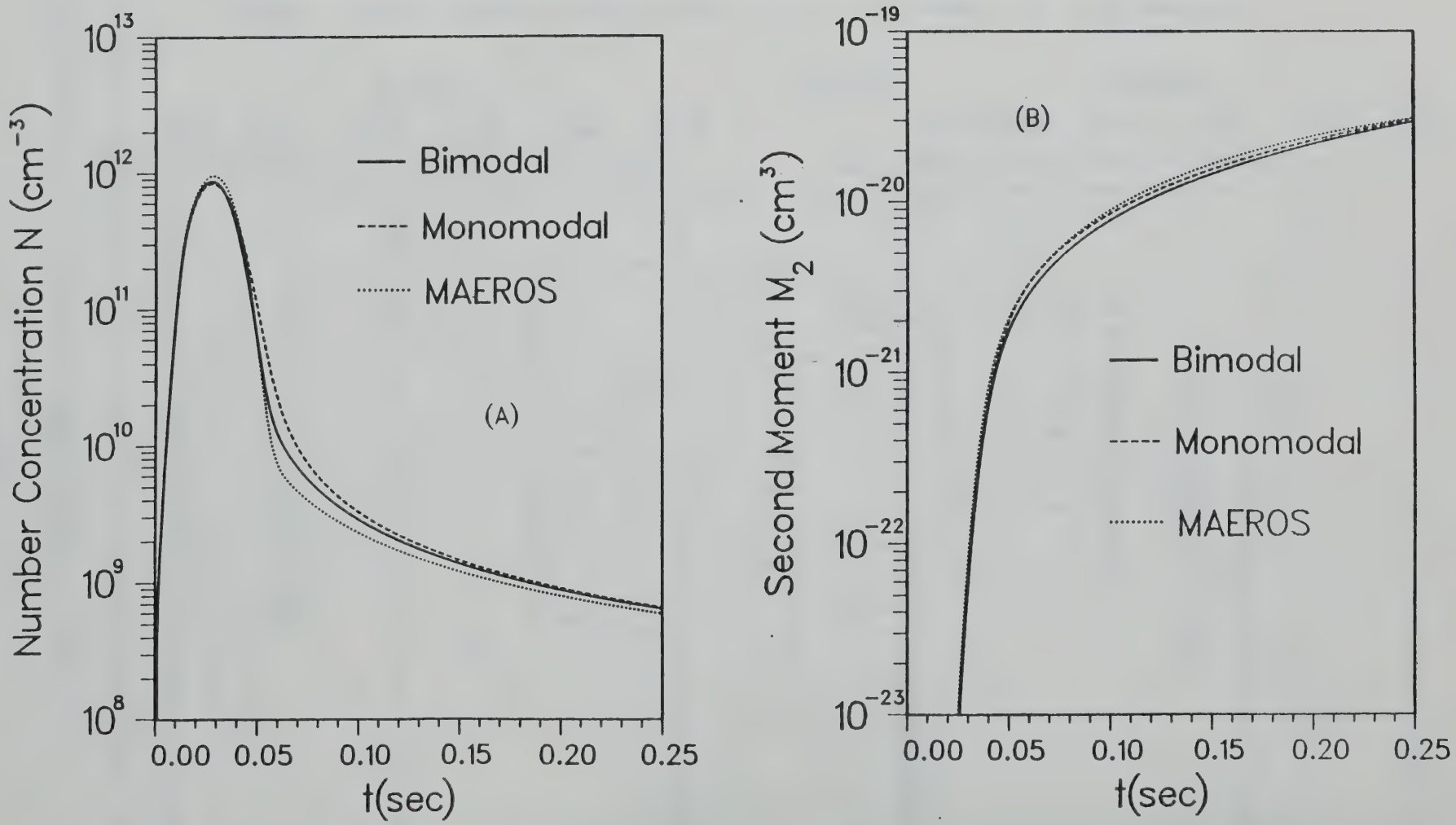

Figure 4.3 (A) Number concentration, and (B) second moment time variation obtained by the three methods examined, for the case of free molecular coagulation with a Gaussian source term.

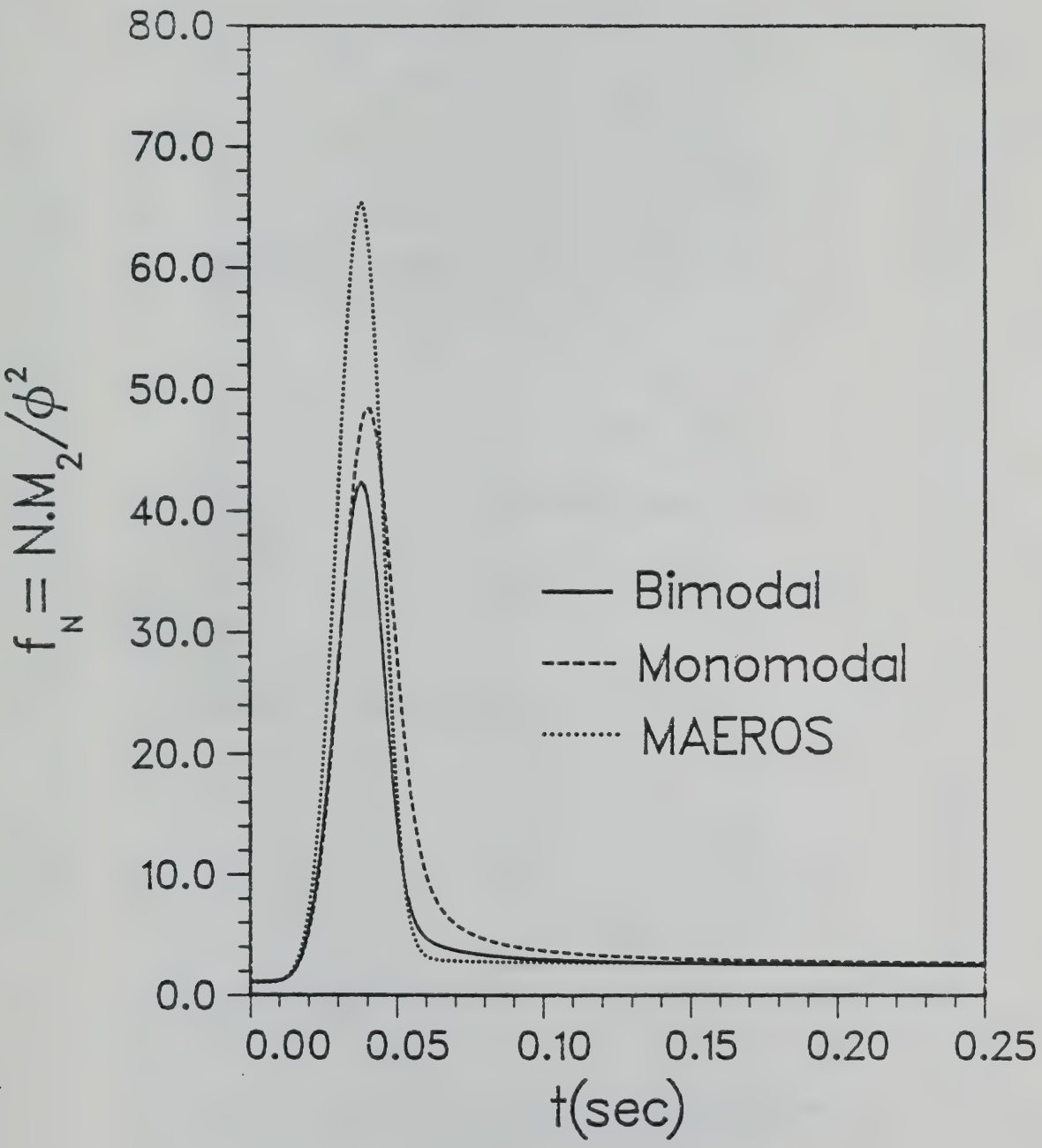

Figure 4.4 Comparison of f_N profiles obtained by the three methods, for the case of free molecular coagulation with a Gaussian source term.

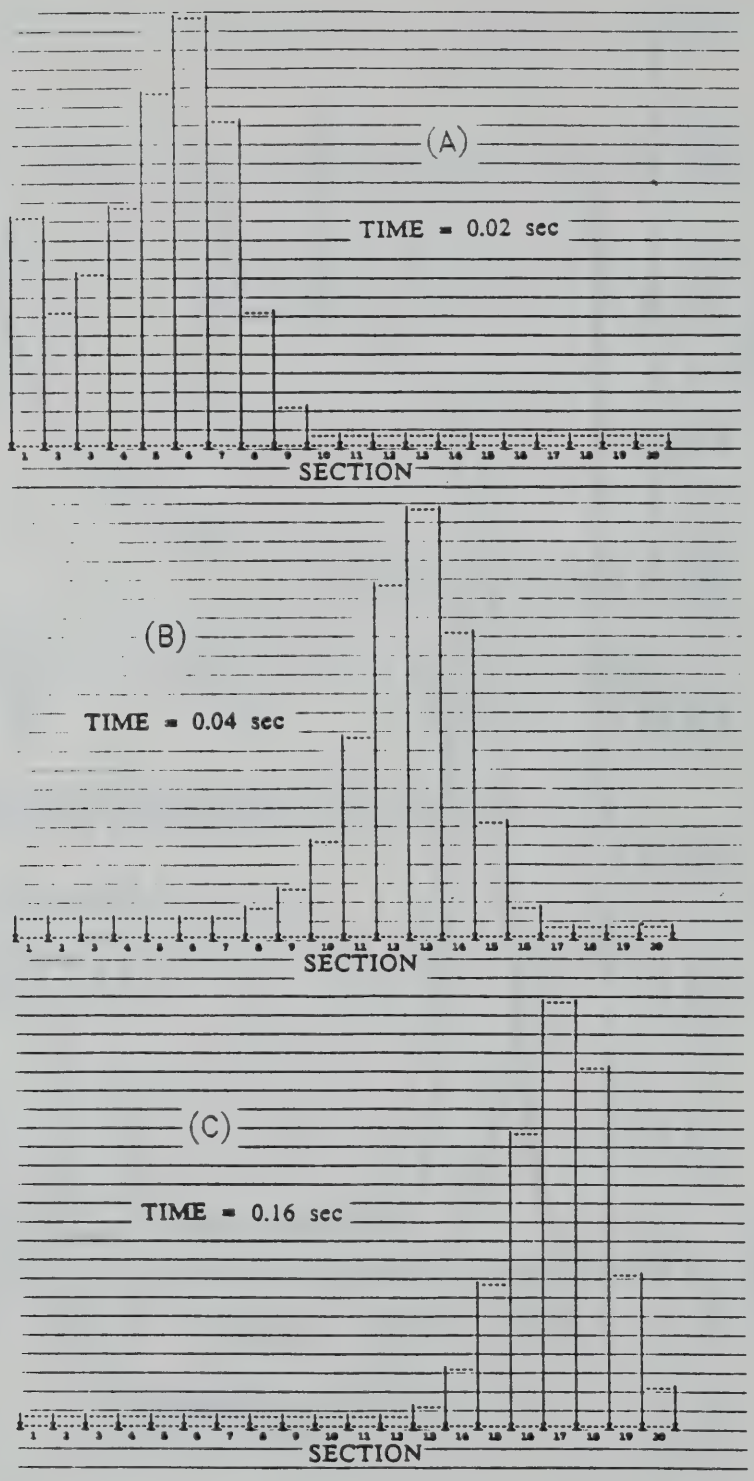

Figure 4.5 Mass concentration histograms obtained by the MAEROS solution for the case of free molecular coagulation with a Gaussian source term. (A) t=0.02 sec, (B) t=0.04 sec, (C) t=0.16 sec.

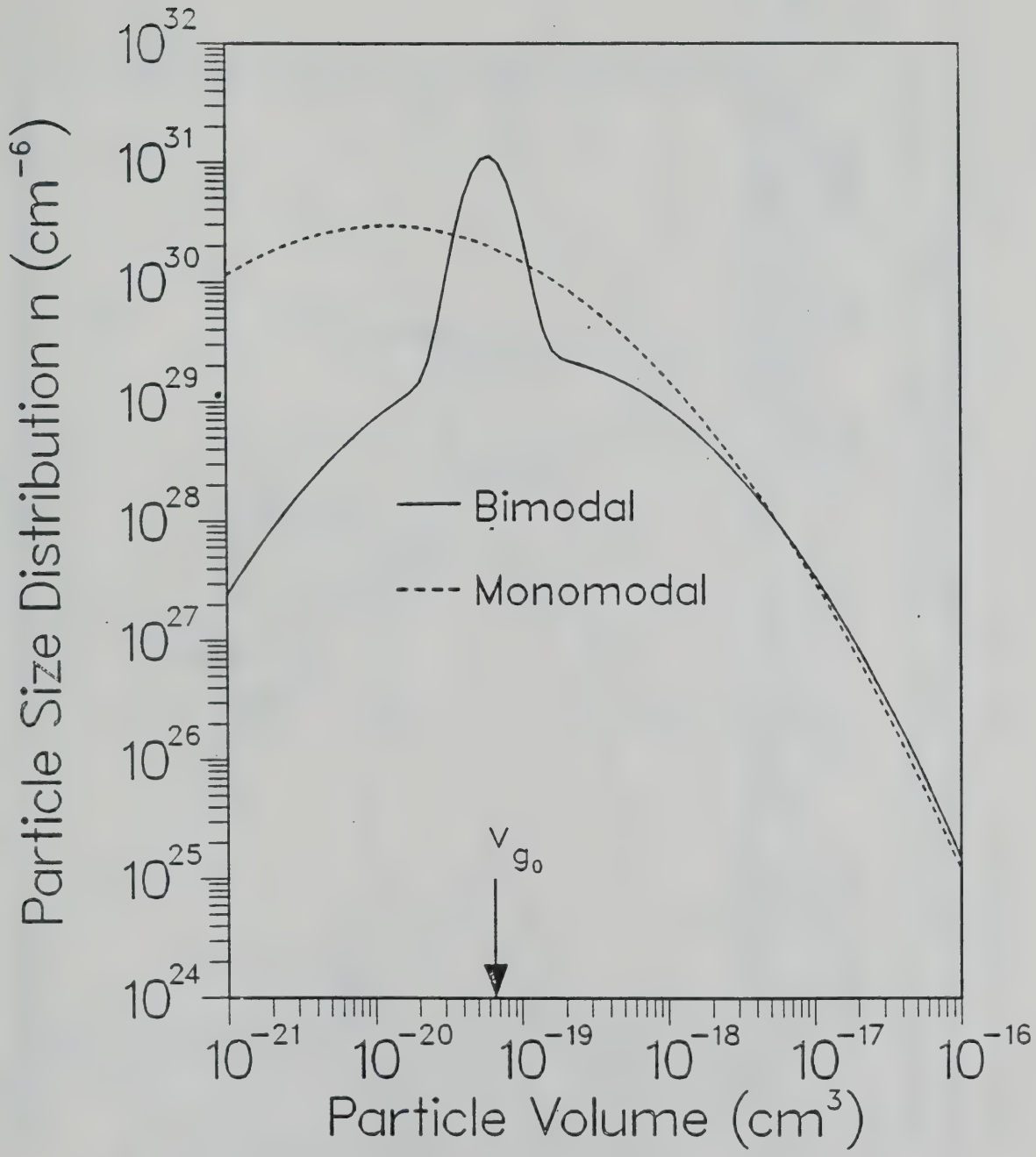

Figure 4.6 Particle volume distribution obtained by the two integral solutions, at an instant where the source term achieves a maximum (t_m=0.03 sec). The geometric mean volume of the source particles is also shown.

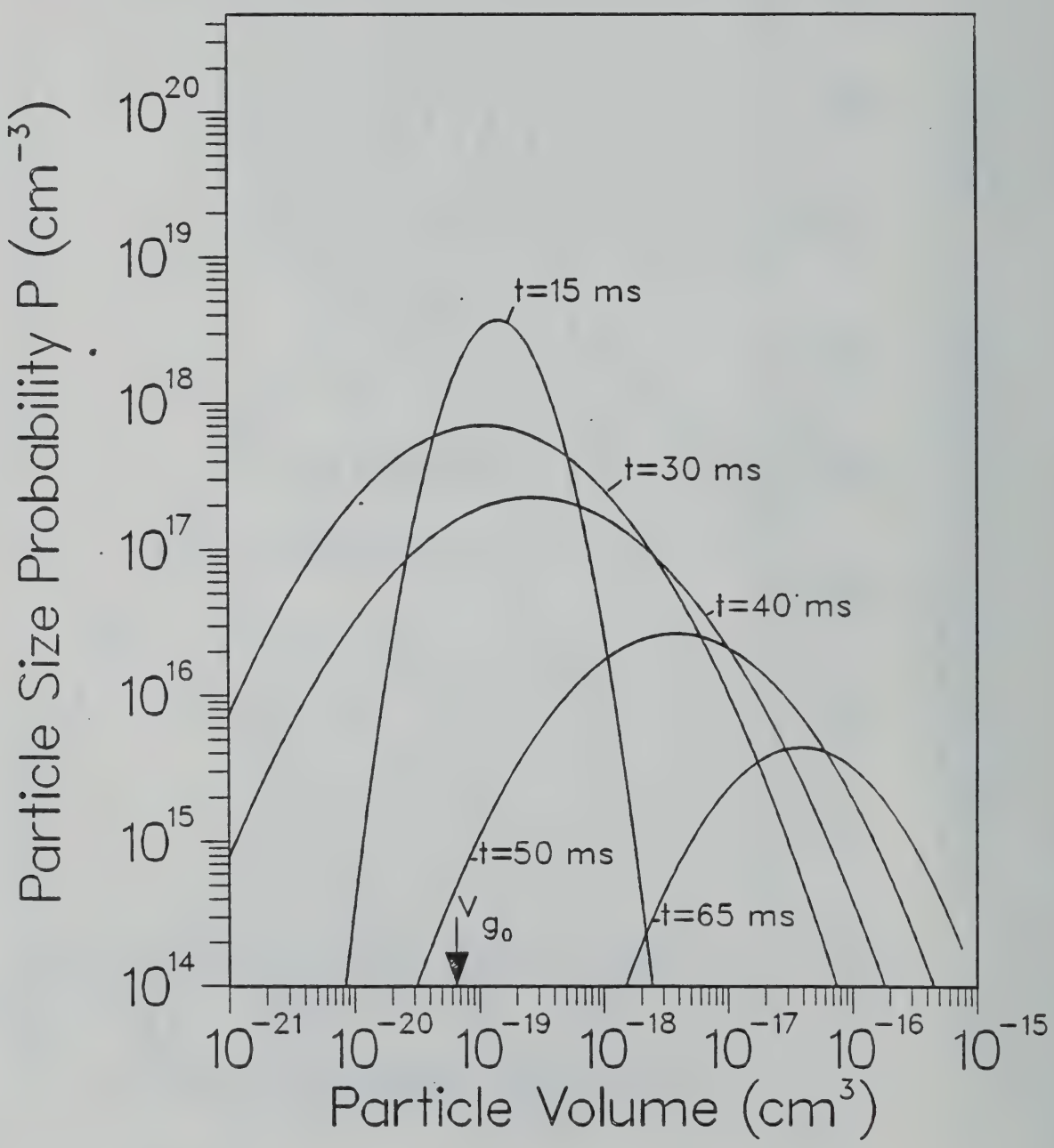

Figure 4.7 Time evolution of the PVPF of the growth mode for the case of free molecular coagulation with a Gaussian source term.

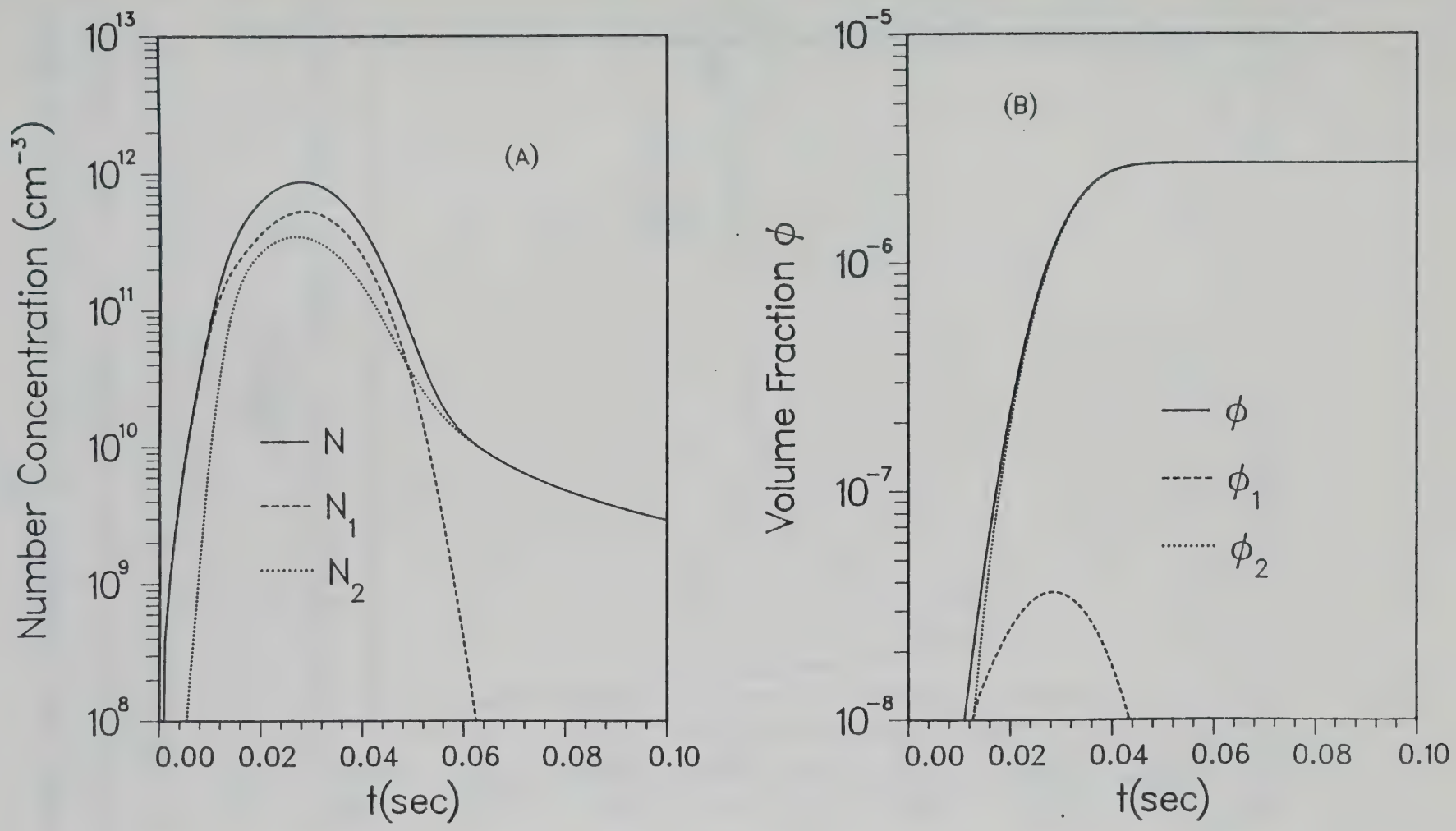

Figure 4.8 (A) Number concentration, and (B) particle volume fraction time variation of the two modes, as calculated by the bimodal integral solution for the case of free molecular coagulation with a Gaussian source term.

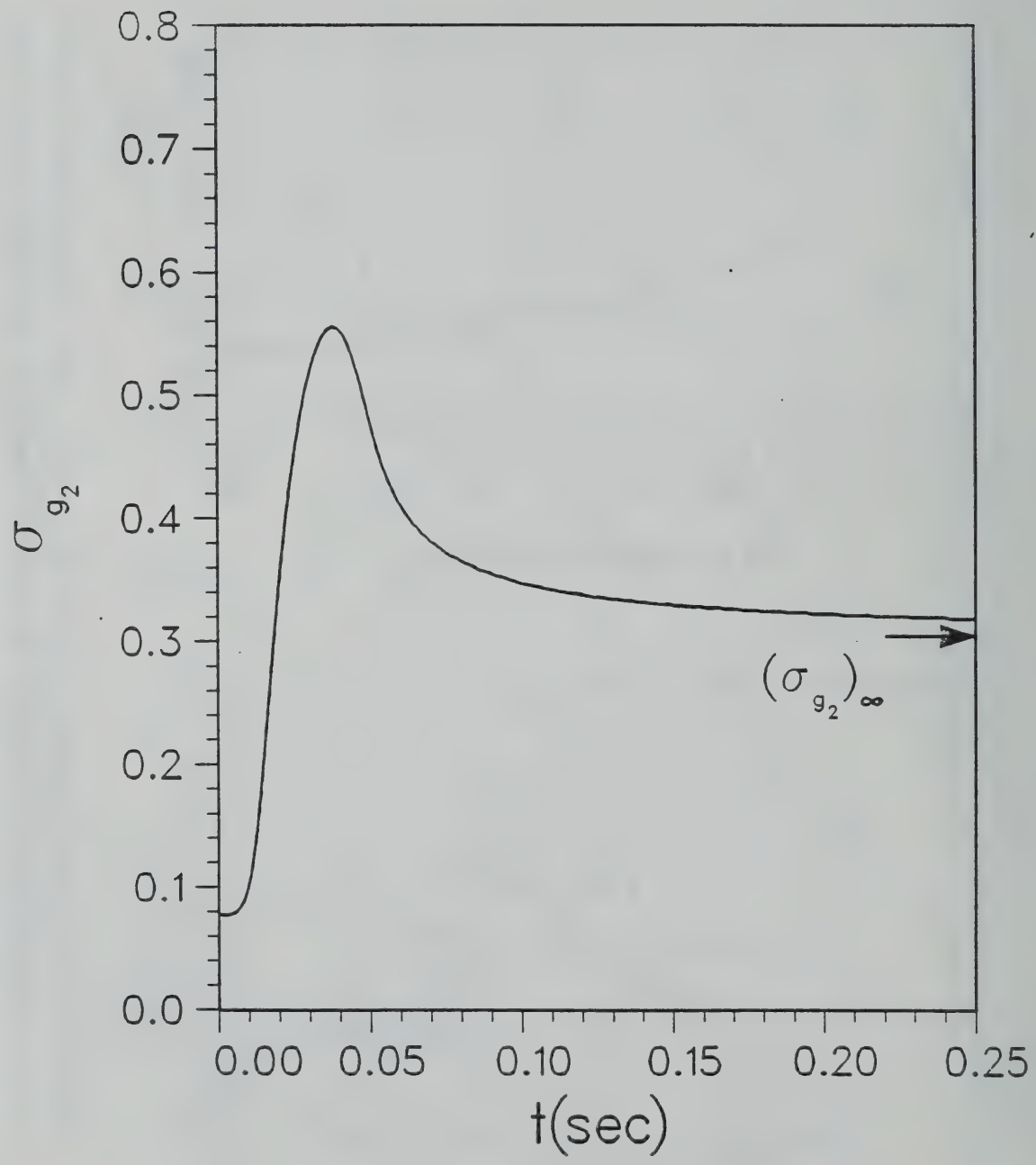

Figure 4.9 Time variation of the geometric standard deviation of the growth mode for the case of free molecular coagulation with a Gaussian source term. The asymptotic value corresponding to the self-preserving form is also shown.

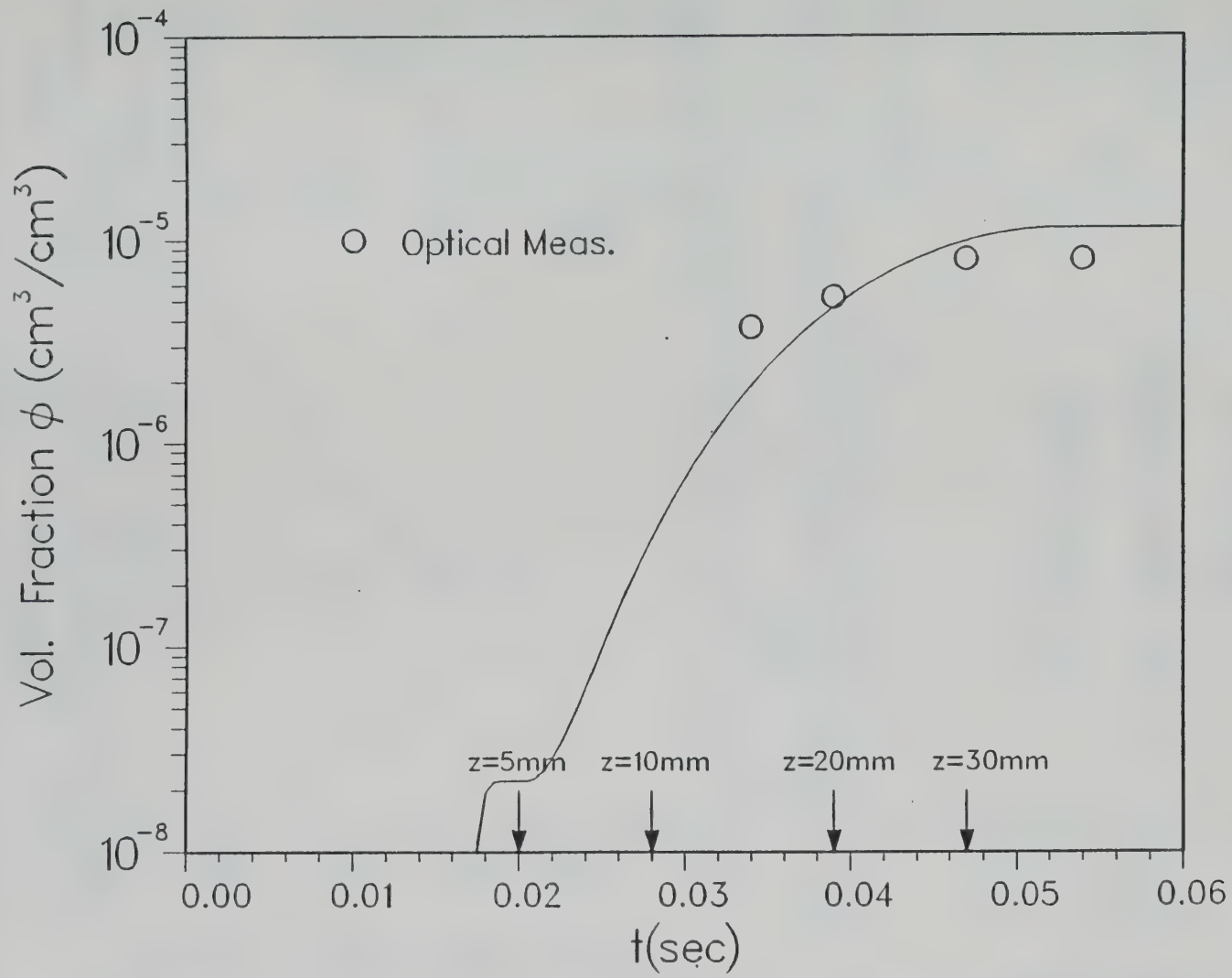

Figure 4.10 Particle volume fraction profile used by the bimodal solution to duplicate the optically determined values. These values correspond to particles transported on the annular region and were determined using Mie scattering theory.

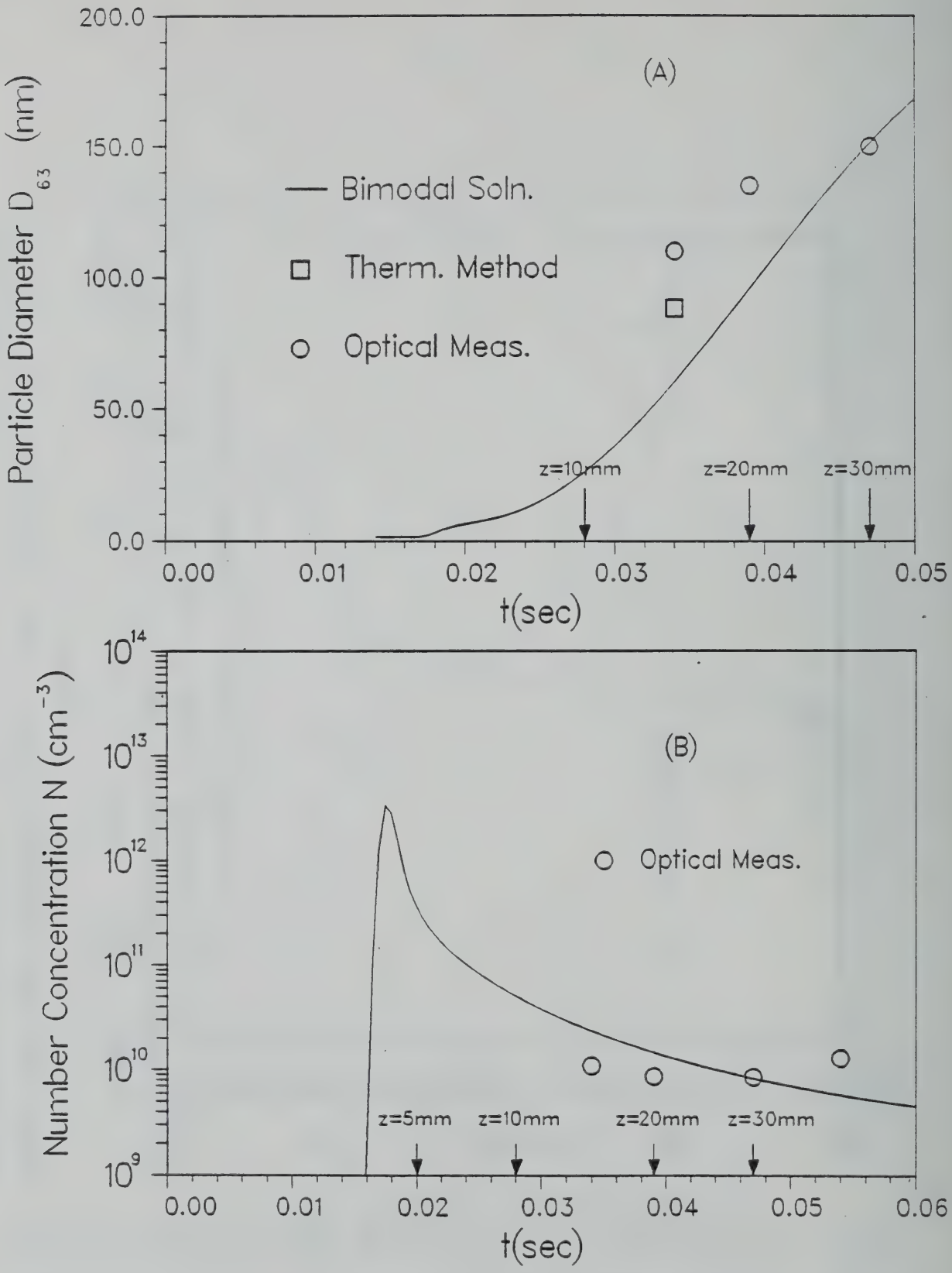

Figure 4.11 (A) Particle diameter and (B) number concentration versus residence time, as calculated by the bimodal solution in the numerical simulation of the soot aerosol. The values determined by the optical and thermophoretic techniques are also shown.

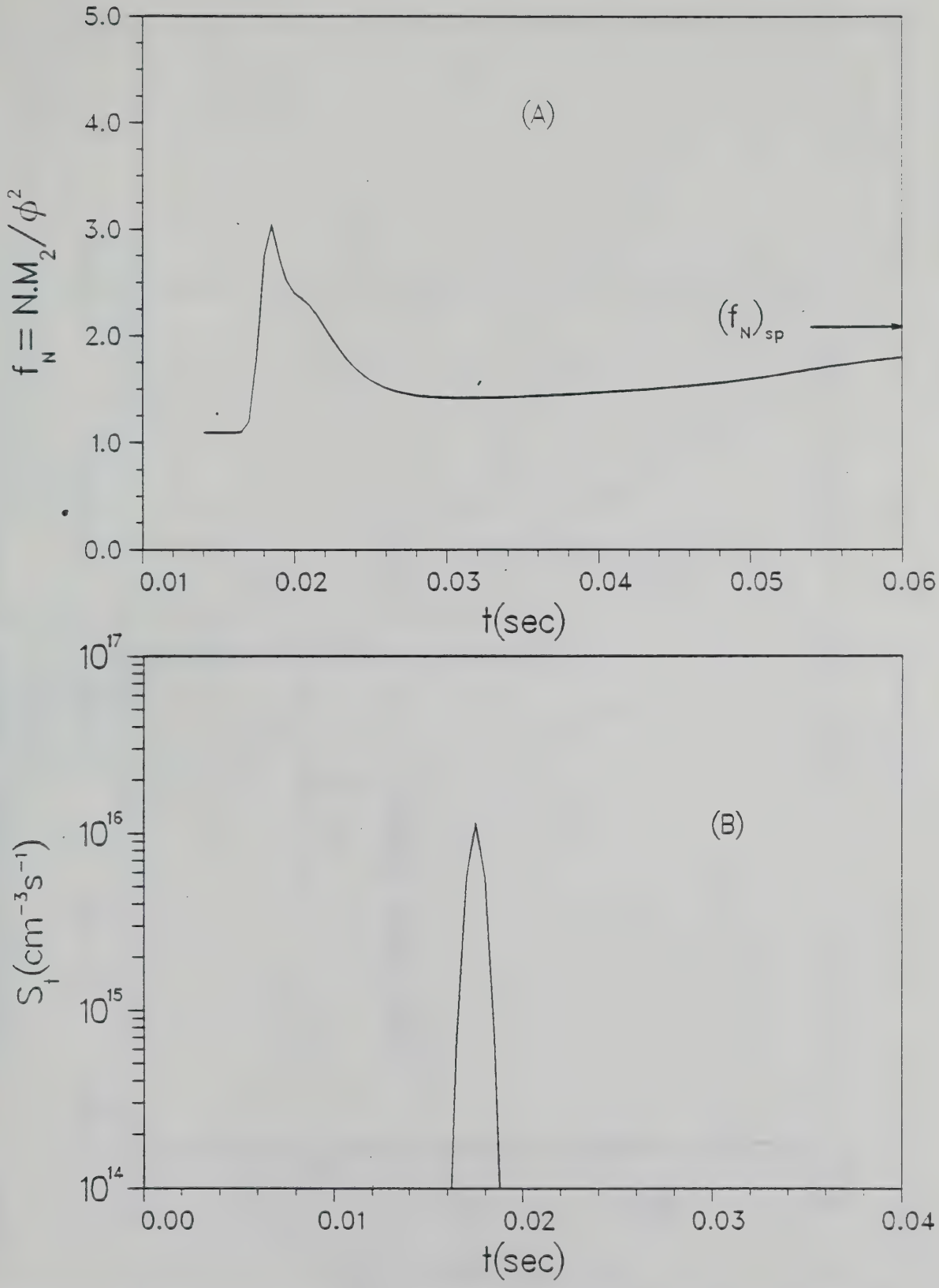

Figure 4.12 (A) Time variation of f_N and (B) Gaussian source pulse used in the numerical simulation of the soot aerosol.

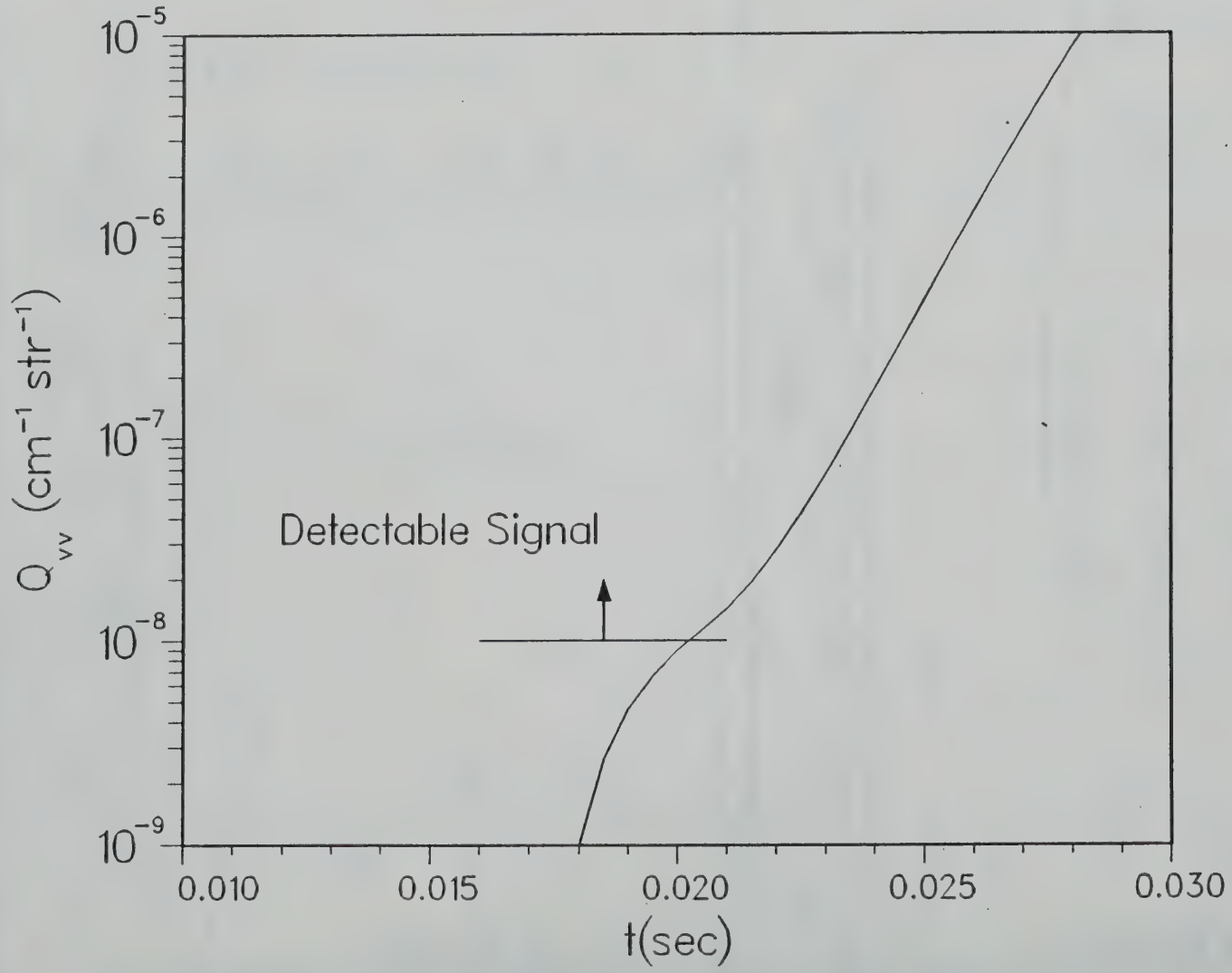

Figure 4.13 Time variation of volumetric Rayleigh scattering cross section Q_{vv} as calculated by the bimodal solution in the numerical simulation of the soot aerosol.

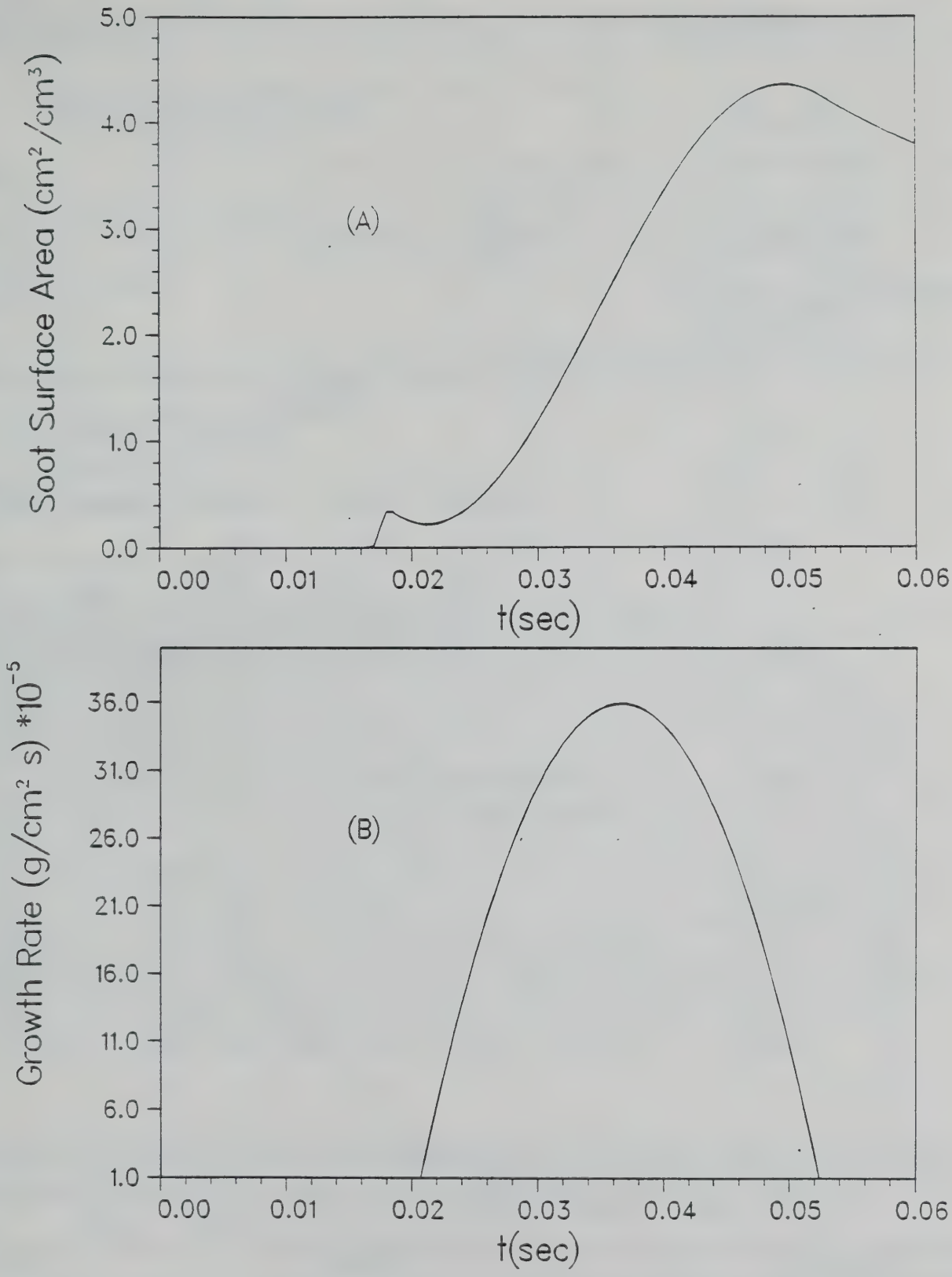

Figure 4.14 Time variation of (A) soot surface area and (B) specific growth rate used in the numerical simulation of the soot aerosol.

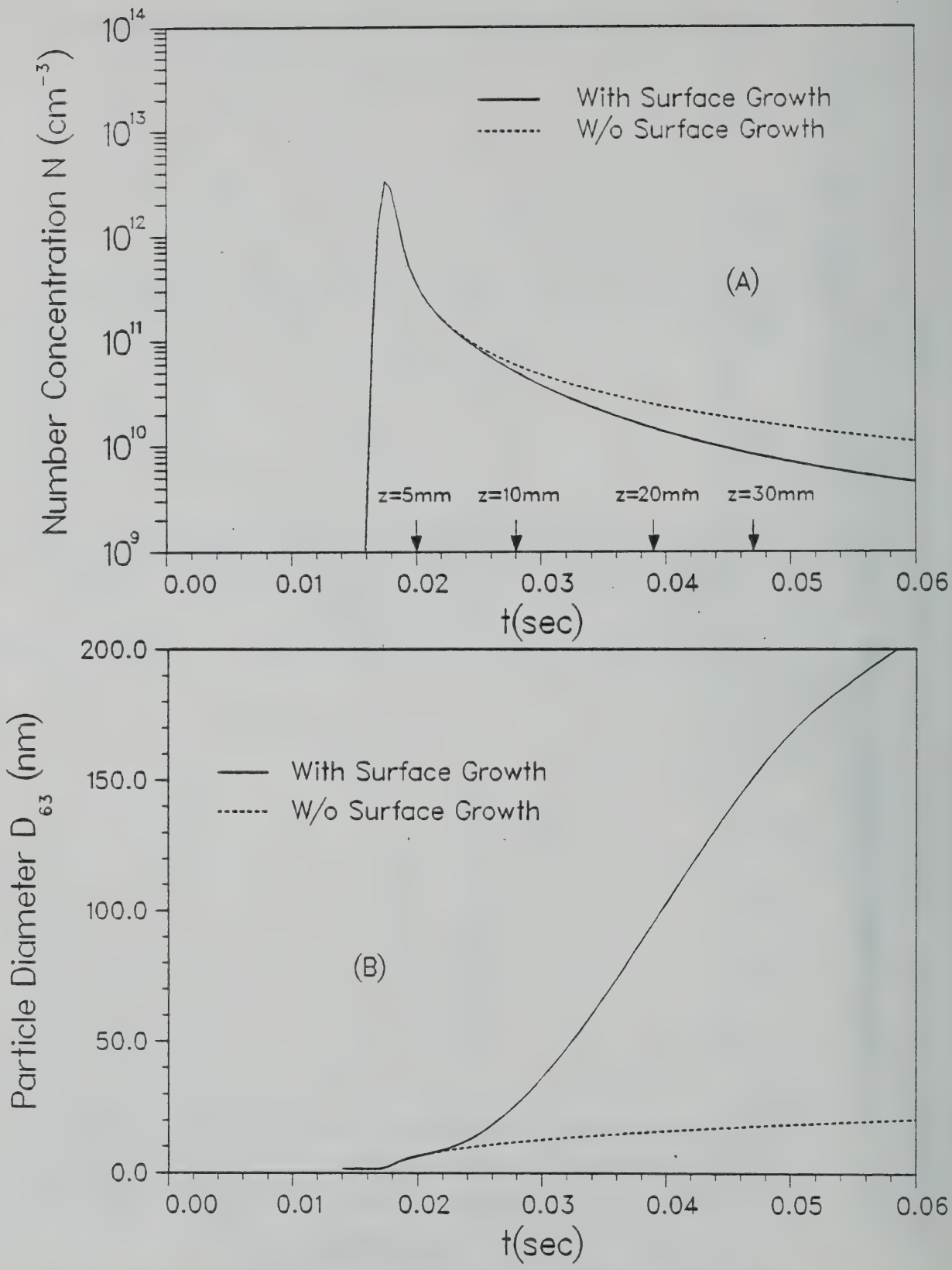

Figure 4.15 Time variation of (A) particle number concentration, and (B) particle diameter with and without the surface growth reaction term.

NBS-114A (REV. 2-80)

U.S. DEPT. OF COMM. BIBLIOGRAPHIC DATA SHEET (See instructions)	1. PUBLICATION OR REPORT NO. NBS/GCR-87/532	2. Performing Organ. Report No.	3. Publication Date December 1987

4. TITLE AND SUBTITLE

Thermophoretic Sampling and Soot Aerosol Dynamics of an Ethene Diffusion Flame

5. AUTHOR(S)

Constantine M. Megaridis

6. PERFORMING ORGANIZATION (If joint or other than NBS, see instructions)

Brown University
Providence, RI

7. Contract/Grant No.

8. Type of Report & Period Covered

May 1986

9. SPONSORING ORGANIZATION NAME AND COMPLETE ADDRESS (Street, City, State, ZIP)

National Bureau of Standards
Department of Commerce
Gaithersburg, MD 20899

10. SUPPLEMENTARY NOTES

☐ Document describes a computer program; SF-185, FIPS Software Summary, is attached.

11. ABSTRACT (A 200-word or less factual summary of most significant information. If document includes a significant bibliography or literature survey, mention it here)

A detailed investigation of the sooting structure of an overventilated laminar axisymmetric ethene/air diffusion flame under atmospheric pressure is presented. A thermophoretic sampling technique using a variety of probes is employed to obtain data on the morphological character of soot particles collected from various locations of the flame. The morphological features of the particles examined by Transmission Electron Microscopy provide not only qualitative information on particle agglomeration, surface growth, and oxidation but also quantitative data on primary particle size as a function of flame coordinates. An increasing primary particle size with height above the burner mouth proved the dominance of surface growth reactions on the morphology of particles transported in the lower and intermediate portions of the flame. The primary particle size was found to decrease as the particles move to the upper regions of the flame probably because of oxidation. A theoretical model examining the aerosol dynamics when particle formation, coagulation, and surface growth are present is also discussed. The combined observations of the thermophoretic method and optical measurements by others led to the conclusion that the soot particles are formed locally low in the flame in regions of high temperature near the reaction zone.

12. KEY WORDS (Six to twelve entries; alphabetical order; capitalize only proper names; and separate key words by semicolons)

aerosols; diffusion flames; morphology; particle size; soot; soot formation

13. AVAILABILITY

☒ Unlimited
☐ For Official Distribution. Do Not Release to NTIS
☐ Order From Superintendent of Documents, U.S. Government Printing Office, Washington, D.C. 20402.
☒ Order From National Technical Information Service (NTIS), Springfield, VA. 22161

14. NO. OF PRINTED PAGES

210

15. Price

$24.95

USCOMM-DC 6043-P80